Thèse n° 10 837

Turbulence and Heat exchange in the Near-Surface Boundary Layer over Patchy Snow

Présentée le 21 juin 2024

Faculté de l'environnement naturel, architectural et construit
Laboratoire des sciences cryosphériques
Programme doctoral en génie civil et environnement

pour l'obtention du grade de Docteur ès Sciences

par

Michael HAUGENEDER

Acceptée sur proposition du jury

Dr S. Takahama, président du jury
Prof. M. Lehning, Dr R. M. Mott-Grünewald, directeurs de thèse
Dr B. Walter, rapporteur
Prof. T. Sauter, rapporteur
Prof. A. Berne, rapporteur

École
polytechnique
fédérale
de Lausanne

2024

Acknowledgements

This thesis was a great experience and I really want to thank a lot of people.

A huge thanks goes to our scientific family:

"Mama" Rebecca, you have been an excellent supervisor. First of all, thanks for trusting me right from the start of the thesis when I had no clue what we were doing. Throughout the four years, the discussions with you were always enlightening and fun at the same time and helped me deal with a lot of problems. And, at least equally important, you taught me a healthy attitude towards science and work. Samichlaus is happy.

"Papa" Michi has been an equally excellent supervisor. You had a lot of good ideas for how to further proceed and I really liked the discussions with you. They were always helpful, relaxed, and funny at the same time. Thanks for leaving me so much freedom, but still giving enough guidance and a broader context when I was lost in too many details. And of course, thanks a lot for all the great ski tours we did together. A weather station maintainance adventure at Piz Grialetsch right at the beginning, Piz Linard, and Piz Vadret were just a few of them. I am really looking forward to continuing working and ski touring with you.

Thanks a lot to my first and best friend in Davos, Dylan. We, the "Jungs", worked on the same project, shared all the lows and highs, and the best office. Together, we enjoyed many unforgettable moments and adventures. We have done fieldwork, bike rides, mountaineering adventures, and numerous ski tours together. We even had the opportunity to visit the US together (thanks, Rebecca) and had a great time. Thanks, Dylan!

I really enjoyed our biweekly scientific family meetings on Wednesdays, where we discussed the project and developed ideas for how to proceed further or where to go ski touring on the weekend. These meetings were famous across the hallway because of the loud laughs we had together.

I would like to thank Ivana Stiperski for her help throughout the PhD especially with dealing with eddy covariance data. By sharing your eddy covariance processing scripts you helped me getting into the topic and your feedback was always really helpful. Also thanks for the support during HEFEX2, even if not everything went great with my loggers. The trip to the Rockies was really interesting and I could meet a lot of new people. I had the chance to deploy our setup within a big field campaign. Thanks Jessica Lundquist, Tobias Jonas, and Rebecca for enabling

this! Also, thanks to Larissa Schädler, who helped me a lot during the field campaign in spring 2021.
Danke auch an die Werkstatt und Elektronik, und besonders Chasper, Hitsch und Franz für die super Unterstützung bei unseren Setups und die immer schnelle und kompetente Hilfe.
Setting up the LES simulations with only few months left was challenging, but Ocèane Hames and Mahdi Jafari helped a lot and made it possible. Without you it would for sure not have been possible.
Thanks to the Snow Hydrology team at SLF for the support. Thanks, Tobias for your help and support especially with the experimental setup and for getting me a place in the SLF-WG at the very beginning when Corona hit. On the not work-related side, the coffee breaks and dinners together were a pleasure and I felt welcome from the first day on. There were so many nice people who I met on this journey, but I would like to especially thank Amelie, Giulia, Kavitha, Ocèane, Bertrand, Dylan, and Michael for the numerous adventures we had together making the PhD the best part in my life so far. Also a huge thanks to Sophia und Painty for making our WG feel like we were a family.
Danke an die Freunde daheim, wegen denen ich mich jedes mal auch wirklich daheim gefühlt hab, wenn ich daheim war. Vielen Dank, Mama und Papa für die Unterstützung die ganze Zeit! Und Bubas, danke für die vielen schönen Sachen, die wir gemeinsam gemacht haben. Noch eine gute Reise und vielleicht seh ma uns ja demnächst mal wieder. Und zum Schluss danke, Sarah, dass du die ganze Zeit zu mir gehalten hast, auch wenn es nicht immer leicht war.

Davos, 18 April 2024 M. H.

Abstract

The atmospheric layer adjacent to the earth's surface is of crucial importance for weather models due to the exchange of energy between the surface and the atmosphere. This exchange is dependent on the various surface properties and influences the state of the atmosphere at all scales from small-scale turbulence to large-scale weather patterns.

In spring, the melting snow cover becomes patchy, resulting in pronounced surface heterogeneity and significant changes to the overlying atmosphere. This interaction leads to the development of shallow thermal internal boundary layers, profoundly impacting turbulent exchange processes. Our objective is to experimentally access this highly dynamic part of the near-surface atmosphere and gain a more thorough understanding of the sub-meter scale heat advection processes.

For this aim, we developed a novel experimental method. We vertically deploy thin synthetic screens across the transition from bare ground to snow. The screens quickly adapt to ambient temperature and, thus, their surface temperature serves as a proxy for the local air temperature. By filming them with a thermal infrared camera at 30 Hz, we obtain two-dimensional visualizations of the near-surface atmospheric dynamics at a spatial resolution of $\approx 0.5\,\mathrm{cm}$. Additionally, we developed an algorithm to estimate two-dimensional wind speeds by tracking patterns of air temperature. We demonstrate the capabilities of the method by investigating the spatio-temporal dynamics of the stable internal boundary layer (SIBL) adjacent to the snow surface.

We complement these measurements with data from conventional eddy covariance sensors in a comprehensive field campaign in spring. Analysis of the eddy covariance data indicates periods when the stratification above the snow is strong enough to dampen and partly shut down near-surface turbulence. On the contrary, two Föhn events induced pronounced shear-generated turbulent kinetic energy and strong downward heat fluxes. Throughout the melt-out, we observed a decrease in the SIBL depths, resulting in a sign change in the heat fluxes at a given height. Apart from heat fluxes exhibiting opposing signs within and above the SIBL, measurements at different levels reveal a uniform pattern of turbulence within the first few meters above the surface. As more bare ground emerged, a shift towards larger time scales in measured temperature variance occurred, with thermal infrared observations unveiling intermittent advection of plumes of warm air over snow-covered areas.

Finally, we set up a centimeter-scale large eddy simulation over an idealized transition from bare ground to snow. We force the simulation with 20 Hz wind speed measurements. We validate the model by comparing it to eddy covariance measurements. While the simulated horizontal wind speed and air temperature exhibit very good agreement with the measurements, there is a lack of representation of vertical motion, especially for higher frequencies. Nevertheless, we show by comparison with screen measurements that the model is capable of resolving important flow features such as the intermittent advection of warm air over snow. We show that higher wind speeds lead to shallower SIBLs. Moreover, the local surface topography has an influence on the heat fluxes through local flow modification and induces the decoupling of a thin stable layer adjacent to the snow surface.

The work opens the way towards a better representation of surface exchange in larger scale models.

Key words: Atmospheric Boundary Layer, Near-Surface Heat Exchange, Heat Advection, Internal Boundary Layer, Eddy Covariance, Two-Dimensional Measurements, Large Eddy Simulation, Patchy Snow, Snow Melt

Zusammenfassung

Die an die Erdoberfläche angrenzende atmosphärische Schicht ist wegen des Energieaustauschs zwischen der Oberfläche und der Atmosphäre von entscheidender Bedeutung für Wettermodelle. Dieser Austausch hängt von den verschiedenen Oberflächeneigenschaften ab und beeinflusst den Zustand der Atmosphäre auf allen Skalen, von kleinskaliger Turbulenz bis hin zu großräumigen Wetterlagen.

Im Frühling wird die schmelzende Schneedecke fleckig, was zu einer ausgeprägten Oberflächenheterogenität und signifikanten Veränderungen in der darüber liegenden Atmosphäre führt. Die Interaktion führt zur Entwicklung flacher thermaler interner Grenzschichten, die die turbulenten Austauschprozesse maßgeblich beeinflussen. Unser Ziel ist es, diesen hochdynamischen Teil der bodennahen Atmosphäre experimentell zu erfassen und ein gründlicheres Verständnis der Wärmeadvektionsprozesse im Submeterbereich zu gewinnen.

Zu diesem Zweck haben wir eine neuartige experimentelle Methode entwickelt. Wir verwenden dünne, synthetische Leinwände, die wir vertikal über dem Übergang von Wiese zu Schnee aufspannen. Das Leinwandmaterial gleicht sich schnell der Umgebungstemperatur an, weshalb die Oberflächentemperatur der Leinwand näherungsweise der lokalen Lufttemperatur entspricht. Indem wir die Leinwände mit einer thermografischen Infrarotkamera mit 30 Hz filmen, erhalten wir zweidimensionale Visualisierungen der bodennahen atmosphärischen Dynamik mit einer räumlichen Auflösung von etwa 0.5 cm. Zusätzlich haben wir einen Algorithmus entwickelt, um zweidimensionale Windgeschwindigkeiten aus sich bewegenden Mustern der gemessenen Temperatur zu schätzen. Mit dieser Methode untersuchen wir die räumliche und zeitliche Dynamik einer stabilen internen Grenzschicht (SIBL) direkt über der Schneeoberfläche und zeigen damit eine Anwendungsmöglichkeit auf.

Diese Messungen ergänzen wir durch Daten von konventionellen Eddy-Kovarianz-Sensoren in einer umfassenden Feldkampagne im Frühling. Die Analyse der Eddy-Kovarianz-Daten zeigt Perioden, in denen die Stabilität über dem Schnee stark genug ist, um die bodennahe Turbulenz zu dämpfen und teilweise sogar zu unterdrücken. Im Gegensatz dazu führten zwei Föhnereignisse zu ausgeprägter, durch Scherung erzeugter turbulenter kinetischer Energie und starken abwärts gerichteten Wärmeflüssen. Während des Schneeschmelzens beobachteten wir eine Abnahme der SIBL-Höhen gekennzeichnet von einem Vorzeichenwechsel der Wärmeflüsse auf einer bestimmten Höhe. Abgesehen davon, dass die Wärmeflüsse innerhalb und oberhalb der SIBL entgegengesetzte Vorzeichen aufweisen, zeigen Messungen auf ver-

schiedenen Höhen ein gleichmäßiges Muster der Turbulenz innerhalb der ersten paar Meter über der Oberfläche. Mit zunehmender Ausaperung kam es bei der gemessenen Temperaturvarianz zu einem Übergang zu größeren Skalen, wobei die thermografischen Infrarotbeobachtungen intermittierende Warmluftadvektionen über schneebedeckte Gebiete aufdeckten.
Schließlich setzen wir eine Large-Eddy-Simulation im Zentimetermaßstab über einem idealisierten Übergang von Wiese zu Schnee auf. Wir treiben die Simulation mit 20 Hz Windgeschwindigkeitsmessungen an und validieren sie, indem wir sie mit Eddy-Kovarianz-Messungen vergleichen. Während die simulierten horizontalen Windgeschwindigkeiten und Lufttemperaturen eine sehr gute Übereinstimmung mit den Messungen zeigen, fehlt es insbesondere bei höheren Frequenzen an einer Darstellung der vertikalen Bewegung. Dennoch können wir anhand des Vergleichs mit thermographischen Infrarotmessungen der Leinwände zeigen, dass das Modell in der Lage ist, wichtige Strömungsmerkmale wie die intermittierende Advektion warmer Luft über Schnee aufzulösen. Wir zeigen, dass höhere Windgeschwindigkeiten zu flacheren SIBLs führen. Darüber hinaus hat die Geländetopografie einen Einfluss auf die Wärmeflüsse durch lokale Strömungsmodifikation und führt zur Entkopplung einer dünnen stabilen Schicht direkt oberhalb der Schneeoberfläche.
Diese Arbeit ebnet den Weg zu einer besseren Darstellung des Oberflächenaustauschs in größerskaligen Modellen.

Stichwörter: Atmosphärische Grenzschicht, Wärmeaustauschprozesse, Interne Grenzschicht, Eddy Kovarianz, Zweidimensionale Messungen, Large Eddy Simulation, Schneefelder, Schneeschmelze

Contents

Acknowledgements **i**

Abstract **iii**

1 Introduction **1**

Introduction **1**

1.1 Turbulent Exchange 2
  1.1.1 Turbulent Fluxes 2
  1.1.2 Monin–Obukhov Similarity Theory 2
1.2 Energy Balance of a Melting Continuous Snow Cover 3
1.3 Patchy Snow Covers 4
  1.3.1 Development of a Patchy Snow Cover 4
  1.3.2 Energy Balance of A Patchy Snow Cover 4
1.4 Large Eddy Simulation 6
1.5 Objectives and Outline 8

2 A Novel Method to Quantify Near-Surface Boundary-Layer Dynamics at Ultra-High Spatio-Temporal Resolution **11**

2.1 Introduction 12
2.2 Methods 13
  2.2.1 Screen Set-Up 15
  2.2.2 Wind Field Approximation 17
  2.2.3 Turbulence Measurements 22
2.3 Results and Discussion 23
  2.3.1 Near-Surface Atmospheric Layer Structure Information Gained from an Infrared Frame 23
  2.3.2 Vertical Profiles of Temperature and Estimated Wind Speeds 25
  2.3.3 Validation Using Wind Measurements 30
2.4 Conclusion and Outlook 32

3 Turbulence in the Strongly Heterogeneous Near-Surface Boundary Layer over Patchy Snow **35**

3.1 Introduction 36

3.2 Methods 38
3.2.1 Study Site and Data Collection 38
3.2.2 EC Data Preparation 42
3.2.3 Multi-Resolution Flux Decomposition 43
3.3 Meteorological Conditions 45
3.3.1 Weather Pattern 45
3.3.2 Flow Regimes 47
3.4 Separation of Turbulent and Non-Turbulent Motions 48
3.5 Evolution of Turbulence During the Melt Out 50
3.5.1 Föhn 50
3.5.2 Period 1: Deep Stable Internal Boundary Layer 52
3.5.3 Period 2: Diurnal variations 53
3.5.4 Comparison: High Versus Low Snow Cover Fraction 56
3.5.5 Vertical Profiles of Turbulence 56
3.5.6 Near-Surface Eddy Covariance Measurements 61
3.6 Conclusion and Outlook 63

4 Large Eddy Simulation of Near-Surface Boundary Layer Dynamics over Patchy Snow 67
4.1 Introduction 68
4.2 Methods 70
4.2.1 Study Site 70
4.2.2 LES 72
4.2.3 Model Setup and Forcing 73
4.3 Validation of Model Results Against Measurements 75
4.4 Characterization of Near-Surface Boundary Layer Dynamics 78
4.4.1 Intermittent Advection 78
4.4.2 Buoyancy Fluxes and Stable Internal Boundary Layer Growth 80
4.4.3 Near-Surface Boundary Layer For Low and High Wind Speeds 82
4.5 Conclusions, Limitations, and Outlook 86

5 Conclusions, Limitations, and Outlook 89

A Supplementary Material for Chapter 2 95
A.1 Spectral Density 95
A.2 Real Time Near-Surface Atmosphere Dynamics (Video) 95

B Supplementary Material for Chapter 3 97
B.1 Spectra For All Sensors 97
B.2 Föhn Diagnosis 97
B.3 Multi-Resolution Flux Decomposition For All EC Sensors 100
B.4 Real Time Near-Surface Atmosphere Dynamics (Video) 100

Bibliography 113

Curriculum Vitae **115**

1 Introduction

Weather is "the state of the [...] atmosphere at a particular time and place" [I]. This state is influenced the exchange of energy and mass between the atmosphere and the underlying surface within the Atmospheric Boundary Layer (ABL). Stull, 1988 defines the ABL as "that part of the troposphere that is directly influenced by the presence of the earth's surface and responds to surface forcing with a timescale of about an hour or less". The energy exchange processes between the surface and the overlying ABL, especially above a heterogeneous surface are manifold. For example, different surface temperatures induce inhomogeneous near-surface air temperatures. Thermal flows develop, which horizontally distribute heat to equilibrate contrasts. Consequently, the energy balance of the surface at a specific location does not only depend on the local state of the ABL and the surface but also on their upwind properties. In mountainous terrain, the surface modifies the flow and thus adds further complexity to this exchange.

An extreme example of strong surface contrasts in mountainous terrain is a patchy snow cover. Warm patches of bare ground coexist directly adjacent to snow-covered areas. The resulting atmospheric heat exchange processes are spatially strongly heterogeneous on sub-meter scales and highly dynamic. The surface heterogeneities have implications on the energy balance of the melting snowpack, which is of crucial importance for snowhydrological models (Mott et al., 2023a). These models help to accurately predict flooding hazards (D. Li et al., 2019; Sui & Koehler, 2001; Würzer et al., 2016) or hydropower generation potential (Magnusson et al., 2020; Stucchi et al., 2019). Furthermore, the strong contrasts in surface temperature and the resulting heat exchanges with the near-surface heat exchange might also affect the overlying atmosphere.

[I] https://www.britannica.com/dictionary/weather, accessed on 27.03.2024

1.1 Turbulent Exchange

1.1.1 Turbulent Fluxes

A crucial part of the energy exchange between the surface and the atmosphere within the SIBL is turbulent exchange, which is magnitudes stronger than diffusion. Turbulence is characterized by significant and irregular variations of the flow velocity in space and time (Pope, 2000). In the ABL, we can quantify turbulent motion as fluctuations in wind speed around a mean. We describe the wind speed using the three components u, v, and w according to the three cartesian directions x, y, and z. Obviously, the definition of an averaging interval length to calculate the mean has an influence on the turbulent properties. Vickers and Mahrt, 1997 propose a gap in the spectrum of a turbulent quantity marked by low spectral energy densities. This gap scale separates turbulent higher frequency motions from larger, (sub-) meso-scale motion and is referred to as Reynolds averaging time.

In this work, we focus on the kinematic flux of sensible heat $\overline{w'T'}$ as the covariance between fluctuations in vertical wind speed w and air temperature T. With the density of air ρ_{air} and the heat capacity at constant pressure c_p, kinematic flux can be converted to fluxes of sensible heat H by

$$H = \rho_{air} \cdot c_p \cdot \overline{w'T'} \approx 10^3\,\mathrm{kg\,K^{-1}\,m^{-1}\,s^{-2}}\,\overline{w'T'}. \tag{1.1}$$

1.1.2 Monin–Obukhov Similarity Theory

Regional, national, or even global scale numerical weather prediction models offer a spatial resolution not finer than 1 km. Even state-of-the-art downscaling approaches only allow for a grid spacing down to several decameters on the regional scale. Therefore, turbulent exchange, which usually takes place at spatial scales of $\mathcal{O}\left(10^{-3}\,\mathrm{m} - 10^{3}\,\mathrm{m}\right)$ can not be resolved. Consequently, turbulent fluxes need to be parameterized. Close to the surface, the vast majority of weather models use the Monin–Obukov Similarity Theory (MOST) (Monin & Obukhov, 1954) that relates estimations for turbulent fluxes to gradients. For example, the turbulent vertical flux of sensible heat is parameterized as

$$H_{MO} = \rho_{air} c_p C_H \overline{u} \Delta T. \tag{1.2}$$

C_H denotes a stability dependent exchange coefficient, $\overline{u}$ is the mean horizontal wind speed and $\Delta T = T_1 - T_S$ is the air temperature difference between the first model level and the surface.

MOST builds on the basic assumptions of stationary turbulence and a horizontally homogeneous and flat surface, which are clearly violated in mountainous terrain. Various adaptions have been suggested to still allow the applicability of MOST even in complex terrain (e.g. González-Herrero et al., 2024; Schlögl et al., 2017b; Sigmund et al., 2022; Stiperski & Calaf, 2023). Still, especially during patchy snow cover causing an extreme surface heterogeneity, there is a distinct mismatch between modelled and observed heat fluxes (Schlögl et al., 2017b) resulting in erroneous estimations of the energy exchange between the surface and the atmosphere. A more thorough understanding of the spatio-temporal heterogeneity of the near-surface atmosphere is necessary to alleviate the mismatch between modelled and observed heat exchange.

1.2 Energy Balance of a Melting Continuous Snow Cover

Snowmelt is determined by the energy balance of the snowpack. The change of internal energy $\frac{\mathrm{d}E}{\mathrm{d}t}$ of the snowpack is related to various inputs by

$$-\frac{\mathrm{d}E}{\mathrm{d}t} = E_S + E_L + E_H + E_E + E_A + E_G. \tag{1.3}$$

E_S denotes net short-wave radiation. It can be calculated by subtracting the reflected from the incoming short-wave radiation. E_S depends on cloud cover, shading or reflections of surrounding terrain, and the albedo of the snow determining the fraction of reflected radiation. During daytime net short-wave radiation usually contributes the most to the increase in internal energy of the snow.

E_L is the net longwave radiation describing the difference between downward and upward longwave radiation. Longwave radiation is described by the Stefan-Boltzmann law

$$E_L = \epsilon \sigma T_S^4 \tag{1.4}$$

and depends on the object's emissivity ϵ, the Stefan-Boltzmann constant $\sigma \approx 5.67 \times 10^{-8}\,\mathrm{W\,m^{-2}\,K^{-4}}$, and the surface temperature T_S. The strong dependence on the surface temperature is particularly noteworthy. Upward longwave emission is determined by the temperature of the snow surface, while downward longwave emission depends on the temperature of the clouds and surrounding terrain or vegetation.

E_H expresses the turbulent flux of sensible heat due to the temperature differences between the surface and the adjacent atmosphere. Similarly, E_E indicates the turbulent flux of latent heat, which is determined by variations in moisture and connected phase changes such as sublimation, condensation, or evaporation. We provide more detail about turbulent fluxes, especially sensible heat fluxes, in Sect. 1.1.

E_A stands for the energy that is transferred to the snowpack by precipitation or blowing snow and therefore has a strong link to the mass balance. Ultimately, E_G denotes the heat flux from the ground into the snow.

At the beginning of the melt, the additional energy input is used to heat the snowpack until it is isothermal at the melting point at 0 °C. After that, any additional energy is transferred into the phase change from solid (snow) to liquid (water).

1.3 Patchy Snow Covers

1.3.1 Development of a Patchy Snow Cover

Mountain snow cover is spatially highly heterogeneous driven by processes during snow accumulation and ablation. The heterogeneity spans across multiple scales and can be observed as scale breaks in spectral analysis of snow depth (Deems et al., 2006; Schirmer & Lehning, 2011; Trujillo et al., 2007).
During accumulation, on scales of a few kilometers to hundreds of kilometers, large-scale topography, climate (Clark et al., 2011; Marty et al., 2023; Moreno et al., 2008), and orographic precipitation (Colle et al., 2013; Houze, 2012) influence the pattern of snow accumulation. On smaller scales of hundreds to thousands of meters, local topography, such as ridges and valleys, influences the depth of the snow. According to the review of Mott et al., 2018, one can distinguish between pre- and post-depositional processes. Pre-depositional effects include local snowfall enhancement through the so-called seeder-feeder mechanism (e.g. Minder et al., 2008) and preferential deposition (Lehning et al., 2008). After snow has reached the ground, wind-driven transport (Föhn & Meister, 1983; Pomeroy & Gray, 1995) and avalanches reshape local snow depths by redistribution (Pomeroy & Gray, 1995; Quéno et al., 2023). Wind-driven transport leads to smoothing of the local terrain (Schirmer et al., 2011).
The heterogeneity of snow depths is further increased in the ablation phase, when spatially variable energy input modifies the continuous snow cover (Grünewald et al., 2010; Pohl et al., 2006). Incoming short-wave radiation is attenuated by the local cloud cover. The terrain influences the locally incoming short-wave radiation by shading or reflection. Furthermore, due to vegetation and cloud formation, the net longwave radiation is also heterogeneous.
A combination of all these processes in both the accumulation and the ablation phase induces the development of a patchy snow cover later in spring.

1.3.2 Energy Balance of A Patchy Snow Cover

As soon as the first bare patches emerge, surface temperatures become strongly heterogeneous. Due to the lower albedo, bare ground absorbs more energy than snow and, thus, heats up. In contrast, the surface temperature of snow is limited by its melting point at 0 °C. Taking into account the resulting warming effect on the adjacent atmosphere, Schlögl et al., 2018a report an increase in daily snow ablation rates by 22 – 40%. The increased ablation rates lead to the appearance of more bare ground and, thus, to an even stronger warming of the near-surface atmosphere. This snow-albedo feedback strongly influences the melt rates throughout the late ablation season (Letcher & Minder, 2015; Ménard et al., 2014a; Mott et al., 2015; Schlögl et al., 2018b). Extreme surface temperature differences lead to a strong horizontal flux divergence. Over bare ground, the warm surface induces a statically unstable stratification in line with positive (upward) sensible heat fluxes. Over the snow, however, the cold surface and a warmer overlying atmosphere lead to a statically stable stratification and negative (downward) heat fluxes.

The surface heterogeneity interacts with winds on different scales. For example, the diurnal valley wind system is influenced by an elevation gradient of the snow cover as lower elevations are already snow-free, whereas higher up, the snow cover is still continuous. This gradient can even completely change the direction of the valley wind (Segal et al., 1991) and lead to katabatic flows, as similarly observed in glacierized areas (Sauter & Galos, 2016). Mott et al., 2015 highlight the strong dependence of the energy input into the snow surface on the local flow pattern. While local katabatic winds can protect the snow surface from the warm atmosphere above, larger-scale flows advect additional heat from bare ground over the snow surface.

Stable Internal Boundary Layer

This local scale advection leads to the formation of overlapping thermal internal boundary layers with different stabilities. In general, internal boundary layers develop downwind of sudden transitions in surface properties (Garratt, 1990). Above snow, the cold air directly adjacent to the surface and the advected warm air above induce a stable stratification, and thus a stable internal boundary layer (SIBL). We define its upper boundary by a sign change of the heat fluxes. Within the SIBL, negative fluxes prevail, while above the SIBL the near-surface advection of warm air induces positive fluxes.

The SIBL growth adjacent to snow patches was investigated by a few studies. Takahara and Higuchi, 1985b and Granger et al., 2006, for example, measured vertical profiles of air temperature to infer the SIBL depth. In agreement with Brutsaert, 1982b, they suggest a power law dependence of the fetch distance. However, their definition of the upper SIBL boundary slightly differs from ours, as they define the top of the SIBL where air temperature profiles from up and downwind of the transition from bare ground to snow overlap. Using three-dimensional ultrasonic wind speed sensors, buoyancy fluxes can be calculated using the eddy-covariance (EC) method. This data can inform about the SIBL at the sensor location. However, the result is only binary: Either the sensor is below (negative buoyancy fluxes) or above (positive fluxes) the SIBL top. Deploying EC sensors at multiple heights, e.g. Mott et al., 2013 and Harder et al., 2017 estimated the SIBL depth at a fixed location over a snow patch. Aerial (two-dimensional) measurements across the transition from bare ground to snow to quantify the spatio-temporal dynamics remain a challenge and will be addressed in this work.

Modeling Approaches

For snowhydrological modeling it is important to quantify the additional energy input into the patchy snow surface from the aforementioned processes. However, the scales of the exchange processes are too small to be directly represented by any numerical weather prediction model. Therefore, they need to be parameterized as a function of variables available on a coarser scale. An essential part of the quantification is the sub-grid scale snow cover fraction. Helbig, Bühler, et al., 2021 and Helbig, Schirmer, et al., 2021 developed a parameterization using sub-grid terrain descriptors together with modelled snow height and snow water equivalent at the peak of winter.

There are a few approaches to estimating the effect of warm air advection over snow. For example, Marsh and Pomeroy, 1996; Neumann and Marsh, 1998; Pohl et al., 2006 used an empirical bulk transfer parameter to determine how much heat above bare ground is transported over snow. Their calculations indicate that heat fluxes contribute up to 28% of the energy available for melt in the late ablation season. However, they uniformly distribute the additional energy over the snow surface, neglecting the observed fetch dependence. Furthermore, their efficiency parameter only depends on the bare and snow-covered areas and an estimation of heat fluxes over the bare surface. Therefore, they do not include essential dependencies as for example on local wind speed. Additionally, the bulk efficiency parameter does not include small-scale stability effects as the development of SIBLs possibly protects the snow surface from the warm air aloft.

Essery et al., 2006 and Granger et al., 2002 developed a more complicated boundary layer integration approach, where they integrate the temperature differences between upwind and downwind profiles to estimate the energy input to the snow surface. Their approach relies on fine-scale vertical temperature profiles available above bare ground and at multiple fetch distances over snow, which is not achievable for coarser (i.e. hectometer) scale models with the first atmospheric model levels a few meters above the surface.

More recently, Schlögl et al., 2018a suggested a temperature footprint approach to account for spatial variabilities in the upwind surface temperature. The shortcoming of this approach is that it requires precise knowledge about the distribution of snow-covered and snow-free areas and a high-resolution wind field input to estimate the temperature footprints.

All these approaches suffer from drawbacks that prevent a ready-to-use implementation in country-scale hydrological or weather models. To overcome the drawbacks and bridge the gap between meter-scale heat exchange processes and hectometer-scale models, more comprehensive field data is necessary. Especially, the dynamic interplay between layers of different stability at the transition from bare ground to snow needs to be further experimentally investigated to find possible implications for future parameterizations.

1.4 Large Eddy Simulation

In order to generalize point-based or even two-dimensional measurements to larger domains, numerical modeling is inevitable. The basis for most computational fluid dynamic models are the Navier-Stokes equations that describe and predict the evolution of the three velocity components $u_j,\ j = x, y, z$. In the following, we use the Einstein summation convention to simplify the notation. In their incompressible form and under the Boussinesq approximation, the Navier-Stokes equations can be written as (Pope, 2000)

$$\frac{\partial u_i}{\partial t} + u_j \frac{\partial}{\partial x_j} u_i = \nu \frac{\partial^2 u_i}{\partial x_j \partial x_j} - \frac{1}{\rho}\frac{\partial p}{\partial x_i} - \delta_{iz} g \alpha \Delta T. \tag{1.5}$$

ν denotes the kinematic viscosity, ρ is the density of the fluid, p the pressure including gravitational effects, g the gravitational acceleration, α the thermal expansion coefficient, and $\Delta T = T - T_0$ the temperature difference relative to a reference temperature T_0. The last term in (1.5) describes the effect of buoyancy on the flow under the Boussinesq approximation. It introduces an additional unknown, T, which can be solved for utilizing energy conservation. Keep in mind, that (1.5) is a coupled system of three partial differential equations with five unknowns. In order to be able to uniquely solve this system, the continuity equation

$$\frac{\partial u_i}{\partial x_i} = 0 \tag{1.6}$$

and an equation for energy conservation are necessary. In order to simplify the description in the following, we neglect the last term in (1.5).

Conceptually the easiest way to solve (1.5) together with (1.6) is Direct Numerical Simulation (DNS), where turbulence is resolved on all scales. The solution is one possible exact representation of the flow. However, the benefit of perfectly resolving all flow features comes with the caveat of tremendous computational costs. Therefore, DNS can only be applied to special, usually idealized cases with low Reynolds numbers. For example, van der Valk et al., 2022 set up idialized DNS simulations to study the effect of heat advection in patchy snow conditions. From their simulations, they estimate that 60 – 80% of the energy input to the snow surface stems from of turbulent fluxes. Furthermore, they could see an increase in melt rates at the leading edge of the snow patch, which was also observed in experimental studies (e.g. Mott et al., 2011, 2017; Schlögl et al., 2018b).

Another way of solving (1.5) and (1.6) is to spatially average the equations and obtain the Reynolds Averaged Navier-Stokes (RANS) equations. This approach allows the treatment of any flow situation by prescribing a suitable averaging length. However, as the name suggests, the solution only describes averaged flow properties and does not resolve turbulence at small scales.

A compromise between DNS and RANS with achievable computational demands and a direct resolution of at least larger turbulence structures are Large Eddy Simulations (LES). By filtering (1.5), resolved, larger scales are separated from non-resolved sub-filter scales. The filter can take on various shapes and width, such as a Gaussian or spectral cut off filter. After filtering, (1.5) writes as

$$\frac{\partial \overline{u_i}}{\partial t} + \frac{\partial \overline{u_i u_j}}{\partial x_j} = \nu \frac{\partial^2 \overline{u_i}}{\partial x_j \partial x_j} - \frac{1}{\rho} \frac{\partial \overline{p}}{\partial x_i}. \tag{1.7}$$

Filtered quantities are denoted by overbars. (1.7) has a similar form as (1.5) except for the last term, that we neglected. The only difference is the second term, which poses a difficulty. $\overline{u_i u_j}$ is the filtered product of two unfiltered quantities, which are a priori unknown. In order to close the set of equations, this term has to be parameterized. In this work, we mainly use the Smagorinsky-Lilly Sub-Grid-Scale model (Smagorinski, 1963) that assumes a linear relation between the anisotropic stress tensor and the filtered rate of strain. For further details, we refer the reader to Sect. 4.2.2.

1.5 Objectives and Outline

As detailed above, a relevant contribution to the energy balance of a melting snow patch comes from heat fluxes. A thorough understanding of the near-surface heat exchange processes is essential to accurately predict the runoff from snow melt in spring and the effect of the strongly heterogeneous surface on the overlying atmosphere. However, the highly heterogeneous surface and near-surface boundary layer over patchy snow, in combination with the strongly dynamic mixing by various flows, makes it formidable to experimentally investigate this layer. While previous studies exist, further comprehensive field data is necessary to understand the sub-meter scale heat exchange processes close to the surface. The existing limitations of fixed-location data, such as temperature profiles or turbulence measurements, pose challenges in comprehensively understanding three-dimensional exchange processes. In an attempt to fill these gaps, this thesis addresses the following research questions:

- How can we experimentally observe and analyse the spatio-temporal evolution of the highly dynamic atmospheric layer adjacent to the snow surface?
- How do the dynamics of the near-surface boundary layer influence heat exchange processes over a patchy snow cover, and what are the implications of their spatio-temporal variability?
- Can we employ high-resolution modeling to spatially extrapolate experimental findings and generalize local measurements to larger domains and diverse settings?

To answer these questions, the thesis is structured as follows:

- In Chapter 2 we present a novel method to quantify the near-surface atmospheric layer. A thermal infrared camera points at thin synthetic screens that are deployed vertically and are aligned with the prevailing wind direction. The screens quickly adapt to ambient temperatures and, therefore, their surface temperature serves as a proxy for the local air temperature. The method offers a spatial resolution of < 1 cm and a temporal resolution of 30 Hz. In addition to spatial information on temperatures, by tracking patterns of temperatures, we can deduce estimates of two-dimensional wind speeds. We compare the data with conventional EC measurements.
- In Chapter 3, we complement results obtained from this method with multiple EC measurements to infer the temporal change of the near-surface boundary layer during a three week period in the melt season. From the EC sensors, we calculate the buoyancy fluxes, sonic temperature variances and the turbulence kinetic energy. By analyzing spectra of those variables, we obtain information about the relevant scales for the heat exchange processes. Based on this data, we differentiate two different periods interrupted by two Föhn events. Furthermore, we could see that warm air from bare patches is intermittently advected over the snow surface.

- In Chapter 4 we aim at generalizing our previous results using a centi-meter resolution LES model. We simulated the flow across a single, idealized transition from bare ground to snow using a inflow-outflow configuration. A novelty of this study is the direct forcing with high-frequency EC data. We validate the model with independent measurement data. Similar to the previous Chapter, we observe intermittently advected plumes of warm air. Furthermore, we use the simulation output to investigate SIBL properties. Separating periods with high and low wind speeds, we can show that SIBLs are shallower for lower wind speeds.
- Finally, in Chapter 5 we draw general conclusions, discuss limitations and give an outlook for future research.

2 A Novel Method to Quantify Near-Surface Boundary-Layer Dynamics at Ultra-High Spatio-Temporal Resolution

This chapter corresponds to the postprint version of the article published as

Haugeneder, M., Lehning, M., Reynolds, D., Jonas, T., Mott, R.: A Novel Method to Quantify Near-Surface Boundary-Layer Dynamics at Ultra-High Spatio-Temporal Resolution, *Boundary-Layer Meteorology* 186, 177–197 (2023). https://doi.org/10.1007/s10546-022-00752-3

Abstract

The lateral transport of heat above abrupt (sub-)metre-scale steps in land surface temperature influences the local surface energy balance. We present a novel experimental method to investigate the stratification and dynamics of the near-surface atmospheric layer over a heterogeneous land surface. Using a high resolution thermal infrared camera pointing at synthetic screens, a 30 Hz sequence of frames is recorded. The screens are deployed upright and horizontally aligned with the prevailing wind direction. The screen's surface temperature serves as a proxy for the local air temperature. We developed a method to estimate near-surface two-dimensional wind fields at centimetre resolution from tracking the air temperature pattern on the screens. Wind field estimations are validated with near-surface three-dimensional short-path ultrasonic data. To demonstrate the capabilities of the screen method, we present results from a comprehensive field campaign at an alpine research site during patchy snow cover conditions. The measurements reveal an extremely heterogeneous near-surface atmospheric layer. Vertical profiles of horizontal and vertical wind speed reflect multiple layers of different static stability within 2 m above the surface. A dynamic, thin stable internal boundary layer (SIBL) develops above the leading edge of snow patches protecting the snow surface from warmer air above. During pronounced gusts the warm air from aloft entrains into the SIBL and reaches down to the snow surface adding energy to the snow pack. Measured vertical

turbulent sensible heat fluxes are shown to be consistent with air temperature and wind speed profiles obtained using the screen method and confirm its capabilities to investigate complex in situ near-surface heat exchange processes.

2.1 Introduction

A precise understanding of the seasonal snow cover dynamics is of crucial importance for various applications (Lehning, 2013). Snow melt and its timing has impacts on the ecosystem (Wheeler et al., 2016), the climate and water availability in cold regions (Beniston et al., 2018; Chapin et al., 2005; Cohen & Rind, 1991), and provides drinking water to downstream communities (Sturm et al., 2017). Hydrological forecasts for flood prevention (Wever et al., 2017) or prediction of the hydropower potential (Schaefli et al., 2007) rely on solid knowledge about the snow cover and its spatio-temporal dynamics.

An important driver for snow cover variations is the interaction of the snow surface and the adjacent atmosphere in the form of mass and energy fluxes (Mott et al., 2018). The energy exchange becomes especially important when the snow cover becomes patchy. Incoming shortwave radiation and a lower surface albedo leads to a warming of bare ground. Melting snow patches, however, remain at 0°C. The resulting strong spatial heterogeneity of surface temperatures interacts with the atmospheric flow at different scales and increases the turbulent exchange of sensible and latent heat towards the snow cover (Letcher & Minder, 2017; Liston, 1995; Mott et al., 2013; Schlögl et al., 2018b). The crucial question in this context becomes: how much of the laterally advected heat reaches the snow surface and leads to an input in the snow pack's energy balance (Harder et al., 2017; Ménard et al., 2014a; Mott et al., 2017; Mott et al., 2015)? Furthermore, interactions between the atmospheric flow field and heat exchange processes over the melting surface occur not only in spring snowmelt, but also influence the melt of glaciers and, thus, their mass balance (Mott et al., 2020).

Few experimental campaigns have been carried out to assess this research question. Granger et al., 2006 measured vertical profiles of air temperatures over bare ground and snow patches. Using their data they give a best-fit approximation for the growth of a stable internal boundary layer developing over the snow surface (Garratt, 1990). Mott et al., 2016 conducted wind-tunnel experiments to study the influence of the topography on the atmosphere close to the snow surface. They point to local decoupling in weak wind conditions. The effect of topography on the local wind speed and, thus, the energy balance of the melting snow pack is also found to be significant by Fujita et al., 2010. They investigated the melt of a persistent snow patch over four decades and related it to meteorological observations. Later, Mott et al., 2017 found evidence for atmospheric decoupling in a comprehensive field campaign including various turbulence measurements. Furthermore, the authors point to the importance of the wind on the exchange of sensible heat with the snow surface through the development of internal boundary layers. In an effort to quantify the advection of both sensible and latent heat over snow patches, Harder et al., 2017 measured vertical temperature and humidity profiles at specific locations over the transition from bare ground to snow. They conclude that advected sensible heat has a significant contribution to the energy balance of a melting snow patch. Advection of latent heat, however, strongly depends on the bare soil moisture.

With the available experimental data, several approaches to model the advection of heat and the resulting turbulent heat fluxes have been developed. Essery et al., 2006 and Granger et al., 2002 used a boundary-layer integration model to estimate aerial averages of advected heat by integrating over the temperature difference between an upwind (over bare ground) temperature profile and a profile over the snow patch. Sauter and Galos, 2016 performed large eddy simulations (LES) in order to better represent the small-scale turbulent processes close to the snow surface. Later, Schlögl et al., 2018a developed a temperature footprint approach to estimate the influence of air temperatures close to the surface in the upwind fetch of a grid point. However, modelling the effect of lateral heat advection on the snow melt over a large-scale domain remains an unresolved issue in snow-hydrological modelling.

To address this problem and gain deeper process understanding of snow–atmosphere interactions and feedbacks, further measurements on the sub-metre-scale are necessary. Thermal infrared imaging of a vertical synthetic screen to investigate the near-surface atmosphere can fill this gap. With spatially continuous data across the transition from bare ground to snow, the shortcomings of point-based measurements can be overcome. Grudzielanek and Cermak, 2015a used a similar set-up to investigate nocturnal katabatic and drainage flows. For this study, we further improved the set-up and applied it on a patchy snow cover. With that we are able to retrieve high spatio-temporal resolution air temperature measurements within the atmospheric layer adjacent to the surface. On the basis of Inagaki et al., 2013, who used a time series of thermal images of a sunlit house wall to investigate air motion close to the wall, we developed an algorithm to estimate near-surface wind speeds. In combination with the measured air temperatures, this allows assessment of both the static stratification and the extreme boundary-layer dynamics in the first few metres above the land surface.

In the following chapter, the experimental set-up and the data processing of the thermal infrared data are described. Subsequently, to show the capabilities of the method, the near-surface atmosphere over a patchy snow cover is described qualitatively using an infrared frame. We present a new method for retrieving vertical profiles of the horizontal and vertical wind speed showing the extreme dynamics of the near-surface atmospheric layer. Finally, the estimated wind fields are compared to both reference measurements and calculated turbulent vertical sensible heat fluxes.

2.2 Methods

Experimental data for the analysis on near-surface atmospheric layer dynamics was collected during a comprehensive field campaign in late spring 2021 in the alpine valley of Monbiel (Klosters, Switzerland). Figure 2.1 shows a map of the investigation area along with an image captured by an unmanned aerial vehicle (UAV). Measurements were taken on the slightly

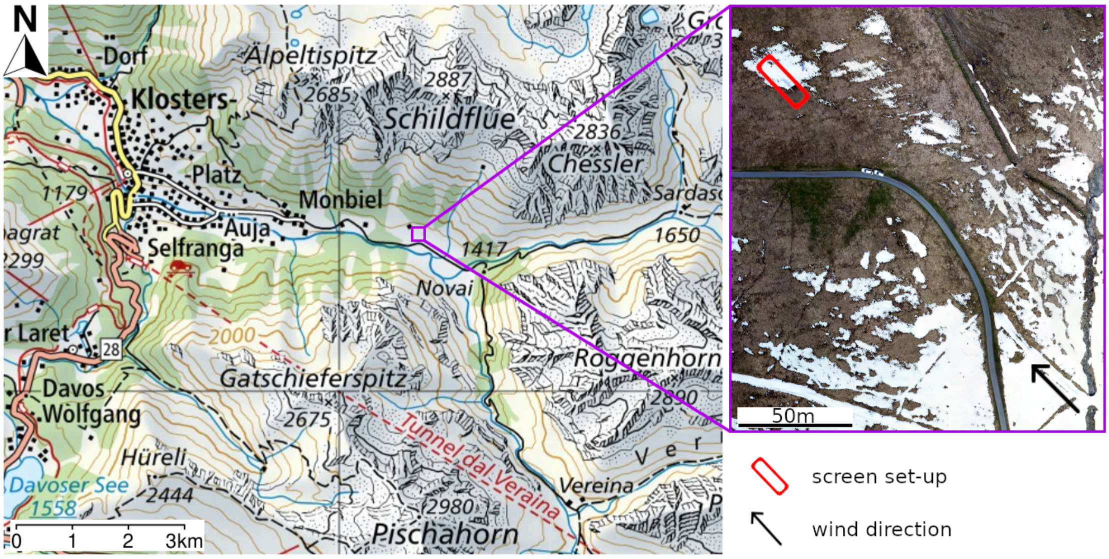
N
Dorf
Klosters
Platz
Älpeltispitz
2685
2887
Schildflue
2836
Chessler
Sardasc
Monbiel
1179
Auja
Selfranga
1417
1650
Novai
Laret
28
2000
Davos
Wolfgang
Gatschieferspitz
Roggenhorn
2890
2675
Tunnel dal Vereina
Hürelli
Davoser See
1558
2444
Vereina
2980
Pischahorn
0 1 2 3km
50m
screen set-up
wind direction

Figure 2.1: The measurement site in the alpine valley of Monbiel (Klosters, Switzerland). On the right a UAV image shows the position of the screen set-up with the upwind fetch. The snow cover fraction of the area shown in the UAV image is SCF= 0.25. Topographic map taken from map.geo.admin.ch

south-exposed valley floor at a height of 1360 m a.s.l. The UAV image in Fig. 2.1 depicts the snow cover at the time of the measurements used for this study. The total snow cover fraction of the area shown in the UAV image was SCF= 0.25. However, SCF was decreasing from south-east to north-west due to the slightly inclined, south-exposed slope in the upper part of the image. On the upwind edge of a snow patch with a size of 20 m × 15 m and a maximum snow depth of $h_s = 0.3$ m the screen set-up was deployed. The snow in the surrounding areas mostly disappeared except for some small patches. The bare ground mainly consisted of alpine meadow with a small paved road 60-m upwind of the screens. The screen method has been developed and tested on multiple different infrared sequences. However, as the primary aim is to demonstrate the capabilities of the screen method, evaluations in this publication stem from a 10-min infrared sequence recorded on 28 April 2021 1200 LT (local time = UTC + 2 h). During the recorded period, multiple gusts advected warm air over the snow surface. Furthermore, measurements of the short-path ultrasonic anemometer close to the screen are available for this period for validation (see Sect. 2.3.3). In future research we plan to analyze the full dataset to more quantitatively asses processes of near-surface heat exchange.

In the following, the screen set-up utilizing a thermal infrared camera is introduced in Sect. 2.2.1. Subsequently, Sect. 2.2.2 describes the data evaluation including a detailed process scheme. Finally, Sect. 2.2.3 gives a brief insight into the conducted turbulence measurements.

2.2.1 Screen Set-Up

The screen set-up (Fig. 2.2a) was adapted from Grudzielanek and Cermak, 2015a, who used it to investigate katabatic flow properties. In order to record a sequence of high spatio-temporal resolution thermal infrared frames, a sun-shielded thermal infrared camera (InfraTec VarioCam HD) was deployed on a tripod and connected to a laptop for recording (marked with ‘1’ in Fig. 2.2a). It points at two vertical screens aligned with the wind direction over the transition of bare ground to snow covered areas (‘2’). The screens are each 2.8-m long and 1.9-m high (for further description see Sect. 2.2.1). A parallel alignment of the screen axis with the wind direction is crucial to avoid artificial vertical movement of air impinging upon the screen for non-parallel flows. Figure 2.2b shows a single infrared frame as an excerpt from a sequence recorded on 23 April 2021 in Monbiel. In the following, the abbreviations ‘TIR camera’ for thermal infrared camera and ‘infrared frame’ for a single frame out of the 10-min sequence are used. As shown in Fig. 2.2a, bare ground (mainly alpine meadow) covers the surface in the upwind fetch of the investigated snow patch. The UAV image in Fig. 2.1 gives an overview of the upwind surface. The area around the screens downwind of the transition

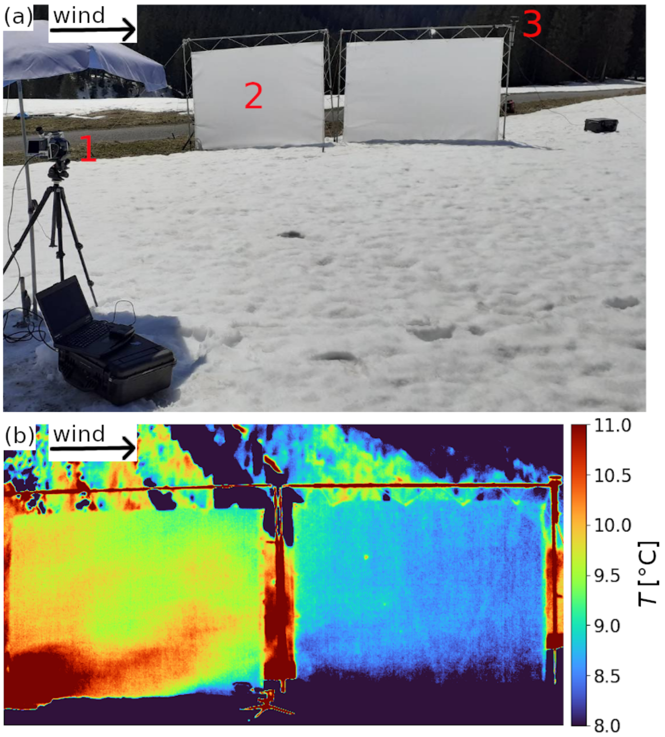

Figure 2.2: **a** Screen set-up used to obtain highly spatio-temporally resolved thermal infrared pictures. 1) Sun-shielded thermal infrared camera, 2) stretched thin synthetic screens, 3) two-dimensional ultrasonic anemometer. **b** Example for a recorded infrared frame. The screen’s surface temperature serves as a proxy for local air temperature and is shown according to the colour bar on the right

is snow covered. The screens cover a wind fetch distance over snow of approximately 5 m. The surface temperature of the screen serves as a proxy for air temperature (Grudzielanek & Cermak, 2015a) and is shown in Fig. 2.2b according to the colour bar. The example infrared frame shows a warm air plume advected by the wind reaching about 1.5 m over the snow patch, while there is still a thin layer of cold air close to the snow surface. The air further downwind is significantly colder. In the background a partly snow covered, forested ridge is visible.

Thermal Infrared Camera

High spatio-temporal resolution thermal frames are recorded by a TIR camera. An uncooled microbolometer in the TIR camera measures the emitted spectral power in a wavelength interval $7.5\,\mu\text{m} \leq \lambda \leq 14\,\mu\text{m}$. To relate the measured spectral power to the surface temperature T_s, the Stefan–Boltzmann law

$$\Phi = \epsilon \sigma T_s^4 \tag{2.1}$$

is used. The emitted power per area is denoted by Φ, the emissivity of the emitting object by ϵ, and the Stefan–Boltzmann constant $\sigma \approx 5.67 \times 10^{-8}\,\text{W}\,\text{m}^{-2}\,\text{K}^{-4}$. The emissivity ϵ is introduced as a material-specific constant. It describes how well the object can be approximated as a perfect black body with an emissivity $\epsilon = 1$. If $\epsilon < 1$, a further correction accounting for reflection and transmission of the surrounding environment can be applied to Eq. 2.1. The screens used in this study have an emissivity of $\epsilon_{screen} = 0.94$ (Grudzielanek & Cermak, 2015a). Due to strong thermal heterogeneities in the surrounding of the screen, further inaccuracies due to transmission and reflection are likely and cannot be corrected. The influence of the atmosphere between the TIR camera and the screens on the transmitted infrared signal is neglected due to the short distance. Furthermore, the analysis in this study only evaluates relative differences in the screen temperatures. Therefore, no corrections are applied.

The detection of surface temperatures with the TIR camera is subject to different sources of artifacts. The most relevant for this study is vignetting. Vignetting is caused by a decrease in illumination of the sensor with increasing off-axis distance due to the optical system (H. Li & Zhu, 2009). In the data the effect is visible as a temperature gradient from the centre towards the periphery of the field of view. Vignetting gets stronger with stronger temperature changes. Its impact is limited by a shutter inside the TIR camera that is moved in front of the microbolometer covering the whole field of view for a fraction of a second. Using the known temperature of the shutter, the microbolometer is recalibrated every 30 s. In the field, it is important that the TIR camera has adapted to ambient temperature before starting to record. To minimize the influence of shortwave radiation on the TIR camera, an umbrella was used as sun protection (see Fig. 2.2A). Furthermore, the preprocessing steps (see Sect. 2.2.2), and in particular the subtraction of a back looking time average, help reducing the effects on the recorded temperature field.

For this study we used an InfraTec VarioCAM HD offering a spatial resolution of 1024 pxl ×

768 pxl to capture boundary-layer dynamics. The TIR camera records infrared frames at 30 Hz. One infrared sequence contains 18000 frames covering 10 min.

Screens and Wind Direction Measurement

The screens consist of a stretched, thin polyester mat with an acrylate coating. The material allows adaption to the ambient air temperature almost instantaneously and, thus, serves as a proxy for the local air temperature (Grudzielanek & Cermak, 2015a). As the screens are not produced for scientific purposes the material shows imperfections such as thickness variations. Furthermore, it is sensitive to contamination with dirt, which changes the reflectivity and the heat capacity. The screens are spanned with an elastic rope in a metal frame to create a trampoline-like set-up, which ensures that the metal structure has a minimal effect on the flow field and the screen temperatures.

A two-dimensional ultrasonic anemometer (WindSonic Gill Instruments, Lymington, UK) is installed on the downwind side of the set-up, ('3' in Fig. 2.2a) mainly providing information about wind direction. This data is used to select time periods where the wind direction is aligned with the screen axis to avoid an influence of the screens on the flow field. For wind directions deviating more than 30° from this axis, substantial flow field disturbances such as up- or downdrafts can be observed. Furthermore, a portable short-path three-dimensional ultrasonic anemometer, deployed close to the surface in vicinity of the screens provides measurements for the validation of screen data.

2.2.2 Wind Field Approximation

The high spatio-temporal resolution of the TIR camera allows for the investigation of boundary-layer dynamics. The air temperature of a plume is used as a marker to observe its motion. The wind field estimation from infrared data (WEIRD) method tracks the pattern caused by air temperature gradients moving over time and estimates a two-dimensional wind field from this. Heterogeneities are induced by the strong differences in surface temperatures between bare ground and snow and the advection of warm air from snow free towards snow covered areas. The resulting air temperature gradients in both the horizontal and the vertical direction allow an approximation of the horizontal and vertical wind speed. Stronger heterogeneities in air temperature yield more reliable estimates of the wind field. The two-dimensional wind field is a projection of the real three-dimensional wind field onto the plane of the screens. A validation of the estimated wind fields is presented in Sect. 2.3.3.

The WEIRD method consists of different preprocessing, processing, and postprocessing steps. The steps are shown in the overview sketch in Fig. 2.3 and explained in detail in the following. Documented source code can be found online (see Sect. 2.4).

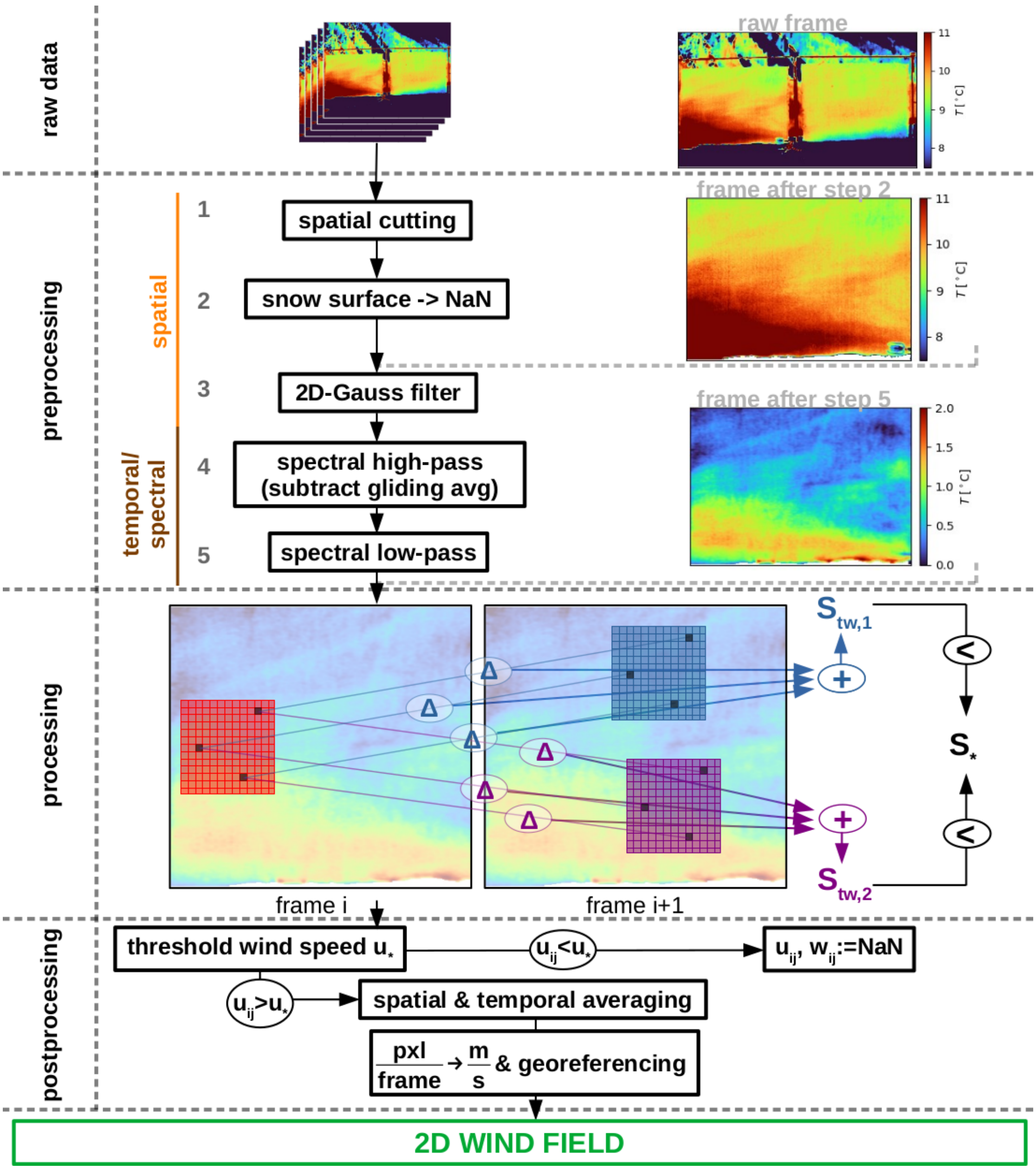
raw data
raw frame
11
10
9
8
T [°C]
preprocessing
spatial
temporal/ spectral
1
spatial cutting
2
snow surface -> NaN
3
2D-Gauss filter
4
spectral high-pass (subtract gliding avg)
5
spectral low-pass
frame after step 2
frame after step 5
2.0
1.5
1.0
0.5
0.0
processing
Δ
+
S_tw,1
S_tw,2
<
S_*
frame i
frame i+1
postprocessing
threshold wind speed u_*
u_ij<u_*
u_ij, w_ij:=NaN
u_ij>u_*
spatial & temporal averaging
pxl/frame → m/s & georeferencing
2D WIND FIELD

Figure 2.3: Sketch of the WEIRD method: The raw infrared sequence is preprocessed in several steps including spatial and temporal filters. In the processing step the correlation between an interrogation window in frame i (red) and multiple spatially shifted target windows in the subsequent frame $i+1$ (blue, purple as two examples) is calculated. The spatial shift between the interrogation window and the target window with the highest correlation is used to calculate the wind speed. The postprocessing includes the application of a threshold wind speed and averaging depending on the desired properties of the two-dimensional wind field. For further details see text

Preprocessing

The goal of the preprocessing is to reduce the noise contained in the infrared frames in order to improve the approximation of the wind speed. The noise mainly stems from imperfections of the screens as well as from artifacts caused by the microbolometer (see Sect. 2.2.1). In the preprocessing the raw infrared data is filtered in both the spatial and the spectral domains. The sequence of preprocessing steps is shown in the upper part of Fig. 2.3. On the right, an example frame is shown as raw data (top), after preprocessing step 2 (middle), and after complete preprocessing (bottom).

The first three preprocessing steps are applied to all infrared frames independently and tackle the spatially distributed noise. Steps 4 and 5 act on the temperature time-series of each pixel and, thus, dampen the temporal or spectral noise. In the following the single steps are described in more detail:

1. The raw infrared sequence is first spatially cut to remove the surrounding environment. Thereby the number of pixels per frame is reduced by 60% and, thus, sufficiently saves computation time for all following steps.

2. Data points representing the snow surface below the screens are set to not-a-number ('NaN') by applying a temperature threshold to every pixel in the lower part of the infrared frame. The value of this threshold depends on the temperature offset of the TIR camera and the angle of view (Pestana et al., 2019) and is set individually for an infrared sequence. It ensures that the wind field can also be evaluated close to the snow surface without artificial influences of the snow surface. In Fig. 2.3 an example of an excerpt from a frame after preprocessing steps 1 and 2 is given on the right side. In contrast to the same frame from the raw infrared sequence shown above, it is cut to screen dimensions and the snow surface is set to NaN (shown by white colour).

3. *Spatially anisotropic Gauss filtering* dampens noise in the spatial domain by smoothing the pixel values. It is applied frame-wise to reduce the vertically aligned and temporally varying artifacts. The anisotropy of the noise is assumed to originate from the column-wise read-out of the microbolometer. To account for the vertical structure, the smoothing over columns (lateral) is stronger than over rows (vertical), i.e., $\sigma_{col} = 2$ pxl and $\sigma_{row} = 1$ pxl.

4. The *subtraction of a back-looking time average* removes effects of low frequency changes. Possible sources include effects caused by the TIR camera such as the temporally changing vignetting. Furthermore, small particles of dirt with different reflectivity and heat capacity than the screens show a different response to incoming shortwave radiation. These effects are dampened by subtracting a back-looking 10-s moving time average similar to a spectral high-pass filter. The resulting data represents temperature fluctuations instead of absolute values.

5. Finally, a *spectral low-pass filter* is applied to each pixel time series. A frequency analysis of the measured temperature data (see Online Resource 1) points to the fact that the screens react to air temperature changes on a time scale of approximately 1 s. Faster changes are strongly damped due to the heat capacity of the screen material and superimposed by random noise. To minimize these influences, a cut-off frequency of $f_{co} = 2\,\mathrm{Hz}$ is chosen for the spectral low-pass filter. The bottom infrared frame on the right side of the preprocessing part in Fig. 2.3 shows the frame after complete preprocessing. Note that the colour bar shows temperature fluctuations T', due to the subtraction of a gliding average in step 4. Also note that the temperature range is 2.0°C in contrast to 3.5°C in both the raw infrared frame and the infrared frame after step 2. The column-wise noise from the previous excerpt is averaged out. However, there is a diagonal line throughout the height of the screen visible. It originates from thickness variations of the screen, probably caused in the manufacturing process.

Processing: Wind Field Estimation Using Thermal Infrared Data

The WEIRD processing step leads to a raw approximation of the two-dimensional wind field in the predefined spatial excerpt of the infrared sequence. Therefore, pairs of two subsequent frames of the preprocessed sequence are analyzed. In the following they are denoted by frame i and frame $i+1$. The time interval between those two frames is given by the temporal resolution of the TIR camera $\Delta t = \frac{1}{30\,\mathrm{Hz}} \approx 3 \times 10^{-2}\,\mathrm{s}$. Vertical wind speed w is defined to be perpendicular, whereas horizontal wind speed u is parallel to the bottom of the infrared frame.

For the following best-correlation-search, both frames are spatially subdivided into windows which are called *interrogation windows* in frame i and *target windows* in frame $i+1$. Because neighbouring windows are shifted by one pixel, they largely overlap. The size of those windows depends on the structure of the observed pattern and, thus, on the structure and dimensions of the investigated near-surface atmospheric layer processes. For our measurement set-up, a parameter study yielded an optimal window size of 10 pxl × 10 pxl (not shown). In Fig. 2.3, interrogation and target windows are shown within the processing part. The red rectangle in frame i denotes an interrogation window. Similarly, the blue and purple rectangles in the right frame symbolize two (out of 300 per interrogation window as in this study) target windows. The grid symbolizes the pixels in this window. To estimate the wind field, correlations between one interrogation window and a set of spatially shifted target windows are calculated. Therefore, values for the maximum shift in positive and negative horizontal and vertical direction need to be defined. These values define the *search region* in frame $i+1$ containing all analyzed target windows for a given interrogation window. For this study the search region is estimated using ultrasonic wind measurements (see Sect. 2.2.3). It is set to be symmetric in vertical direction (−5 pxl to +5 pxl) accounting for a symmetric distribution of the measured vertical wind speeds and with a bias (−5 pxl to 25 pxl) in the direction of the measured horizontal wind speed in horizontal direction. The search region also defines the extent of the estimated wind field towards the upwind, downwind, and top edges of the screen. Only interrogation windows for which all target windows are within the screen extent are considered. Since information on the wind field is of special interest close to the snow surface, the vertical extent of the search region decreases symmetrically towards the surface in the lowest 0.1 m of the screen. This is in accordance with decreasing vertical wind speeds close to the land surface. However, no decrease in the horizontal extent of the search region close to the bottom is applied to allow the detection of low-level jets (Mott et al., 2020).

The wind field approximation for two screens and one time step needs $\mathcal{O}(10^8)$ correlations to be evaluated. Therefore, a computationally efficient algorithm to estimate correlations is adapted from Kaga et al., 1992. This algorithm finds the best correlation between a given interrogation window and one out of the set of target windows by accumulating differences between corresponding pixels step by step for each target window. Once the sum exceeds a defined threshold, the respective target window is not considered anymore. The last remaining target window is assumed to have the highest correlation with the interrogation window. This search is done in three steps (Kaga et al., 1992):

1. The accumulated absolute difference $S_{tw,k}$ between $n_{ini} = 10$ random pixels in the interrogation window and all target windows k is evaluated. $S_{tw,min}$ denotes the minimum of all $S_{tw,k}$ values.

2. The threshold S_* for aborting the correlation search is set as

   $$S_* = \alpha S_{tw,min} \cdot \frac{x_w}{n_{ini}},$$

   with α a constant and $x_w = 10$ the window size. Lower values of α lead to a faster correlation search, but may also lead to a non-unique determination of the best correlation. Sensitivity testing showed that $\alpha = 0.3$ gives a good balance.

3. The summation is continued with step-wise accumulation of differences between random pairs of pixels. Once $S_{tw,k} > S_*$, the corresponding target window k is not considered anymore. The last remaining target window is assumed to have the highest correlation with the interrogation window. This step is illustrated in Fig. 2.3.

Often a unique best-correlation target window cannot be determined using this algorithm. This can happen when multiple target windows exceed the threshold within one step of the pixel-wise difference and no target window with $S_{tw,k} < S_*$ is left. Thus, an additional method to compare these multiple qualified target windows is needed. Therefore, not only the number of steps until $S_{tw,k} > S_*$ (which is the same for the remaining target windows in this case), but also $S_{tw,k}$ directly is used as a secondary criterion. Applying this correlation search for all possible interrogation windows and for all pairs of subsequent infrared frames in a sequence yields a two-dimensional wind field and its temporal evolution.

Postprocessing

The WEIRD method is not able to estimate a wind field within a moving plume of constant air temperature. When this occurs, WEIRD may calculate erroneously low wind speed estimates due to a lack of temperature inhomogeneities. Therefore, the first step in the postprocessing is to apply a threshold $u_* = +1$ pxl frame^{-1} to the horizontal wind speed. If the estimated horizontal wind speed is below this threshold, the horizontal and vertical wind speed at this pixel is set to NaN.

In order to smooth the resulting two-dimensional wind field, averaging in both the spatial and the temporal domain can be applied. The balance between spatial and temporal averaging depends on the expected properties of the wind field. For example, if the focus is on a high temporal resolution of the estimated wind field, averaging over a domain with larger spatial but smaller temporal extent might be applied. The rate of NaNs within an averaging window (in both spatial and temporal dimension) is tracked and used as a quality control measure.

In a final step, the obtained shift in pxl frame^{-1} is converted into wind speed in m s^{-1}. With the spatial resolution in horizontal direction $\Delta_x = 0.61\,\mathrm{cm}$ and the frame rate of the TIR camera $f = 30\,\mathrm{Hz}$ the conversion factor for horizontal wind speed u is given by $\Delta_x \cdot f = 0.183\ \frac{\mathrm{m \cdot frame}}{\mathrm{s \cdot pxl}}$. Similarly, the conversion factor for vertical wind speed w is $\Delta_z \cdot f = 0.165 \frac{\mathrm{m \cdot frame}}{\mathrm{s \cdot pxl}}$. Be aware that the raw estimated wind speeds for a single pixel and two subsequent frames can only be an integer multiple of the conversion factors. $u_{min} = 0.183\,\mathrm{m\,s^{-1}}$ and $v_{min} = 0.165\,\mathrm{m\,s^{-1}}$ are the minimal detectable wind speeds. A quasi-continuous wind speed estimation is achieved by temporal and spatial averaging of single pixel estimations. The two-dimensional wind vector is assigned to the centre of the corresponding interrogation window. Each vector's location in spatial coordinates (fetch distance and height) is obtained by georeferencing.

2.2.3 Turbulence Measurements

In addition to the screens, a portable short-path ultrasonic anemometer (DA-700 Sonic Corporation, Tokyo, Japan; in the following 'turbulence sensor') was deployed at a height of $h_K = 0.35\,\mathrm{m}$ above the surface. With the measured three-dimensional wind speed components u, v, w and the virtual potential temperature θ the turbulent vertical sensible heat fluxes (SHFs) can be calculated. Data from the turbulence sensor is evaluated for the same 10 min as the infrared sequence. Prior to flux computation erroneous data points are removed and wind speed data is detrended (Aubinet et al., 2012). Furthermore, the three-dimensional wind speed data is double rotated (Kaimal & Finnigan, 1994). Double rotation is preferred over planar fitting due to permanent surface changes induced by snow melt and slight movement of the sensor (Stiperski & Rotach, 2016). After rotation of the ultrasonic data, the u-component points into the mean wind direction and the w-component is perpendicular to the snow surface (Mott et al., 2020). In order to define a suitable Reynolds averaging time separating turbulent from non-turbulent (sub)mesoscale motions, data from the turbulence sensor is evaluated using a Multi-Resolution Flux Decomposition (MRD). MRD is a wavelet transformation preserving Reynolds averaging rules (Vickers & Mahrt, 2003). However, due to the strong temporal heterogeneity of the near-surface atmospheric layer, it is challenging to determine a clear gap scale between turbulent and (sub-)mesoscale motion as described in Vickers and Mahrt, 2003. Combining the MRD with sensitivity analysis suggests a gap scale of $t_{avg} = 30\,\mathrm{s}$. Reynolds averaging to compute fluxes is applied using a moving average with a symmetric window of width t_{avg} around every data point. The obtained SHFs are smoothed by a moving average with a width of 10 s. Additionally, data measured by the turbulence sensor are used as a validation measurement for the wind speed estimations (see 2.3.3).

2.3 Results and Discussion

In the following, an infrared frame is examined qualitatively to obtain a snapshot of the near-surface atmospheric layer. Subsequently, vertical profiles of horizontal and vertical wind speed and temperature for the same situation are analyzed to demonstrate the ability of the developed method. Measurements of wind speed and calculated sensible heat fluxes close to the screen allow the validation of the WEIRD wind field estimations. A video showing the evolution of the near-surface atmosphere in real time is included in Online Resource 2.

2.3.1 Near-Surface Atmospheric Layer Structure Information Gained from an Infrared Frame

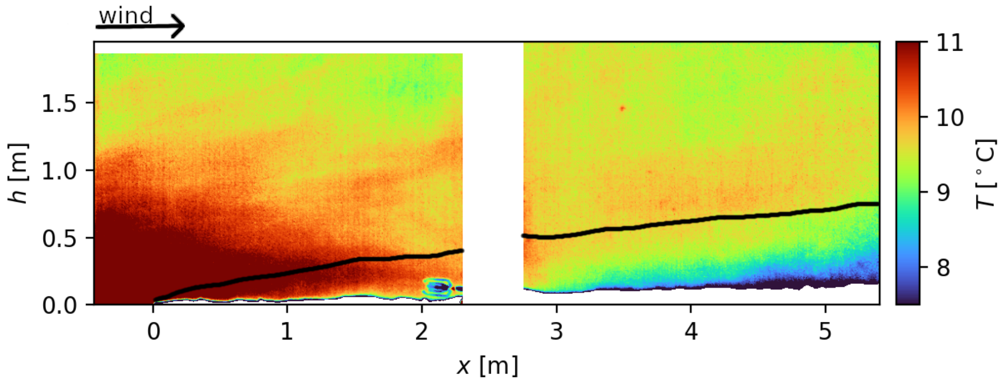

Figure 2.4: A frame out of the sequence for qualitative analysis. The wind advects warm air above bare ground (left/upwind of $x = 0\,\mathrm{m}$) over the snow surface. The black line visualizes the internal boundary layer height approximation in Granger et al., 2006

Qualitative analyses of the data from the TIR camera reveals information about the structure of the near-surface atmospheric layer. Figure 2.4 shows one infrared frame as an excerpt from the infrared sequence with the arrow indicating the prevailing wind direction. The figure shows the wind fetch distance over snow, x, on the x-axis and the height above the bottom of the infrared frame on the y-axis. The snow cover at the screen location is shown in Fig. 2.2a. Furthermore, the UAV image in Fig. 2.1 gives an overview of the snow cover fraction on the site. According to preprocessing step 2, snow covered pixels in Fig. 2.4 are set to NaN and are shown in white. The pixels between the two screens are set to NaN since they do not contain information on the near-surface dynamics. At $x_K = 2\,\mathrm{m}$ the turbulence sensor is deployed at a height of $h_K = 0.35\,\mathrm{m}$ above the snow surface (visible in the foreground of Fig. 2.4, 1.5 m in front of the screens). Data measured with the turbulence sensor is used for validation of the estimated wind field in Sect. 2.3.3. Furthermore, at $x = 3.5\,\mathrm{m}$ and a height of 1.5 m above the bottom of the frame, a small area with a warmer screen temperature is visible. This is an artifact stemming from dirt with a reduced reflectivity and increased heat capacity compared to the screen material. The isolated artifact has just local influences on the recorded temperature field and, subsequently, also on the estimated wind field. However, it demonstrates the importance of a clean screen surface.

The enhanced surface temperature and upward heat fluxes at the bare ground induce plumes of warm air. Figure 2.4 shows the advection of a warm air plume with the mean wind towards the snow covered area. Adjacent to the snow surface a centimetre-deep film of cold air is visible along the whole screen length. There is a strong air temperature gradient within this small film from 0°C at the snow surface to ≈ 10°C above. In order to better visualize the temperature differences above this thin film, the lower limit of the colour bar is chosen to be 7.5°C. Since the temperatures in the lowest centimetre above the snow surface are below this lower limit, the occurring temperature gradient is not resolved in Fig. 2.4 and the temperature appears to be constant within the centimetre adjacent to the snow surface. Above, for $x < 0.5\,\mathrm{m}$ the warm air is mixed down to the snow surface. However, for $x > 0.5\,\mathrm{m}$ a layer of colder air adjacent to the snow surface is visible. With increasing fetch distance, the depth of the cold air layer increases. Simultaneously, the air temperature close to the snow surface decreases with increasing fetch distance. This layer of cold air yields a statically stable temperature stratification close to the ground (temperature profiles are discussed in more detail in Sect. 2.3.2). Above the cold air layer, the static stability changes. The transition in static stability might be referred to as the stable internal boundary layer (IBL) height. IBLs are induced by air moving across a transition of different surface properties (Garratt, 1990). In our case there is a step change in surface temperatures from bare ground (warm) to snow covered areas (0°C). Additionally, there is a step change in surface roughness. In an experimental study Granger et al., 2006 measured the height of the IBL at various fetch distances over snow on an isolated snow patch. The black line in Fig. 2.4 shows their best-fit exponential function as an approximation for the IBL growth for an upwind surface roughness of $z_0 = 0.02\,\mathrm{m} - 0.04\,\mathrm{m}$, which is comparable with the surface roughness of the alpine meadow in our case. In contrast to point-wise temperature measurements as used, for example, in Granger et al., 2006 and Harder et al., 2017, the high spatio-temporal resolution of the temperature field in Fig. 2.4 facilitates more detailed spatial and temporal investigations. Comparing approximated IBL growth with the temperature field on the downwind (right) screen reveals an analogous behaviour especially for the downwind screen. For increasing fetch distances, the height at which a given temperature level is reached grows similarly (e.g., cyan colour $T \approx 9$°C). This resemblance affirms the theoretical approximation. However, a clear IBL height is difficult to determine only from the temperature field. Also note that Fig. 2.4 shows a snapshot of the temperature stratification. For $x < 1.5\,\mathrm{m}$, significant penetration of warm air below the black line down to the snow surface can be observed. Warm air is mixed into the stable IBL at the upwind edge of the snow patch. This entrainment leads to increased melt rates at the upwind edge of the snow patch and is referred to as the leading edge effect. Besides the asset of spatially continuous temperature fields at centimetre resolution, the high temporal resolution of data recorded with the TIR camera allows us to examine the evolution and dynamics of the near-surface atmospheric layer.

2.3.2 Vertical Profiles of Temperature and Estimated Wind Speeds

Figure 2.5 shows vertical profiles at four locations along the screens (1 to 4). The profiles describe the near-surface atmospheric layer dynamics as measured in Fig. 2.4. Complementary to the measured static boundary-layer information shown in Fig. 2.4, the profiles reveal additional high spatial resolution estimations about the dynamics close to the surfaces retrieved by the WEIRD method. Vertical profiles provide information on horizontal wind speed u (left, blue), vertical wind speed w (middle, orange), and screen temperature T (right, red) as a proxy for air temperature. Vertical wind speed w is defined to be positive if air moves upwards away from the surface. The vertical line in the w-profiles denotes $w = 0$. Be aware that, as shown in the bottom infrared frame, the height of the snow surface ($\tilde{h} = 0$) increases for increasing fetches. The vertical lines in the infrared frame indicate the profiles' location on the screens and the corresponding fetch distance. Profile 1 shows the near-surface atmospheric layer over bare ground upwind of the snow patch, while 2 and 3 are taken at fetch distances of $x_2 = 0.25\,\mathrm{m}$ and $x_3 = 1.15\,\mathrm{m}$. The vertical structure of the near-surface atmospheric layer further downwind at a fetch distance of $x_4 = 4.60\,\mathrm{m}$ is indicated by profile 4.

In order to obtain the vertical profiles as shown in Fig. 2.5 the wind field is averaged using a pixel-wise 0.5 s moving average (corresponding to 15 frames) as described in Sect. 2.2.2. The solid lines in the profile plots show the median of all raw profiles in an averaging window with spatial width of $\Delta x = 10\,\mathrm{cm}$ and a temporal span of $\Delta t = 0.25\,\mathrm{s}$. The shaded regions indicate the interquartile range containing 50% of the data from the raw profiles around the median. For a smoother visualization, the profiles are averaged vertically by a moving average with an averaging interval length of 15 cm. Comparing the temperature profiles from the four fetch distances 1 to 4 shows the cooling of the near-surface air as it is transported over the snow surface. This effect is visible up to a height of $\tilde{h} = h_B \approx 100\,\mathrm{cm}$. Vertical temperature profiles measured by Harder et al., 2017 and idealized direct numerical simulations by van der Valk et al., 2021 reveal a similar behaviour. Harder et al., 2017 refer to h_B as the blending height. Furthermore, the temperature profiles 1 to 4 visualize the changing static stability of the near-surface atmospheric layer across the transition from bare ground to snow surface as mentioned in Sect. 2.3.1. The air over bare ground at location 1 is characterized by a statically unstable stratification below a height of $\approx 120\,\mathrm{cm}$ and a near-neutral stratification above. This static instability stems from the bare ground heating up the adjacent air mass

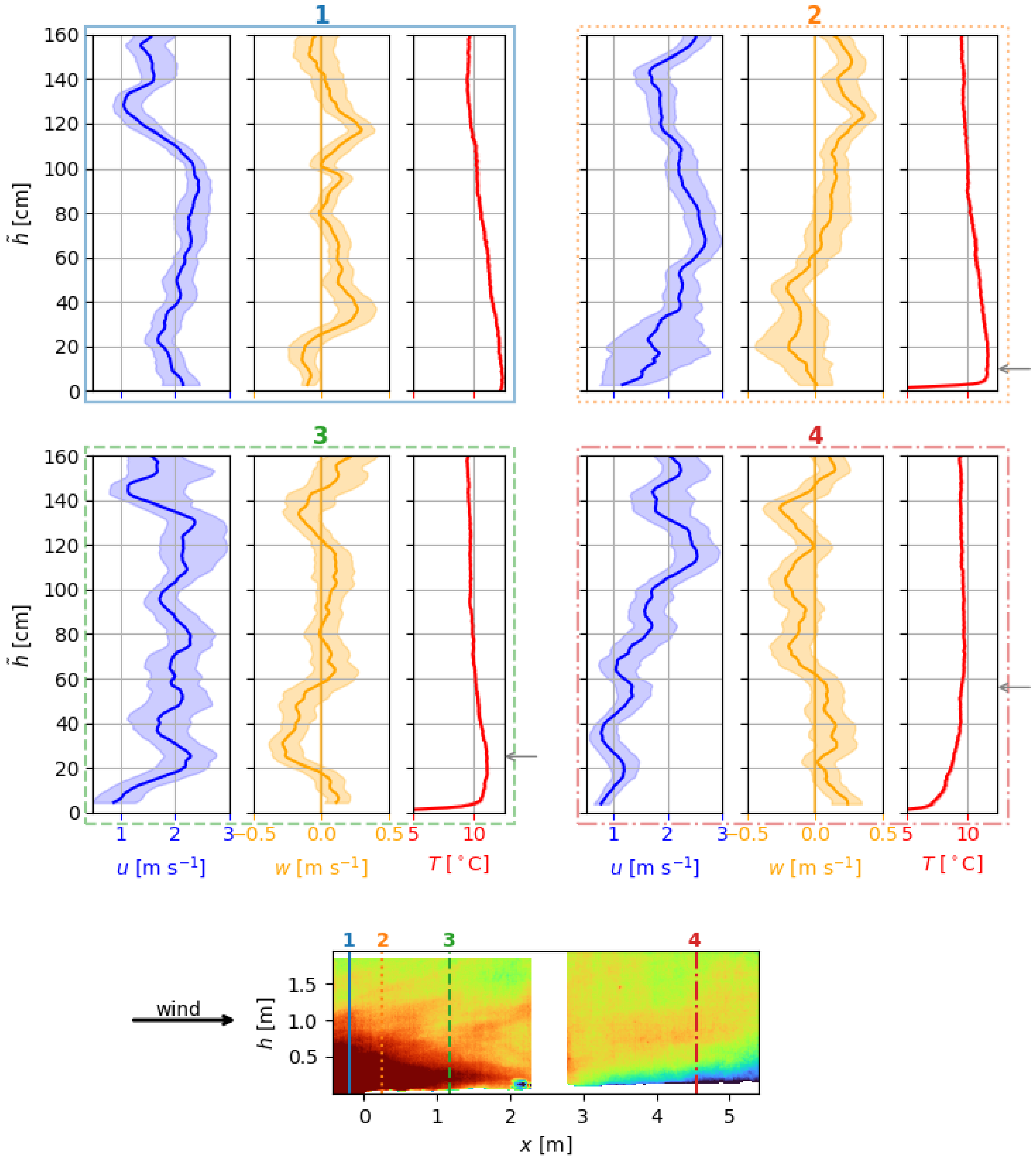

Figure 2.5: Vertical profiles of horizontal wind speed u (blue), vertical wind speed w (orange) and temperature T (red) for 4 different locations along the screen axis averaged over 0.25 s. $\tilde{h}$ is the height above the snow surface for locations 2 – 4 and the height above bare ground for location 1. $w = 0\,\mathrm{m\,s^{-1}}$ is marked by an orange solid vertical line. The four locations are indicated by the vertical lines in the bottom infrared frame and the frames around the corresponding profiles. The height h in the infrared frame refers to the height above the bottom of the frame. The top left profiles describe the situation above the upwind bare ground. From the top right profiles to the bottom right profiles the fetch distance over snow increases. Therein, the approximation for the SIBL height by Granger et al., 2006 is indicated by the grey arrows on the right

causing plumes of warm air. At the leading edge of the snow patch in profiles 2, a very shallow statically stable layer close to the snow surface up to $\tilde{h} \approx 5\,\mathrm{cm}$ is visible. Further downwind the thickness of the statically stable layer close to the snow surface grows. For all locations the IBL height approximated by Granger et al., 2006 is indicated by the grey arrows on the right of the profiles. Comparing the approximation and the height of the statically stable layers at locations 2–4 displays a similar growth. A growing stable layer adjacent to the snow surface is also in accordance with the findings in van der Valk et al., 2021. They show that the strongest downward SHF occur at the upwind edge of the snow patch and the magnitude of the SHF decreases with increasing fetch distance due to a growing stable layer. However, these profiles and the static stratification at the different locations are highly variable in time.

As mentioned above, the entrainment at the leading edge of the snow patch is characterized by mixing warmer air from above down into the IBL at the snow surface. Negative vertical wind speeds for $h < 60\,\mathrm{cm}$ at location 2 and for $20\,\mathrm{cm} < h < 60\,\mathrm{cm}$ at location 3 point to this downward mixing.

At location 2 below 40 cm an enhanced spread in the horizontal and vertical wind speed is visible through the wider interquartile range. This spread points to the extreme spatio-temporal variability of the flow directly at the leading edge of the snow patch. Another aspect is the reduced horizontal wind speeds u in the statically stable layers at locations 3 and 4 in comparison with u aloft. Furthermore, the change in static stability is accompanied by a change from positive w in the statically stable regime to negative w above. These changes might point to a decoupling of the statically stable layer adjacent to the snow surface from the atmosphere above. At location 2 the statically stable layer is too shallow, so a change of vertical wind speed direction cannot be resolved. However, a reduction in u close to the surface can be observed. These findings are complemented by vertical turbulent sensible heat fluxes calculated from the DA-700 short-path ultrasonic (turbulence sensor) data. Figure 2.6 shows a time series of the kinematic SHFs at the same time interval as the infrared sequence. Be aware that the ultrasonic and the infrared data are not precisely synchronized so there might be a time shift in the order of a few seconds. The calculated SHFs vary strongly between up- and downward. This heterogeneity of the fluxes suggests that the turbulence sensor is close to the height of the temporally varying stable IBL, which is in accordance to the approximation in Granger et al., 2006 and to the profiles in Fig. 2.5. Although strongly oscillating and changing signs, the SHFs averaged over the whole sequence are slightly negative (dashed horizontal line), indicating a mean IBL height just above the measurement height of the turbulence sensor.

In order to compare two different characteristic situations, Fig. 2.7 juxtaposes profiles and an infrared frame for a time when the turbulence sensor registered positive SHFs (vertical line t_1 in Fig. 2.4) in the left column and negative SHFs (vertical line t_2 in Fig. 2.4) in the right column. Time t_1 represents the same situation as shown in Fig. 2.4 and Fig. 2.5. However, the profiles are taken at a fetch distance comparable to the fetch distance of the turbulence sensor as indicated by the vertical line in the infrared frame. Comparing the infrared frames

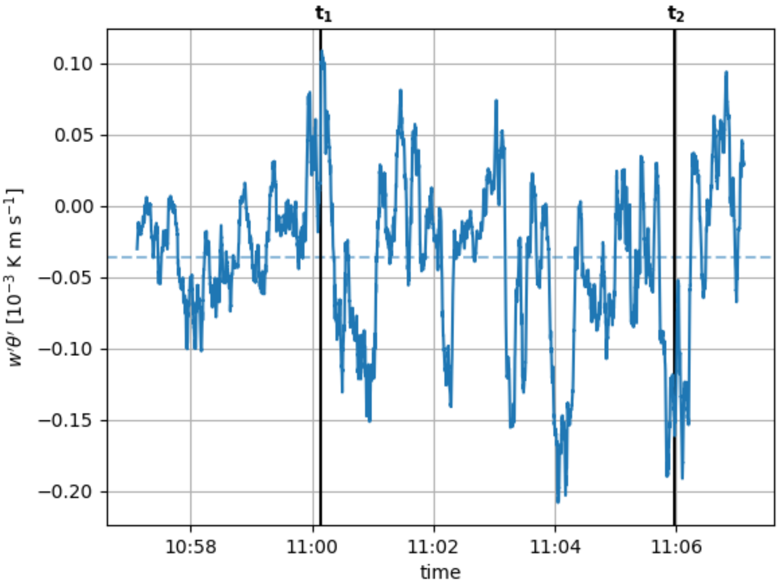

Figure 2.6: Kinematic turbulent vertical sensible heat fluxes ($w'\theta'$, SHFs) measured by the short-path ultrasonic (turbulence sensor) at $h_K = 0.35\,\mathrm{m}$ and a fetch distance $x_K = 2\,\mathrm{m}$ (see bottom right of the upwind screen in Fig. 2.4). Fluctuations of vertical wind speed w' and temperature θ' result from subtracting the 30 s mean from the time series. The plotted flux is averaged using a 10 s moving average. Positive (negative) SHFs refer to the transport of heat away (towards) the surface. The dashed horizontal line represents the average. The vertical line ‘t_1’ (positive SHFs) shows the time where the profiles in Fig. 2.5 and the left column of Fig. 2.7 are taken. The vertical line ‘t_2’ (negative SHFs) indicates the time for the profiles and the frame in the right column of Fig. 2.7

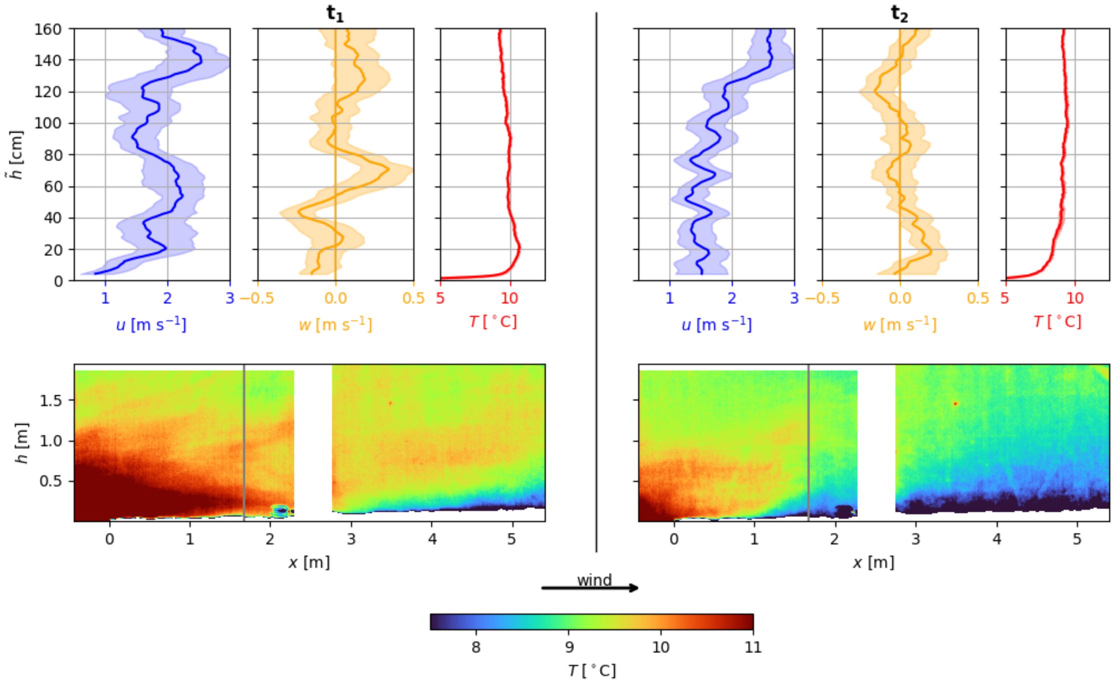

Figure 2.7: Juxtaposition of profiles and infrared frames for positive SHFs (t_1) and negative SHFs (t_2) at the height of the turbulence sensor. See the vertical lines in Fig. 2.6 for the measured fluxes

of time t_1 and t_2 reveals a significantly different atmospheric structure. The atmosphere at time t_1 is characterized by entrainment of warm air at the leading edge of the snow patch and a thin layer of cold air adjacent to the snow surface further downwind. At time t_2, the air is generally colder and the layer of cold air is thicker. At a height of $\tilde{h} = 20\,\mathrm{cm}$ above the snow surface the temperature difference between t_1 and t_2 is 2.2°C. Warm air from over bare ground is not moving downwards towards the snow surface. The thicker and colder layer of air can also be seen in the temperature profiles. While the stable layer at time t_1 is only 20 cm deep, its depth is 100 cm at time t_2. In both cases, the horizontal wind speed in the stable layer is lower than above. At time t_1 and above the warm air plume, a transition from slightly negative vertical wind speed to positive vertical motion can be observed. Within the stable layer at time t_2, updrafts occur close to the surface. Above $\tilde{h} > 0.5\,\mathrm{m}$ the vertical motion is very weak. Combining the infrared frames and the profiles, the findings are in accordance with the SHFs calculated from the turbulence sensor data. For time t_1, positive SHFs indicate a very shallow IBL below the measurement height of the turbulence sensor, whereas for time t_2, negative SHFs support the increased depth of the IBL. The fact that both situations were observed within few minutes demonstrates the high temporal variability of the atmosphere adjacent to the snow surface and therefore the need for ultra-high resolution measurements.

2.3.3 Validation Using Wind Measurements

For the validation of the near-surface wind field estimations from WEIRD, measured wind speeds from the short-path ultrasonic anemometer (turbulence sensor) are used. Data recorded with the turbulence sensor is double rotated into the mean wind speed. To overcome the differences in temporal resolution of the turbulence sensor (20 Hz) and WEIRD estimations (raw data 30 Hz), both are averaged to 10 Hz. Furthermore, ensuring comparability between the two data series, the WEIRD estimations are spatially averaged over a 5 cm × 5 cm window, which matches the path length of the turbulence sensor. The location of the WEIRD averaging window is chosen at the same fetch distance as the profiles in Fig. 2.7 at a height of $h = h_K = 0.35\,\mathrm{m}$. Due to the strong spatio-temporal heterogeneity of near-surface turbulence, a comparison of the wind speed distributions over the 10 min observation period of the infrared sequence is adequate. The distributions are obtained by binning both time series using a bin with of $0.05\,\mathrm{m\,s^{-1}}$. Figure 2.8a shows the comparison for the horizontal wind speed u and Fig. 2.8b for the vertical component w. The comparison of horizontal wind speed histograms in Fig. 2.8a yields a correlation of $\rho_u = 0.96$ and a root-mean-square deviation of $RMSD_u = 0.10$. Both the turbulence sensor data and the WEIRD estimations show a similar distribution with a peak at $\hat{u} \approx 2.2\,\mathrm{m\,s^{-1}}$. However, the maximum of the WEIRD distribution exhibits more scatter. Furthermore, WEIRD estimations of wind speeds $u < 1.5\,\mathrm{m\,s^{-1}}$ occur more often than for the turbulence measurements. A possible explanation might be the decreased performance of the estimation for homogeneous air temperatures or very rapid changes between two subsequent infrared frames leading to difficulties in tracking the pattern. As a consequence, the WEIRD algorithm yields wind speeds scattered around 0 $\mathrm{pxl\,frame^{-1}}$. This scatter is partly filtered by applying the threshold wind speed $u^* = +1\,\mathrm{pxl\,frame^{-1}}$, but the

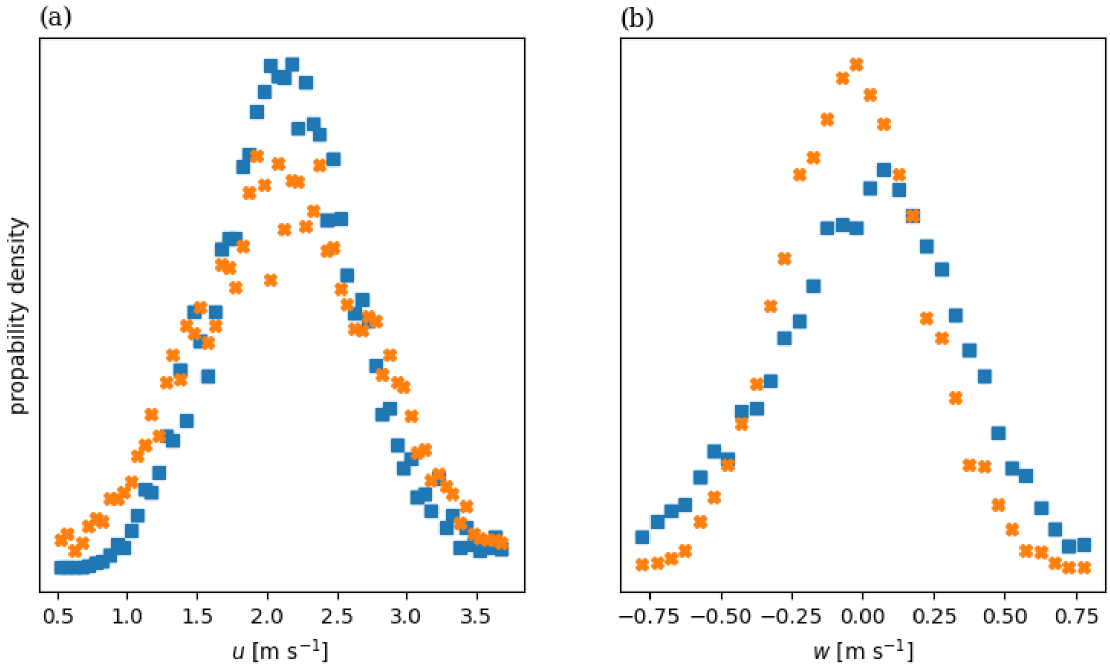

Figure 2.8: Histogram comparison between measured ultrasonic data (turbulence sensor, blue) and estimations using WEIRD (orange) for **a** horizontal and **b** vertical wind speed components

remaining scatter overlaps with valid estimations resulting in an increased estimation of wind speeds $u < 1.5\,\mathrm{m\,s^{-1}}$. Additionally, an increased occurrence of estimations for $u > 2.8\,\mathrm{m\,s^{-1}}$ can be observed. This might stem from the fact that high horizontal wind speeds in the experimental setting of this study mainly coincide with the advection of a warm air plume and, thus, an increase in local air temperature. The resulting clear air temperature pattern allows for accurate tracking and consequently for a valid wind speed estimation. However, if the near-surface flow is characterized by a homogeneous air temperature over time, tracking of pattern fails and results in the above described scatter. The resulting withdrawn estimations leads to a relative overestimation of high (and valid) estimations.

The distributions for the vertical component w of the wind speed shown in Fig. 2.8b exhibit a correlation of $\rho_w = 0.94$ and a root-mean-square deviation of $RMSD_w = 0.23$. Both distributions show a similar shape, but with a shifted peak. This shift might stem from a small tilt of the local snow surface. This tilt would result in a tilt between the direction of horizontal wind speed ($w_{WEIRD} = 0$) on the screen and the u, v-plane of the turbulence sensor. The applied double rotation on the turbulence sensor data implies $\overline{w}_{turbsensor} = 0$, whereas $w_{WEIRD} := 0$ is defined for motions parallel to the bottom of the infrared frame. A counter clockwise rotation of the local wind field in the chosen average window of $\beta = 0.97°$ would yield $\overline{w}_{WEIRD} = 0$ and could therefore explain the shift. However, the minimal shift towards negative vertical motions estimated with WEIRD might also represent the true motion of air, which might have been removed from the turbulence sensor data through double rotation. Similar to the analysis of the horizontal wind speeds, the higher occurrence of WEIRD estimations around $w = 0\,\mathrm{m\,s^{-1}}$ can be explained by scatter around $w = 0\,\mathrm{m\,s^{-1}}$, where the algorithm cannot track a clear air temperature pattern. This scatter, and the resulting increased probability density around $w = 0\,\mathrm{m\,s^{-1}}$, might also be a reason for the relative underestimation of stronger positive and negative vertical motions.

Generally, the wind field estimations using the WEIRD algorithm could be improved by including the propagation of information from the wind field estimation between frame i and frame $i+1$ to the subsequent step. This could help to significantly reduce the computation time due to a restriction of possible target windows to a smaller spatial domain. Additionally, propagation of information between subsequent steps, especially limiting the number of possible target windows, may yield a smoother wind field after the processing step. A smoother wind field in turn offers the possibility to retrieve even higher spatio-temporal resolution data, since less averaging in the post processing is necessary.

2.4 Conclusion and Outlook

We presented a method to gain information about the near-surface atmospheric layer and its dynamics over a strongly heterogeneous surface. Thin synthetic screens are set up vertically across a transition from bare ground to snow aligned with the predominant wind direction. Combined with infrared measurements, the screens serve as a proxy for air temperature. Sequences of infrared frames are recorded by a high-resolution thermal infrared camera at 30 Hz. This data yields ultra-high spatio-temporal resolution information about the near-surface air temperature stratification. Various processes could be observed, such as the entrainment of warm air at the leading edge of a snow patch, or the development of a stable internal boundary layer adjacent to the snow surface.

Using temperature as a marker for moving air parcels, the WEIRD method can track temperature patterns and estimate high resolution horizontal and vertical wind speeds. In combination with the temperature stratification and its temporal change, the wind field from WEIRD provides a new way to quantify the dynamics of the near-surface atmospheric layer on scales of 10^{-2} m and 10^{-1} s.

Near-surface wind speed measurements with a short-path ultrasonic anemometer served as a reference measurement. It was shown that the turbulent sensible heat fluxes calculated from the measured data are in agreement with profiles of horizontal and vertical wind speed and temperature obtained from the screen measurements. Two different characteristic situations with positive and negative sensible heat fluxes and the corresponding infrared frame with vertical profiles of temperature and wind field were juxtaposed. This comparison elucidated the highly variable behaviour of the near-surface atmospheric layer and demonstrated the capability of the presented method to measure the spatio-temporal dynamics. Furthermore, a histogram comparison of horizontal and vertical wind speeds over the 10 min sequence proved the validity of the WEIRD estimations.

The results above display the power of the screen set-up in combination with WEIRD for investigation of the near-surface atmospheric layer dynamics. Such a set-up may also be useful for addressing other research questions, with the requirement of heterogeneous air temperatures at the metre-scale. Other possible applications could include the characterization of different kind of slope flows such as thermal updrafts, drainage, or katabatic flows (Grudzielanek & Cermak, 2015a). Especially measuring properties of low-level jets within deep katabatic flows on glaciers might be an interesting application (Mott et al., 2020; Sauter & Galos, 2016). Furthermore, debris-covered glaciers or perennial ice fields offer a strong surface heterogeneity. The investigation of near-surface atmospheric flow and surface heat exchange processes might, thus, benefit from high spatio-temporal resolution screen measurements (Brock et al., 2010; Mott et al., 2019). Spatially scarce point-based eddy-covariance sensors are not capable of resolving the full near-surface vertical structure. The screen method can fill this gap with spatially continuous measurements.

In ongoing and future research, we will apply the presented methods on multiple recorded sequences in various conditions. We hope to get a broader and deeper insight into the metre- and sub-metre-scale processes present above patchy snow covers, and their consequences for snow melt in late spring. This will be studied with the aim of developing better parameterizations of these processes for use in coarse-scale snow melt models.

Data Availability

Data and documented source code is available at doi:10.16904/envidat.299 .

3 Turbulence in the Strongly Heterogeneous Near-Surface Boundary Layer over Patchy Snow

This chapter corresponds to the postprint version of the article published as

Haugeneder, M., Lehning, M., Stiperski, I., Reynolds, D., Mott, R.: Turbulence in the Strongly Heterogeneous Near-Surface Boundary Layer over Patchy Snow, *Boundary-Layer Meteorology* 190, 7 (2024). https://doi.org/10.1007/s10546-023-00856-4

Abstract

The near-surface boundary layer above patchy snow cover in mountainous terrain is characterized by a highly complex interplay of various flows on multiple scales. In this study, we present data from a comprehensive field campaign that cover a period of 21 days of the ablation season in an alpine valley, from continuous snow cover until complete melt out. We recorded near-surface eddy covariance data at different heights and investigated spectral decompositions. The topographic setting led to the categorisation of flows into up and down valley flows, with a down valley Föhn event in the middle of the observation period. Our findings reveal that the snow cover fraction is a major driver for the structure and dynamics of the atmospheric layer adjacent to the snow surface. With bare ground emerging, stable internal boundary layers (SIBL) developed over the snow. As the snow coverage decreased, the depth of the SIBL decreased below 1 m and spectra of air temperature variance showed a transition towards turbulent time scales, which were caused by the intermittent advection of shallow plumes of warm air over the snow surface. The intermittent advection could also be observed visually with high spatio-temporal resolution measurements using a thermal infrared camera. While the shallow advection only affected the lowest measurement level at 0.3 m, the measurements above at 1 m, 2 m, and 3 m indicate that the distribution of eddy size and, thus, the turbulence structure, did not distinctly change with height.

3.1 Introduction

The exchange of energy, mass, and momentum between the atmosphere and the underlying surface is driven by processes in the Atmospheric Boundary Layer (ABL). Stull, 1988 defines it as "that part of the troposphere that is directly influenced by the presence of the earth's surface and responds to surface forcing with a timescale of about an hour or less". Due to its significance for understanding, modelling, and predicting weather, it has been the focus of many studies. Due to radiative cooling in clear sky conditions or advection of warm air over a cold surface, stable boundary layers develop. This is especially the case in the presence of snow covering the surface (Schlögl et al., 2017a). The stably stratified layer attenuates or even shuts down any turbulent motion. Compared to convective boundary layers, their stable counterparts are less well understood. Interactions with larger, submeso scale motions lead to non-stationary intermittent turbulence (Mahrt, 2014).

Similar to the ABL, Lehner and Rotach, 2018 define the Mountain Boundary Layer (MBL) over complex topography. The MBL influences the flow on various scales ranging from $\mathscr{O}(10^2\,\mathrm{m})$ to $\mathscr{O}(10^6\,\mathrm{m})$ (Serafin et al., 2018). On a mountain-range scale, forced dynamic lifting or acceleration of atmospheric flow induces phenomena such as Föhn (Drobinski et al., 2007; Jansing et al., 2022). On smaller scales, valleys and ridges also interact with the flow by deflecting the flow direction to follow the valley axis. Flows above the terrain with a cross valley direction accordingly change direction closer to the surface (Jackson et al., 2013; Whiteman & Doran, 1993; Zardi & Whiteman, 2013). Furthermore, differential heating leads to the development of valley wind systems. During the day, enhanced warming of the valley atmosphere leads to a local low pressure and up valley flow. In the evening, pronounced cooling reverses the valley flow to down valley (Schmidli, 2013). The same effects occur on a slope scale. Terrain features like slope angle and exposition induce local differences in the surface energy budget, influencing the temperature of the adjacent air. Slope winds compensate for the resulting buoyancy-driven pressure heterogeneities. With incoming radiation, slopes heat up, and up slope (anabatic) winds develop. Cooling near-surface air by the surface causes downward slope (katabatic) winds. Compared to valley flows, slope flows react much quicker to changes in the surface energy balance as shading of the incoming radiation by clouds or terrain can happen quickly (Nadeau et al., 2013; Zardi & Whiteman, 2013). Interaction between flows at all scales and superposition with the synoptic flow adds complexity to the MBL (Zängl, 2009).

Not only the topography but also the surface heterogeneity leaves its fingerprint in the atmospheric flow. Surfaces of alternating aerodynamic roughness length, surface temperature, and surface moisture lead to spatially highly heterogeneous turbulent heat and momentum fluxes (Goger et al., 2022; Rotach et al., 2015).

In spring, bare patches arise in the mountainous snow cover. The lower surface albedo leads to an increased energy input by radiation and, thus, to ground heating. However, the melting snow pack's surface temperature is limited to 0°C, resulting in a substantial surface temperature heterogeneity. This heterogeneity of the surface influences the near-surface atmosphere. Regions of opposite atmospheric stability and sensible heat flux direction develop within just a few meters of lateral distance (Mott et al., 2018).

The advection of warm air leads to the development of a stable internal boundary layer (SIBL) adjacent to the snow surface (Garratt, 1990). The SIBL height is characterized by the transition from downward sensible heat fluxes within the SIBL to upward heat fluxes above (Mott et al., 2017). The strong near-surface stability dampens heat fluxes and thus has an impact on the energy balance of snow. During patchy snow cover, depending on the meteorological conditions, heat fluxes contribute up to 30% to the available energy for melt (Harder et al., 2017; Pohl et al., 2006; Schlögl et al., 2018b, 2018a). Above bare ground, however, the high surface temperatures induce the development of heated, convective near-surface atmospheric layers. Additionally, Harder et al., 2017 illustrated the importance of latent heat advection, especially with the presence of upwind ponded water. Despite the impact on snow cover modelling, only a few experimental studies of the interaction between the near-surface atmosphere and melting snow cover have been carried out in the past years (for example Fujita et al., 2010; Granger et al., 2006; Harder et al., 2017; Mott et al., 2013, 2017; Schlögl et al., 2018a; van der Valk et al., 2022).

To address the existing lack of extensive experimental data, we conducted a comprehensive field campaign in an alpine catchment during patchy snow cover. The experiment has been designed to be able to quantify the processes and relevant time- and length scales. Using various measurement techniques, we aim to answer the following questions:

- How do buoyancy fluxes, turbulence kinetic energy, temperature variance, and their time scales change with a decreasing snow cover fraction throughout the ablation period?

- How do the fluxes and their time scales change when approaching the partly snow covered surface? How do they differ at different measurement levels (0.3 m, 1 m, 2 m, and 3 m)?

The paper is structured as follows: The second section gives an overview of the experimental set-up and the applied methods for processing the data. Sect. 3.3 describes the meteorological conditions and prevailing flow regimes. After describing how we separated turbulent from non turbulent motions in Sect. 3.4, Sect. 3.5 analyzes the development of the near-surface boundary layer during the observation period. Additionally, we elaborate on the vertical structure of turbulence close to the surface. Finally, conclusions are drawn in Sect. 3.6.

3.2 Methods

3.2.1 Study Site and Data Collection

We collected experimental data at the flat Dürrboden in the upper Dischma valley (Fig. 3.1) close to Davos (Switzerland) from 21 May 2021 to 11 June 2021. The Dischma valley is an alpine valley with its valley axis in southeast–northwest direction. It has been comprehensively investigated for multiple observational and modelling studies (Bavay et al., 2009; Brauchli et al., 2017; Carletti et al., 2022; Gerber et al., 2019; Lehning et al., 2006; Reynolds et al., 2023; Schlögl et al., 2018b, 2018a; Wever et al., 2017). Slopes enclose the valley floor with an elevation difference of around 1000 m. Piz Grialetsch and Scalettahorn form the boundary of the catchment area towards the south–southeast. These peaks have long-lasting snow fields and a small glacier on their northern slopes, visible on the bottom right of the map in Fig. 3.1. On the ridge, at an elevation of 3035 m a.s.l. an automatic weather station records meteorological data. The data are used to classify Föhn periods in Sect. 3.3.2. At an altitude of 2010 m a.s.l., the flat area of Dürrboden is covered by alpine meadow and accessible by a

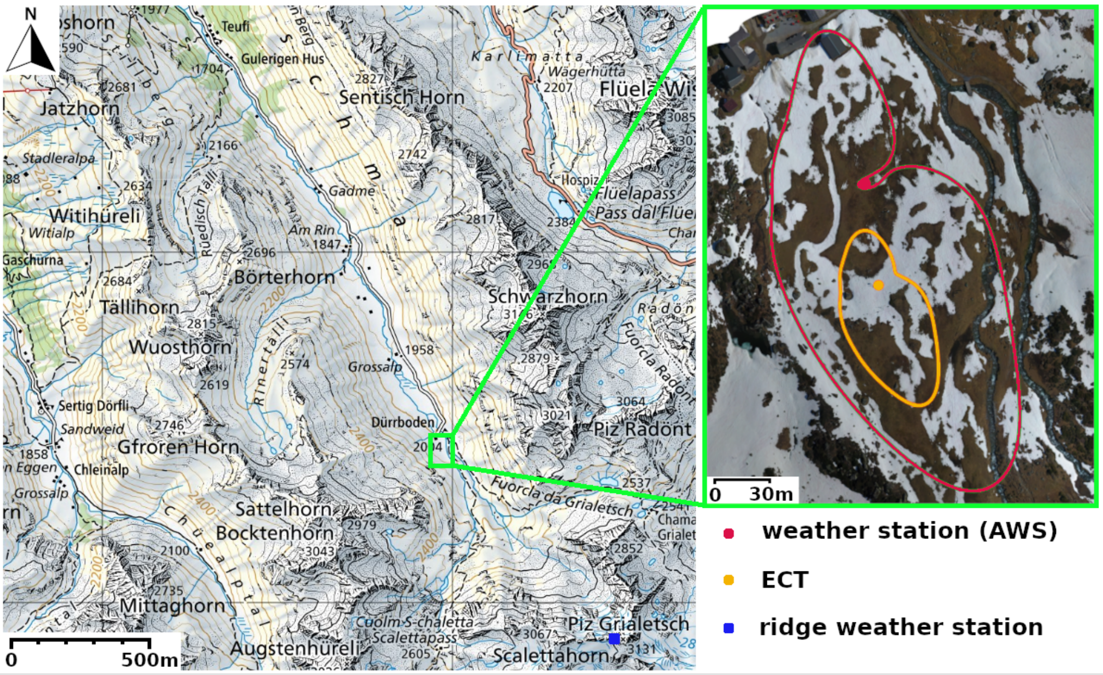
N
Jatzhorn
Witihüreli
Sentisch Horn
Flüela Wis
Börterhorn
Tällihorn
Wuosthorn
Schwarzhorn
Grossalp
Dürrboden
Piz Radönt
Gfroren Horn
Sattelhorn
Bocktenhorn
Mittaghorn
Augstenhüreli
Scalettapass
Piz Grialetsch
Scalettahorn
Fuorcla da Grialetsch
0 500m
0 30m
● weather station (AWS)
● ECT
■ ridge weather station

Figure 3.1: Topographic map of Dischma valley end close to Davos (Switzerland). In the green box, an orthophoto (3 June 2021) obtained from an Uncrewed Aerial Vehicle shows the flat study site with the measurement stations including an automatic weather station (AWS). Additionally, the 70% climatological flux footprints according to (Kljun et al., 2015) are shown for a 5 m measurement at the AWS (red line) and a 2 m measurement at the eddy covariance measurement tower (ECT) (orange line). Furthermore, a blue dot indicates the location of an automatic weather station at the ridge close to Piz Grialetsch.

maintained road. The orthophoto (Fig. 3.1 right) shows the Dürrboden area on 3 June 2021.

The location of an automatic weather station (AWS) and a movable eddy covariance measurement tower (ECT) is also marked on the orthophoto in Fig. 3.1. Figure 3.2 shows a picture of the two measurement stations. The sensors used for the analysis in the present study are highlighted and their specifications are further described in Table 3.1. All sensors on the ECT were sampled at 20 Hz using a single data logger.

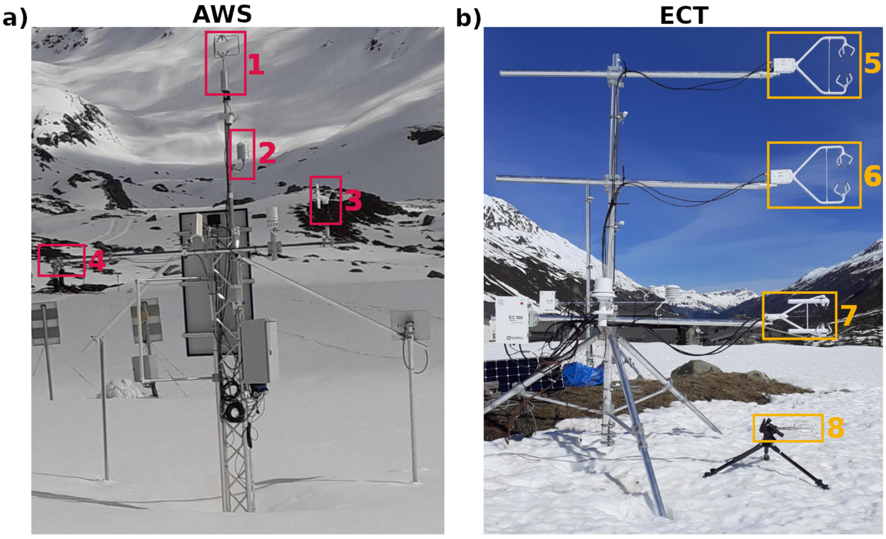

Figure 3.2: **a** The automatic weather station (AWS). **b** The eddy covariance measurement tower (ECT) and a short-path ultrasonic anemometer. Instruments used for the present study are highlighted with the corresponding descriptions and specifications in Table 3.1. The pictures were taken on 20 May 2021 (AWS) and 28 May 2021 (ECT).

The AWS was installed at a fixed position throughout the whole campaign. At the beginning of the observation period, the surface below was still snow covered. However, a small bare patch below the station emerged on 22 May. It gradually expanded to a radius of ≈ 2 m on 30 May. Afterwards, the bare patch quickly grew (see orthophoto on 3 June in Fig. 3.1).

Additionally, Uncrewed Aerial Vehicle (UAV) flights were conducted on multiple days to obtain orthorectified areal overview photos. Figure 3.3 shows captured orthophotos revealing the snow cover distribution throughout the campaign. The AWS and the ECT positions are indicated by circles. Applying a pixel colour value threshold on the blue band of the orthophotos yields information on the snow cover fraction (Eker et al., 2019). Snow covered pixels exceed the threshold, while bare pixels stay below.

We repositioned the ECT once according to the snow distribution. We expect that for up valley flows, the sensors at the ECT characterized the near-surface atmospheric layer above the upwind edge of a snow patch. Until 31 May, when more bare patches arose, both were positioned close to the AWS. At noon of 31 May, we relocated the ECT to a second position

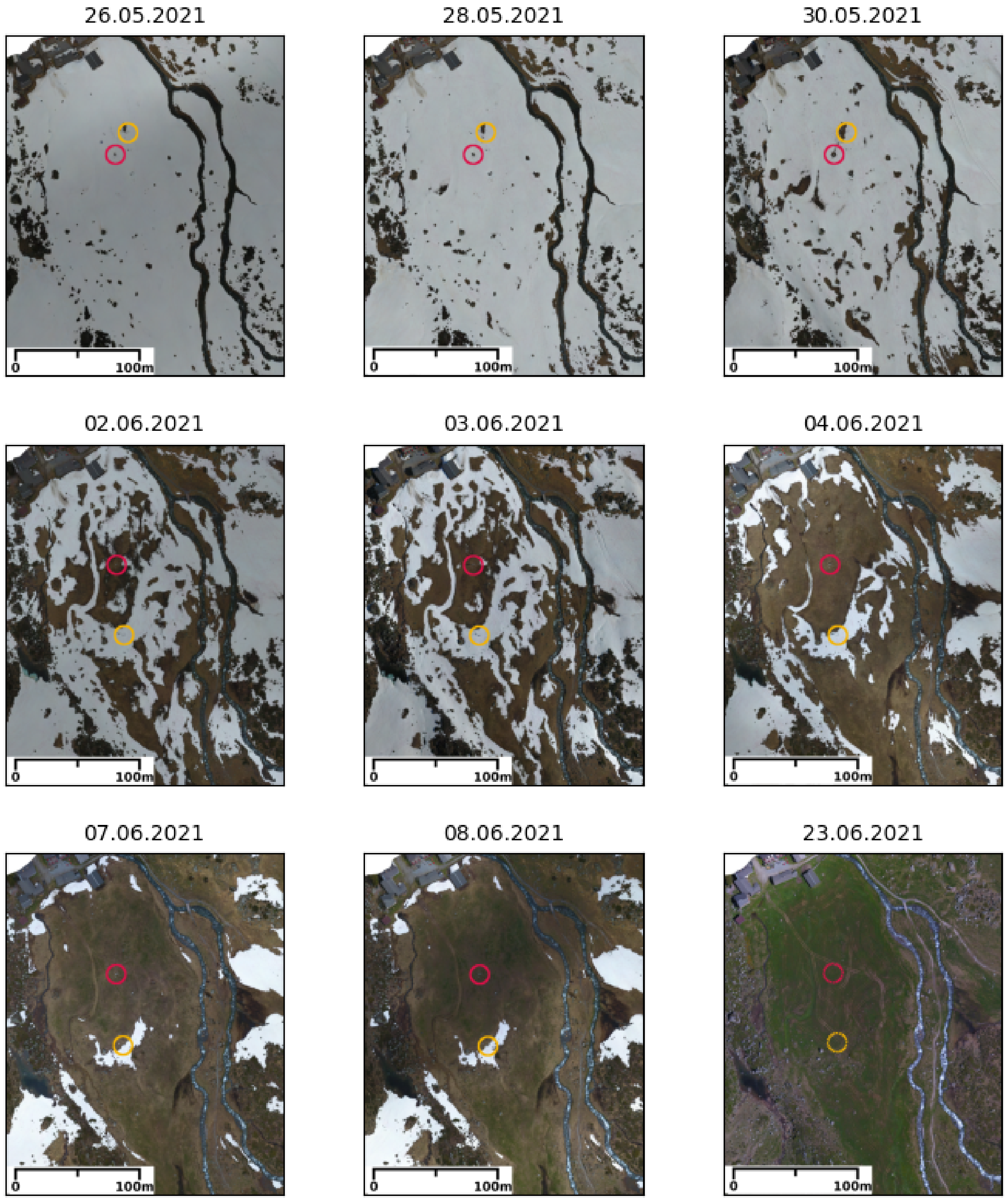
26.05.2021
28.05.2021
30.05.2021
02.06.2021
03.06.2021
04.06.2021
07.06.2021
08.06.2021
23.06.2021
0
100m

Figure 3.3: Orthophotos captured by the UAV during the observation period. The red circles mark the position of the AWS, the orange circles the position of the ECT. The last image captured on 23 May 2021 is a snow off reference. The stations were already dismantled. Therefore, the last position of the stations is indicated by the dotted circles.

Table 3.1: Sensors used for the present study. See Fig. 3.2 for a picture and the numbering of the sensors.

Nr.	Height [m]	Model	Description
1	5.0	81000 Ultrasonic Anemometer, YOUNG[1]	EC sensor
2	4.0	CS215-L Campbell Scientific[2]	T_{air} and RH sensor
3	3.5	05103 Wind Monitor, YOUNG[1]	propeller anemometer
4	3.1	SN-500-SS, Apogee Instruments[3]	Net radiometer
5	3	CSAT3B, Campbell Scientific[2]	EC sensor
6	2	CSAT3B, Campbell Scientific[2]	EC sensor
7	1	IRGASON, Campbell Scientific[2]	EC sensor and gas analyser
8	0.3	DA-700, Sonic Corporation[4]	short-path EC sensor

[1] YOUNG, Traverse City, Michigan, USA; [2] Campbell Scientific, Logan, Utah, USA;
[3] Apogee Instruments, Logan, Utah, USA; [4] Sonic Corporation, Tokyo, Japan

approximately 80 m south-south-west, where it remained during the rest of the observation period. We relocated the ECT such, that the distance to the upwind edge of the snow patch before and after relocation was the same. Thus, we expect no influence on the continuity of the data. The two positions of the ECT throughout the campaign are indicated by the orange circles in Fig. 3.3. As the snow cover decreased, the transition line from bare ground to snow approached the ECT. However, the ECT remained above the snow until the end of the observation period.

In Fig. 3.1, we present the 70% climatological flux footprints for the final position of the ECT from 31 May to 11 June. The climatological flux footprints aggregate flux footprints during the entire observation period. We use the parameterization described in Kljun et al., 2015. The parameterization results from a Lagrangian footprint model using readily available variables like surface roughness, mean wind speed, shear velocity, and lateral wind speed fluctuations. The orange footprint represents the 3 m measurement at the ECT, while the green footprint represents the 5 m measurement at the AWS. The analysis shows that southerly (down valley) winds dominate the footprints with a smaller contribution from northerly (up valley) winds. For the 5 m measurement, the 70% footprint covers the entire Dürrboden area. The buildings 120 m north of the setup do not substantially disturb the measurements.

From 1 June 0600 LT (LT = local time = UTC + 2 h) to 2 June 1200 LT a portable short-path EC sensor ("8" in Fig. 3.2 and Table 3.1) was installed at the ECT at a height of 0.3 m above the snow surface.

In addition to the eddy covariance measurement, we deployed the setup described in Haugeneder et al., 2023. Following their methodology, we recorded sequences of thermal infrared frames of thin synthetic screens vertically deployed across the transition from bare ground to snow. The screens cover a horizontal distance of 6 m and a height of 2 m. Their surface temperature serves as a proxy for local air temperature. The measurements offer a spatio-temporal resolution of 0.6 cm and 30 Hz. The data are presented in Figs. 3.8 and 3.9. The shown excerpts stem from a sequence recorded on 31 May 1435LT-1455LT in direct vicinity of the ECT position indicated in Fig. 3.1.

3.2.2 EC Data Preparation

The presence of a heterogeneous surface and steep slopes requires special attention in the EC data treatment (Stiperski & Rotach, 2016). In the following, we describe the post processing steps to remove artefacts and obtain reliable fluxes. Initially, the diagnostic flags set by the instrument were checked, and suspicious records were flagged as Not-a-Number (NaN). Subsequently, the data were compared to physical limits to remove non-physical values. Additionally, a despiking algorithm, as described by Sigmund et al., 2022, was applied, which considers that spikes often coincide in multiple variables. Next, intervals of NaNs shorter than one second were filled using linear interpolation, reducing the gaps and simplifying posterior flux calculations. Finally, the data were double rotated in 30 min blocks. The double rotation ensures that the u axis is aligned with the mean horizontal wind direction and the mean vertical wind speed vanishes ($\overline{w} = 0$).

To perform a general quality analysis of the EC data, we checked Fourier spectra for the presence of an inertial subrange. Within the inertial subrange, the $\log(f)$–$\log(fS(f))$ diagram exhibits a $-\frac{2}{3}$ slope (Kolmogorov, 1941; Stull, 1988). The Fourier spectra in Online Resource 1 for all sensors indicate the existence of the inertial subrange with its characteristic slope suggesting a good quality of the measured data on all EC sensors.

To calculate fluxes, the timescale separating turbulence from submeso scale motions required for Reynolds averaging was determined using a Multi-Resolution Flux Decomposition (see Sect. 3.2.3) (Howell & Mahrt, 1997; Vickers & Mahrt, 2003). The results are presented in Sect. 3.4. For a qualitative description of the difference between turbulence and submeso scale motions see Sect. 4 and 5 and Fig. 2 in Mahrt, 2014. $\overline{w'T_s'}$ denotes the buoyancy flux with a downward flux defined as negative (stable conditions). T_s is the virtual temperature measured by the sonic anemometers containing effects of moisture (Schotanus et al., 1983). From the diagonal entries of the Reynolds stress tensor, turbulence kinetic energy e is calculated as

$$e = \frac{1}{2}\left(\overline{u'u'} + \overline{v'v'} + \overline{w'w'}\right). \tag{3.1}$$

In order to explain measured air temperature variances in the strongly stable near-surface layer, we utilize the concept of turbulence potential energy. According to Zilitinkevich et al., 2007, in stable boundary layers, the total turbulence energy is comprised of e, and the turbulence potential energy

$$E_p = \frac{1}{2}\left(\frac{\beta}{N}\right)^2 \left\langle \Theta^2 \right\rangle \propto \overline{(T_s')^2}, \tag{3.2}$$

with the buoyancy parameter $\beta = \frac{g}{T_0}$ (gravitational acceleration g and a reference temperature T_0). N denotes the Brunt–Väisälä frequency $N = \left(\beta \frac{\partial \Theta}{\partial z}\right)^{\frac{1}{2}}$, Θ the virtual potential temperature fluctuations, and z the height above the surface. In unstable conditions, the Brunt–Väisälä frequency becomes imaginary. Therefore, E_p is only defined in stable conditions. In the present study, the proportionality of E_p with the variance of the measured sonic temperature is important.

3.2.3 Multi-Resolution Flux Decomposition

The Multi-Resolution Flux Decomposition (MRD) is a powerful tool to gain spectral information from a time series data set (Howell & Mahrt, 1997). MRD is a wavelet decomposition into dyadic scales with a constant basis function (Vickers & Mahrt, 2003). The decomposition offers scale-wise information on fluxes while preserving Reynolds averaging rules. Unlike the Fourier Decomposition, it is not based on the assumption of infinite temporal periodicity of the data. This periodicity includes both turbulent events and the temporal separation between events. Turbulence in general does not fulfil the periodicity assumption. Therefore, MRD is preferred over Fourier decomposition. According to Vickers and Mahrt, 2003 the MRD cospectrum of two turbulent time series u_i and $\phi_i,\ i = 1,2,..,2^M$ at scale $m+1,\ m = 0,1,..,M-1$ is given by

$$C_{u\phi}(m+1) = \frac{1}{2^{M-m}} \sum_{n=1}^{2^{M-m}} \overline{u}_n(m)\overline{\phi}_n(m) \tag{3.3}$$

with $\overline{u}_n(m)$ (similar for $\overline{\phi}_n(m)$) the mean of all 2^m non-overlapping segments of length 2^{M-m}

$$\overline{u}_n(m) = \frac{1}{2^m} \sum_{i=(n-1)2^m+1}^{n2^m} ur_i(m),\ n = 1,...,2^{M-m}. \tag{3.4}$$

$ur_i(m)$ is the residual time series where segment averages of width $> 2^m$ have been subtracted. An MRD is obtained recursively starting with the average over the complete time series ($m = M$; no $C_{u\phi}(M)$ is calculated). Subsequently, the average is removed from the time series to obtain $ur_i(M-1)$ and (3.3) and (3.4) are evaluated for $m = M-1$. At last, $C_{u\phi}(0)$ is determined by the fluctuations of single data points about 2-point means. For a visualisation see Fig. 1 in Vickers and Mahrt, 2003. The flux calculated using a specific Reynolds averaging time (2^m data points) can be obtained by summing the spectral contributions for scales $\leq m$.

Applying MRDs for multiple windows shifted by Δi data points (corresponding to a time shift of Δt) a time series of arbitrary length l, i.e. $l \neq 2^M$, can be decomposed. Furthermore, it allows for illustrating the change of the MRD with time, which enables observing changes in the turbulence structure from hours to days. Especially in the presented case of a highly heterogeneous near-surface atmospheric layer, much information can be gained from the temporal evolution of the cospectra.

The orthogonal decomposition (non-overlapping averaging segments) is sensitive to a temporal shift of the data. Especially for near-surface turbulence above a strongly heterogeneous surface, the cospectrum at a given scale depends on the position of events at that scale relative to the averaging segments boundaries (Howell & Mahrt, 1997). To overcome this drawback, the non-orthogonal MRD uses overlapping averaging segments. In this study consecutive segments are shifted by 1 record yielding maximum overlap. Equations (3.3) and (3.4) are modified to

$$C_{u\phi}(m+1) = \frac{1}{2^M - 2^m + 1} \sum_{n=0}^{2^M - 2^m} \overline{u}_n(m)\overline{\phi}_n(m), \; n = 1, ..., 2^M - 2^m + 1 \tag{3.5}$$

with

$$\overline{u}_n(m) = \frac{1}{2^m} \sum_{i=n}^{n+2^m-1} ur_i(m). \tag{3.6}$$

The non-orthogonal MRD is normalized using calculated turbulent fluxes to ensure comparability with the orthogonal MRD.

Another advantage of the non-orthogonal MRD is the possibility to extend the decomposition to more time scales m. Howell and Mahrt, 1997 suggest setting $m = \log_2(2k)$, $k = 1, 2, 3, ..., 2^{M-1}$. However, that includes many steps and, thus, the computational effort is tremendous. Therefore, we adapted the non-orthogonal MRD to be used with multiple independent series for m. Instead of only setting $m = m_1 = 1, 2, ..., 2^M$, a non-orthogonal MRD can also be evaluated for $m_2 = 3m_1 = 3, 6, ..., 3 \cdot 2^{M-2}$, $m_3 = 5m_1 = 5, 10, ..., 5 \cdot 2^{M-3}$, and so on. The evaluation is truncated when the desired total number of time scales is reached.

Figure 3.4a shows a comparison of an orthogonal (blue) and non-orthogonal moving window (orange, dashed) MRD for a 12 h period over snow. The MRD window width is $M = 15$ corresponding to ≈ 27 min. Decomposed turbulent variables are the vertical wind speed w and the sonic temperature T_s yielding the vertical sonic temperature flux $\overline{w'T_s'}$. The shaded areas indicate the region between the 25% and the 75% quartiles. Both curves show a maximum negative flux contribution for time scales between 5 s and 10 s. At short time scales non-orthogonal MRD shows a slightly smaller flux contribution than orthogonal MRD. However, for larger time scales both MRDs agree well. Generally, a deviation between the two methods is expected due to a difference in phase and number of the averaging segments. In Fig. 3.4b, the non-orthogonal moving window MRD with 15 discrete time scales (orange curve in Fig. 3.4a) is compared to a non-orthogonal MRD using 106 time scales. It becomes obvious that an extension to more time scales does not change the shape of the cospectrum. However, it adds more detailed information on the cospectrum between the 15 discrete time scales. In summary, normalized non-orthogonal MRDs, as employed in this study, can be interpreted equivalent to "traditional" orthogonal MRDs.

We show the decomposed scales in units of time (i.e. time scale τ on the x-axis in Fig. 3.6). Employing Taylor's hypothesis (Taylor, 1938) and using the mean wind speed during the individual periods, τ can be converted to spatial scales.

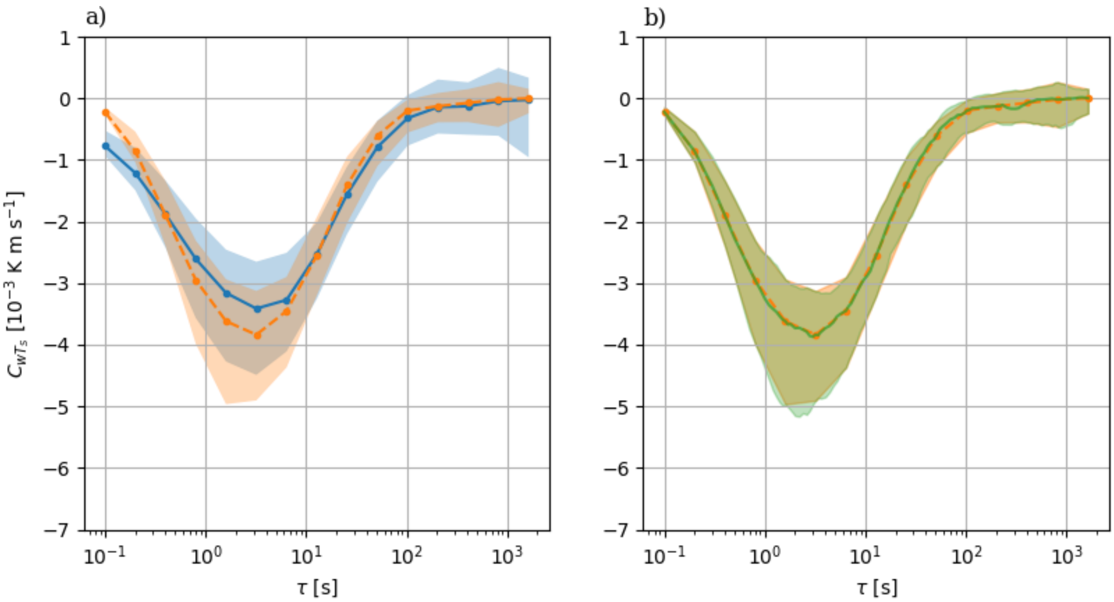

Figure 3.4: **a** Comparison of an orthogonal moving window MRD (blue) and a non-orthogonal moving window MRD (orange, dashed) for a 12 h period over snow. On the x-axis, the time scale, τ, is shown, while the y-axis indicates the cospectrum C_{wT_s}. The shaded region is defined by the 25% and the 75% quartiles. **b** The non-orthogonal moving window MRD from a) (orange, 15 discrete values for τ) compared to a non-orthogonal moving window MRD using 106 discrete values for τ for the decomposition (green).

The MRDs shown in this study are created using Julia (Bezanson et al., 2017) and Matplotlib (Hunter, 2007). We use scientific, perceptually uniform colour maps from Hunter, 2007 and Crameri et al., 2020.

3.3 Meteorological Conditions

3.3.1 Weather Pattern

In Fig. 3.5, we present the data recorded by the AWS during the campaign. We observed an increasing air temperature trend during the 21 day observation period. High relative humidity at the beginning and towards the end of the period indicates cloudy and humid conditions. There were two major snow falls on 22 May and 23 May, each yielding ≈ 10 cm of new snow. Due to warm and sunny weather, the new snow melted within 12 h after deposition. After 5 June, there were a few minor rainfall events < 1 h with minor precipitation amounts. During the melt phase, especially on 28 May and from 30 May to 1 June, the conditions were characterized by clear skies and maximum incoming shortwave radiation. On 27 and 29 May, developing cumuli attenuated the incoming shortwave radiation already before noon. The attenuation is visible in Fig. 3.5c. Until 24 May we measured wind gusts up to 18 $\mathrm{m\,s^{-1}}$. After that, only few

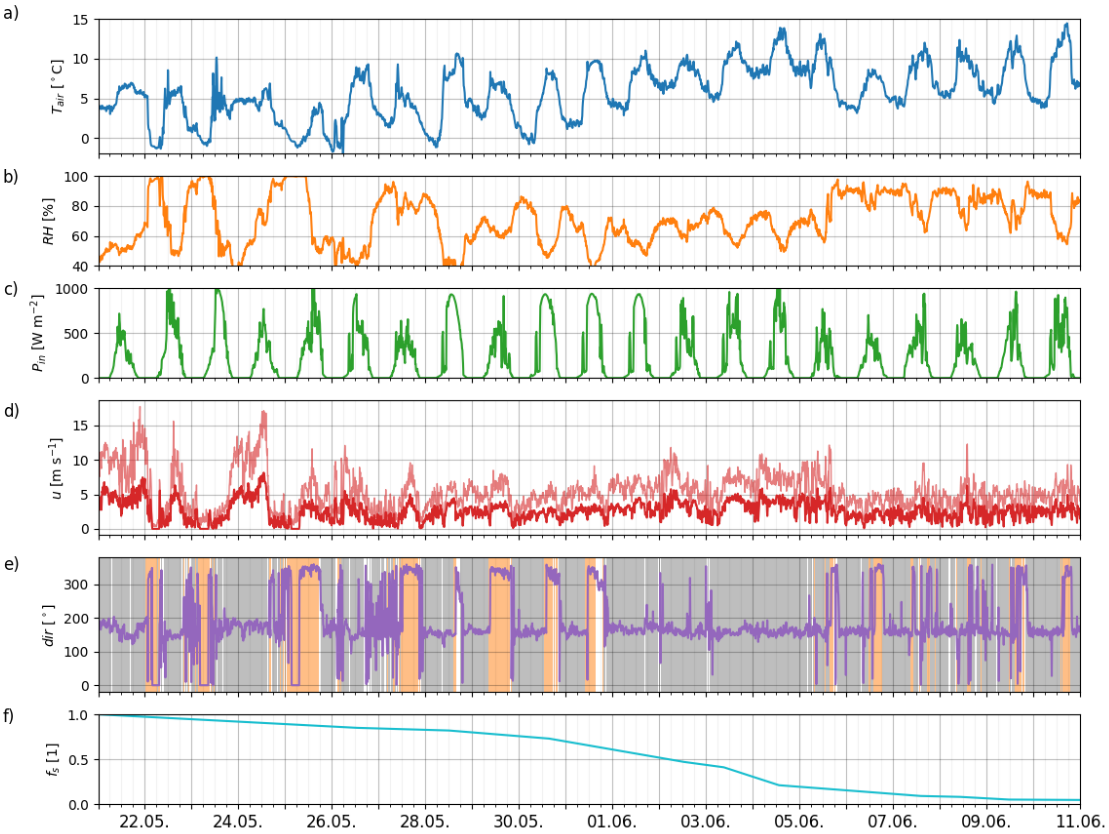

Figure 3.5: The plot displays the following variables from top to bottom: **a** air temperature, T_{air}, and **b** relative humidity RH at a height of 4 m above the surface, **c** incoming shortwave radiation P_{in}, **d** wind speed measured by a propeller anemometer at a height of 3.5 m above the surface u (red: 10 min mean, light red: 10 min gusts). The background colours in the wind direction panel **e** denote the corresponding wind direction class as introduced in Sect. 3.3.2. **a** to **e** shows data recorded by the AWS. The bottom panel **f** shows the snow cover fraction f_s evaluated from the UAV images.

wind gusts exceeded 10 $\mathrm{m\,s^{-1}}$ and the mean wind speed was largely below 5 $\mathrm{m\,s^{-1}}$. In the wind direction plot, the two main wind directions appear: Up valley flow (NNW) and down valley flow (SSE). They are marked according to the corresponding wind direction class as explained in Sect. 3.3.2. The bottom panel shows the snow cover fraction f_s for the Dürrboden area. The strongest decrease of snow cover fraction occurred between 28 May and 5 June, when air temperatures constantly rose and the weather was mostly clear. Furthermore, during that period the weather was influenced by interrupted Föhn (see Sect. 3.3.2).

3.3.2 Flow Regimes

Due to the topography of the straight Dischma valley, two main flow directions can be distinguished. The dominance of those two flow directions is visible in the wind direction panel of Fig. 3.5 and the climatological flux footprints in Fig 3.1. During sunny days around noon, in the absence of counteracting synoptic forcing, a thermally driven up valley flow developed (Farina & Zardi, 2023; Urfer-Henneberger, 1970; Whiteman & Doran, 1993; Zardi & Whiteman, 2013). Its onset, strength, and duration depend on the atmospheric conditions and the interplay with other flows. When the surface heating decreased in the evenings, the flow direction switched back to down valley around 1900 LT at the latest. The second main flow direction was down the valley. Down valley flow typically occurred from evening to the next morning until the up valley flow set in again. As with up valley flow, down valley flow mainly was thermally driven. We assume that down valley flow was enhanced by cold, continuously snow covered, and glacierized northern slopes at the back of the catchment.

Westerly winds occurred during afternoons and the calm transition from up valley to down valley flow. Those flows can be explained by heating the snow free, west facing slopes with the afternoon/evening sun. The resulting anabatic flow led to westerly winds at the bottom of the slopes at Dürrboden. The effects of the few periods of westerly flow on the flux footprints are also visible in Fig. 3.1. Similar cross valley flows have also been observed in an idealized modelling study by Schmidli, 2013. Due to the rare occurrence of flows not aligned with the valley axis, they are combined into the "cross valley" flow group. Table 3.2 gives an overview of the identified flow groups, their wind direction intervals, and the frequency of occurrence.

Table 3.2: Flow direction groups during the observation period.

Flow group	Direction interval [°]	Occurrence	background colour in plots
up valley	$[310, 20]$	19%	orange
down valley	$[130, 200]$	72%	grey
cross valley	$]200, 310[\cup]20, 130[$	9%	white

Wind directions between 320° and 20° are denoted as up valley, and between 130° and 200° as down valley flows. All other flow directions are classified as cross valley.

Table 3.2 also contains the background colour used in Figs. 3.5 and 3.7 – 3.14 to identify the wind direction classes. We used the propeller anemometer at the AWS at a height of 3.5 m above the surface to determine the wind direction classes for the analysis in the following sections.

Mott et al., 2017 also found two main wind directions in the Dischma valley. Using wind speed and direction criteria, they categorized data from three ablation periods into three groups: synoptic south, synoptic north, and thermally driven. Since we focus on small scale processes, the driver of the flow is of minor relevance for the analysis and hereafter we do not distinguish between thermally or synoptically driven flow.

However, a special case is Föhn. During Föhn, increased wind speeds and weaker stability enhance vertical mixing (Drobinski et al., 2007; Haid et al., 2022). At the measurement site, the wind direction during Föhn is south. Since that aligns with the direction of the katabatic flow, it is difficult to separate the two. To classify Föhn and non-Föhn events, we utilize the mixture model presented in Plavcan et al., 2014. The model yields a Föhn probability using wind speed measured at the AWS as a primary classifier. As a concomitant classifier, we chose wind direction and relative humidity measured at the AWS. Furthermore, the model uses the potential temperature difference between a ridge station close to Piz Grialetsch (see Fig. 3.1 for location) and the AWS as a concomitant classifier. The resulting Föhn periods relevant for further analysis are

- 21 May 0000 LT to 25 May 1800 LT, interrupted twice by different flow
- 1 June 0000 LT to 5 June 1500 LT, disrupted and superimposed by thermal and synoptic flows.

For further details we refer the reader to Online Resource 2.

3.4 Separation of Turbulent and Non-Turbulent Motions

To separate turbulent from non-turbulent flow, we computed MRDs for the entire observation period from 21 May to 11 June. Figure 3.6a displays the MRDs for the 2 m level at the ECT, while Fig. 3.6b shows the MRDs for the 5 m EC sensor at the AWS. The MRDs were classified into two categories: statically unstable (positive $\overline{w'T_s'}$, red) and stable (negative $\overline{w'T_s'}$, blue), with stable conditions comprising approximately two thirds of all periods for both sensors.

Upon comparison of the spectral structures of decompositions of both levels during stable periods, we observed similar median values for both levels for $\tau < 100\,\mathrm{s}$. At a measurement height of 2 m, the maximum cospectral contribution is observed at $\tau \approx 2\,\mathrm{s}$, while at a height of 5 m, the maximum contribution was observed at $\tau \approx 10\,\mathrm{s}$. This difference is influenced by differences in stratification and a spatial limitation of the eddy size due to the respective distance to the surface. For $\tau > 100\,\mathrm{s}$, a clear difference is apparent. While the measurement at 2 m above snow shows negligible cospectral contribution, the 5 m measurement at the AWS

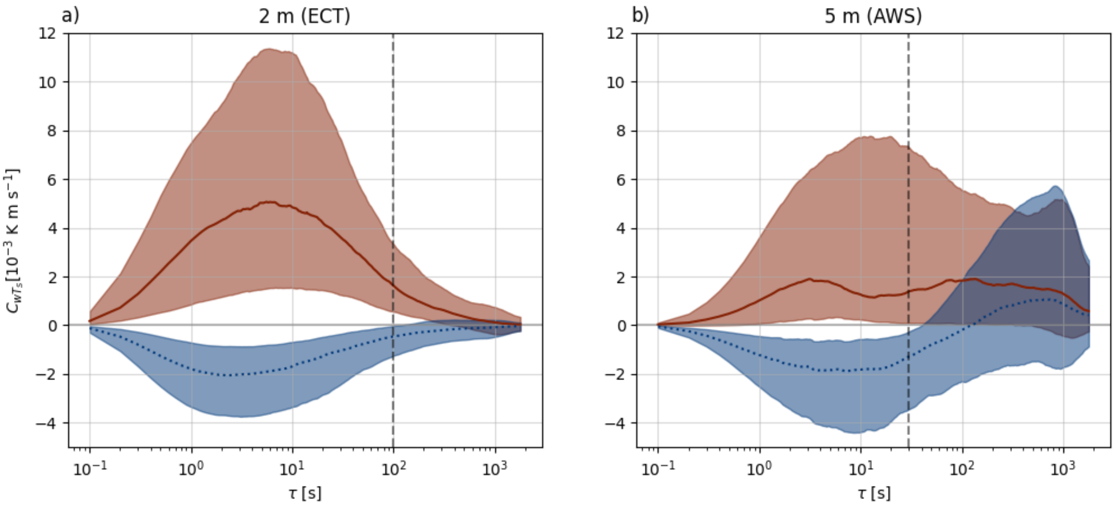

Figure 3.6: **a** MRDs for the EC sensor on the ECT at the height of 2 m above the surface and **b** the EC sensor on the AWS at 5 m above the surface. Red corresponds to unstable, and dotted blue to stable conditions. The solid lines show the median and shaded areas indicate the interquartile range (25% – 75%). The vertical dashed lines indicate the chosen Reynolds averaging time for the corresponding instrument.

reveals substantial cospectral contribution for $\tau > 100$ s. The median of this submeso scale cospectrum at 5 m is positive with a wide interquartile range indicating strong variability.

We obtain a smooth distribution with large variability for the atmospherically unstable periods at the 2 m level. Similar to the decomposition of the stable periods, there is no submeso scale contribution. However, for the EC sensor at the AWS (5 m above the surface), the decomposition is more complex. Two maxima in the median of all decompositions indicate a scale separation between different processes. Furthermore, there is a high variability of the cospectrum for larger scales, suggesting the presence of variable submeso scale motions.

The Reynolds averaging time separates turbulent (shorter time scales) from submeso scale motion (larger time scales) and is used to calculate turbulent fluxes. We followed the approach of Vickers and Mahrt, 2003 to determine the Reynolds averaging time. They propose a cospectral gap between turbulent motion and larger, meso scale motion. Contrary to turbulence, they describe the meso scale motion as chaotic with a large spread. According to Vickers and Mahrt, 2003 and Mott et al., 2020, we used as a criterion for the cospectral gap the time scale at which the upper quartile of the decomposed fluxes becomes positive. We chose a time scale of 100 s for all sensors on the ECT. As visible from Fig. 3.6a, larger time scales did not contribute noticeably to the total flux for both stable and unstable phases. Therefore, the obtained fluxes from the 2 m sensor at the ECT are not very sensitive to the chosen averaging time. It is challenging to define a suitable time scale for the 5 m EC sensor at the AWS. We set the averaging time as 30 s. This is a compromise between unstable and stable periods. For unstable stratification, the local minimum in the median cospectrum indicate a shorter separation time scale ($\approx 20\,\mathrm{s}$). During stable periods, the 75% quartile points towards a longer separation time scale ($\approx 50\,\mathrm{s}$). For consistency, we use 30 s for all stabilities. Similar time scales have been used in other studies (for example Mahrt & Vickers, 2006). Online Resource 3 shows MRDs for all fixed sensors.

3.5 Evolution of Turbulence During the Melt Out

In this part, we aim to gain information on how buoyancy fluxes ($\overline{w'T_s'}$), air temperature heterogeneity represented by sonic temperature variance ($\overline{\left(T_s'\right)^2}$), and turbulence kinetic energy (e) change with a decreasing snow cover fraction. Buoyancy fluxes indicate the local stability at the sensor height. Especially the height of the SIBL can be diagnosed using the buoyancy fluxes (negative/downward fluxes within SIBL, positive/upward fluxes aloft). Furthermore, we use temperature variance as a diagnostic of the changing surface temperature heterogeneity on the near-surface atmosphere. The turbulence kinetic energy e provides information about the time scale of energy containing eddies. In the following, we mostly focus on local processes caused by the presence of snow and bare ground at the measurement site. Additionally, there might be influences by advection from remote sources, such as internal gravity waves.

Figure 3.7 shows moving-window MRDs of the three variables during the entire observation period. The moving-window MRDs in Fig. 3.7b,d, and f reveal strong temporal and spectral heterogeneity throughout campaign. For the following, we separate the observation period into three periods according to characteristics in the spectral decompositions:

- Föhn: 21 to 25 May (interrupted twice) and 1 to 5 June (disturbed by other flow regimes).
- Period 1: 26 May to 1 June, *Deep SIBL*
- Period 2: 5 June to 11 June, *Strong diurnal variations in turbulence characteristics*

The periods are indicated by the bars in Fig. 3.7h. We discuss the periods separately in the following sections.

3.5.1 Föhn

Two Föhn events at the beginning of the observation period are particularly noteworthy. The high wind speeds during those events led to shear generated turbulence and, thus, peaks in the e spectrum at time scales $\mathcal{O}\,(100\,\mathrm{s})$. In contrast, the Föhn event from 1 June to 5 June exhibited less spectral contribution at time scales $\mathcal{O}\,(100\,\mathrm{s})$, which can be attributed to reduced wind speeds and less turbulence generated by shear. As warmer air impinged and partially displaced cold air adjacent to the snow surface during the second Föhn period, we also observed enhanced $\overline{\left(T_s'\right)^2}$ on time scales $\mathcal{O}\,(100\,\mathrm{s})$. Furthermore, during these Föhn periods,

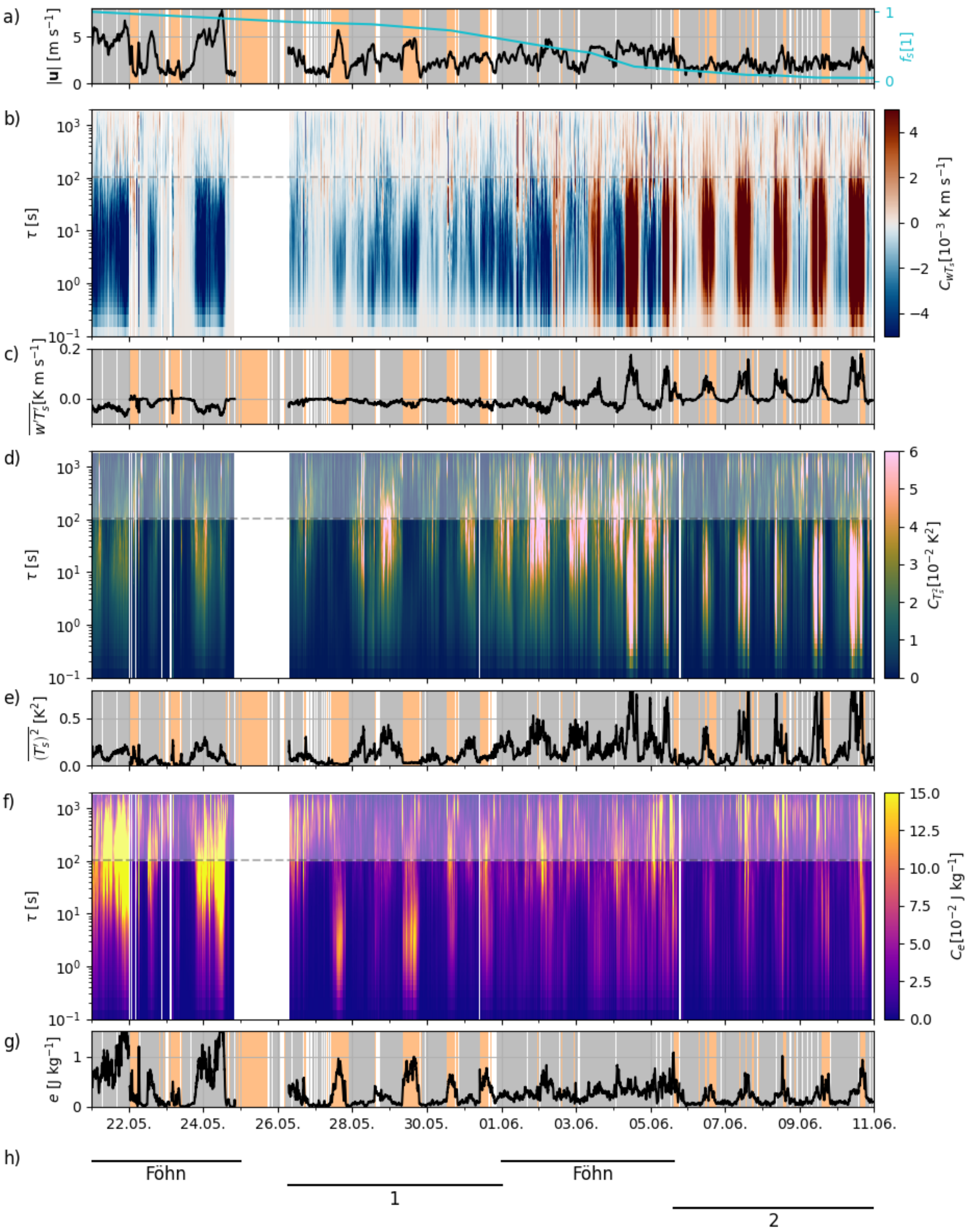

Figure 3.7: Moving-window MRDs of data measured at the 2 m EC sensor at the ECT. **a** The mean wind speed is plotted as a black curve on the left y-axis. The background colours indicate the wind direction class (see Sect. 3.3.2). Orange corresponds to up valley wind, grey to down valley flow, and white denotes wind from other directions. On the right y-axis the snow cover fraction f_s as obtained from the UAV orthophotos is shown. **b, d, e** Moving-window MRD of the buoyancy fluxes $\overline{w'T_s'}$ (b), the sonic temperature variance $\overline{\left(T_s'\right)^2}$ (d), and the turbulence kinetic energy e (f). A vertical slice corresponds to a 'normal' MRD. The x-axes show the time during the observation period, while the y-axes display the time scale τ of the spectral decomposition corresponding to the x-axis in Fig. 3.6. The dashed horizontal lines correspond to the Reynolds averaging time (see Sect. 3.4), splitting turbulence (below) and larger, submeso scale motion (above). **c, e, g** Integral of the decomposed variable for turbulent motion (short time scales up to Reynolds averaging time). The gap from 24 May 1900 LT to 26 May 0700 LT is due to bad weather and a subsequent power outage. **h** indicates the periods that are separately discussed in the following.

we observed pronounced negative values for $\overline{w'T_s'}$ (downward), a pattern consistent with findings from previous Föhn studies (e.g. Drobinski et al., 2007; Haid et al., 2022). However, during the second Föhn period from 1 to 5 June, which was disturbed by non-Föhn periods, we measured positive daytime buoyancy fluxes starting on 2 June. The pattern of the daytime variation after 2 June in Fig. 3.7b resembles the days following the Föhn period. We explain the positive daytime buoyancy fluxes as follows. As visible in the UAV orthophotos in Fig. 3.3, more bare ground emerged south of the snow patch with the ECT. The snow cover fraction on 2 June was $f_s \approx 0.5$. As a consequence, the SIBL depth decreased below the measurement height of 2 m and we measured positive $\overline{w'T_s'}$. These observations suggest that, in case of high surface heterogeneity, the influence of the flow driver (in this instance, Föhn) on the measured turbulence quantities was subordinate. Instead, the snow cover fraction and the local distribution of patches were the dominating factors characterizing the turbulence.

3.5.2 Period 1: Deep Stable Internal Boundary Layer

From 26 May to 1 June, the snow cover fraction was still high. The surface was characterized by snow with, at the beginning, few isolated snow free patches. Towards the end of this period, more bare patches emerged. With the melting snow surface at 0°C, air temperatures > 0°C, and advection of warm air from isolated bare patches, stable internal boundary layers (SIBLs) developed above snow (Garratt, 1990). We measured negative $\overline{w'T_s'}$ (Fig. 3.7c), which indicates that the SIBLs were deep enough to include the EC sensor at 2 m.

Within the SIBL, the main air temperature variances were present on scales $20\,\mathrm{s} \leq \tau \leq 500\,\mathrm{s}$. These variances were increased during nighttime with low wind speeds as visible in Fig. 3.7e and g. According to Zilitinkevich et al., 2007 the observed temperature variance in the stable near-surface atmospheric layer is a measure of the turbulence potential energy. Turbulence is suppressed by the strong stratification in the SIBL over snow and energy is transferred from turbulence kinetic energy to turbulence potential energy. This is supported by an observed decrease in e concurrent with an increase in $\overline{(T_s')^2}$. On the contrary, especially during daytime of 29 May, increased wind speeds led to shear generation of turbulence and thus weaker stability. The total turbulence energy was then mostly contained in e and $\overline{(T_s')^2}$ as a measure of turbulence potential energy, was low.

For e, two different regimes can be observed: On 27 and 29 May, we detected e on short turbulent scales $\mathcal{O}(10\,\mathrm{s})$ similar to the late ablation period (also see Fig. 3.7g). On the other days in this period, we observed mostly larger scale contributions. The time scales of e were similar to the buoyancy-driven e in period 2, when the surface at the measurement site was strongly heterogeneous (see Sect. 3.5.3). In contrast, on 27 and 29 May, the snow cover at the measurement site was still almost continuous. Therefore, we hypothesize that the pronounced up valley winds on those days advected buoyancy-driven, short time-scale turbulence caused by surface heterogeneity further down the valley. We would expect the increased wind speeds to cause shear generated turbulence on scales $\mathcal{O}(100\,\mathrm{s})$ similar to the first Föhn period (21 to

25 May). The factors contributing to the damping of this larger-scale e on 27 and 29 remain unclear.

3.5.3 Period 2: Diurnal variations

As the snow cover fraction f_s further decreased between 5 and 11 June, only few snow patches remained. They were surrounded by large areas of bare ground. We observed pronounced diurnal variations in $\overline{w'T_s'}$. During nights, the radiation balance is negative, resulting in surface cooling. Therefore, typically stable conditions and negative $\overline{w'T_s'}$ prevail. During the day, incoming shortwave radiation results in a positive radiation balance for bare ground and, thus heating the surface. The stability of the near-surface atmospheric layer changes towards statically unstable with more bare ground emerging. The SIBLs adjacent to the snow patches grow only to shallower heights. The lower the f_s, the shallower the SIBLs adjacent to the remaining snow patches are (Mott et al., 2017; Schlögl et al., 2018a) (also see Fig. 3.12 and discussion thereof). Above the SIBL, at the 2 m measurement level, we measured positive $\overline{w'T_s'}$ (upward) indicating an unstable stratification. Thus, layers of different stability alternate within short lateral and vertical distance (Harder et al., 2017; Mott et al., 2017).

Especially the temperature variances show a clear scale transition starting on 4 June. The unstable stratification (TPE not defined, because Brunt–Väisälä frequency becomes imaginary) indicated by positive $\overline{w'T_s'}$, points to the fact that temperature variances need to be interpreted differently. The need for a different interpretation is further indicated by a change in the interplay between temperature variance and turbulence kinetic energy. Earlier, in period 1, temperature variance and turbulence kinetic energy showed alternating peaks: When we measured high $\overline{\left(T_s'\right)^2}$, concurrently e was low, and vice versa. After 4 June, during daytime, both variables peaked simultaneously on turbulent time scales ($2\,\mathrm{s} < \tau < 50\,\mathrm{s}$). We argue that, after 4 June, peaking temperature variance and turbulence kinetic energy reflected the intermittent advection of warm air from bare ground over the snow surface.

In order to facilitate the visualization of this highly dynamic near-surface layer processes, we deployed thin synthetic screens vertically across the transition from bare ground to snow (Haugeneder et al., 2023). The temperature of the screens, captured by a thermal infrared camera, serves as a proxy for the local air temperature. For a more thorough understanding of the following results, we strongly encourage the reader to watch the real time video in Online Resource 4.

The snapshot in Fig. 3.8b visualizes the intermittent advection of a plume of warm air over snow. The plume only affects the atmosphere's lowest $\approx 1\,\mathrm{m}$ at the transition from bare to snow. Aloft and further down wind, colder air is still present. Only 1.6 s later, in the snapshot in Fig. 3.8c, the plume disappeared and the air adjacent to the surface is significantly colder. The strong temporal dynamics reflect the interplay between warm air advected from over bare ground and the cold air adjacent to the snow surface.

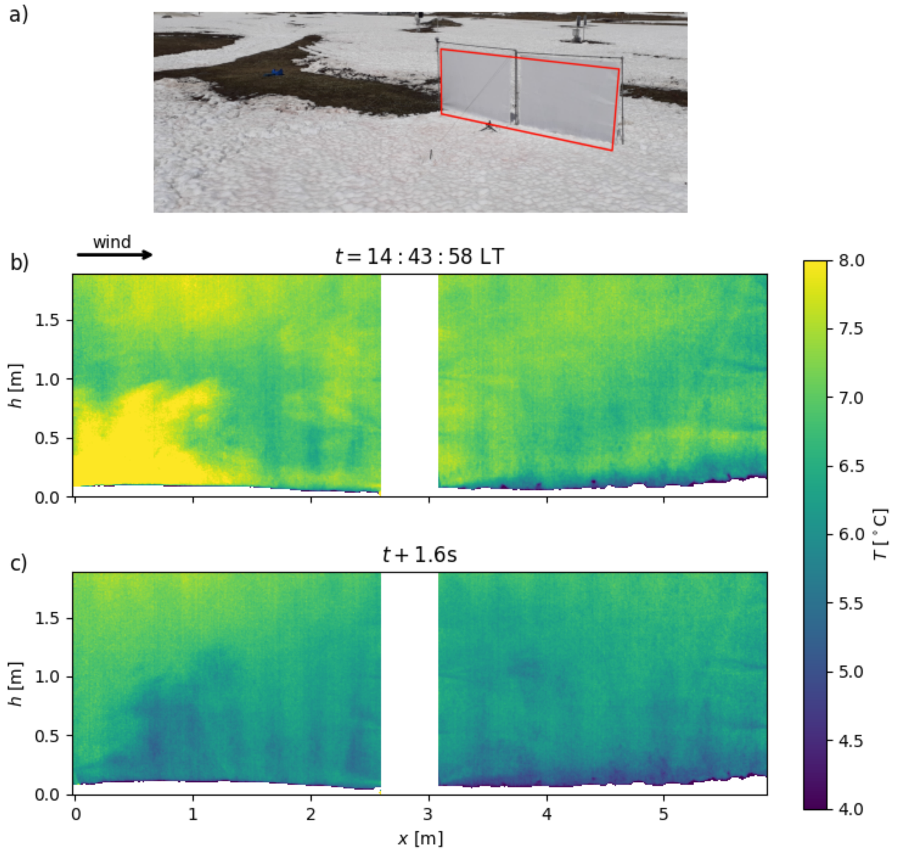

Figure 3.8: Measurements with the screen setup visualizing the temporal dynamics of the atmospheric layer adjacent to the surface. **a** Overview of the set-up. The red box shows the excerpt of the following panels. **b** The thermal infrared snapshot visualizes the near-surface advection of warm air. The x-axis shows the downwind distance from the transition from bare to snow (transition at $x = 0\,\mathrm{m}$). The y-axis denotes the height above the bottom of the frame. The up valley flow blows from left to right as indicated by the arrow. **c** Only 1.6 s later the near-surface atmosphere is a few degrees colder and the warm air plume is not visible anymore.

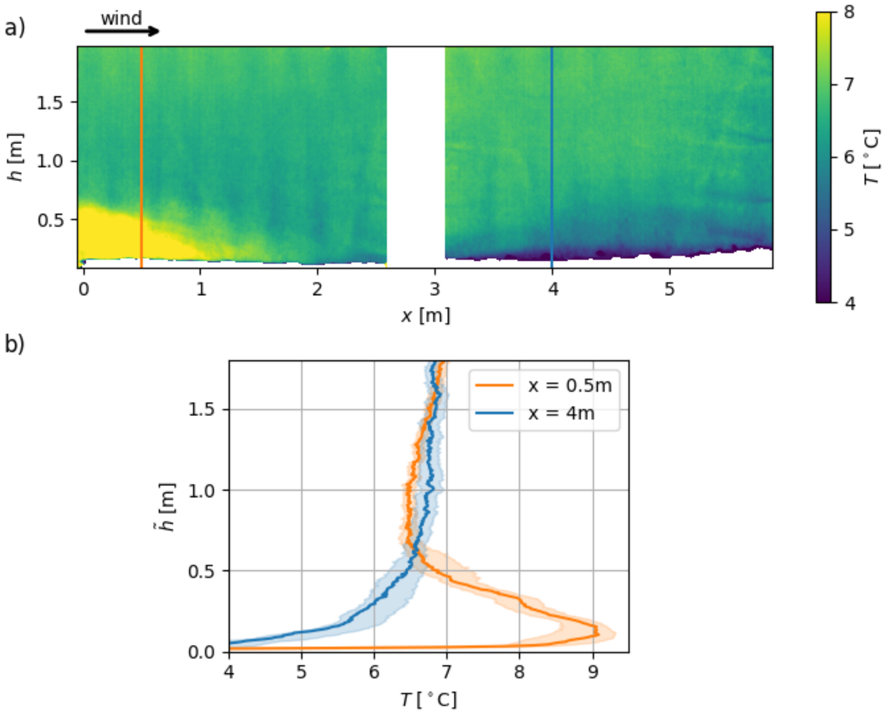

Figure 3.9: **a** Similar figure set-up as in Fig. 3.8b and c. The data are temporally averaged over 1 s. The two vertical lines indicate the location of vertical temperature profiles as shown in **b**. On the y-axis of **b** the height above the snow surface $\tilde{h}$ is plotted. The profiles are averaged over a 20 cm wide column and 1 s. The shaded regions indicate the 25%–75% interquartile range.

The strong spatial heterogeneity is evident in both parts of Fig. 3.9. Within a lateral distance of 3.5 m the air temperatures at 0.2 m above the snow surface differed by 3.5°C due to the intermittent advection of a shallow plume of warm air at the upwind edge of the snow patch. The advection only affected the lowest layer adjacent to the snow surface. It led to a strongly stable stratification within the SIBL. The warm air close to the surface presumably also increased negative buoyancy fluxes and, thus, surface energy input close to the snow at the leading edge. Previous studies have measured the resulting influence of the so-called leading edge effect on the melt rates (Mott et al., 2011; Mott et al., 2018; Schlögl et al., 2018b). Above a height of $\tilde{h} \approx 0.7\,\mathrm{m}$ the atmospheric layer during the snapshot shown in Fig. 3.9b was mixed and there were only minor differences in stratification.

3.5.4 Comparison: High Versus Low Snow Cover Fraction

The difference of the turbulence structure with high and low f_s is further elucidated in Fig. 3.10. In the first period (left column), f_s decreased from 0.80 to 0.70, while in the second period (right column), f_s ranged from 0.19–0.12. Fig. 3.10b shows that negative buoyancy fluxes prevailed in the first period. During daytime, pronounced negative fluxes were caused by increased wind speeds (Fig. 3.10a) and resulting shear driven turbulence. The SIBL was deeper than 2 m, including the EC sensor. Conversely, during the second period, we measured positive $\overline{w'T_s'}$ on turbulent time scales. These positive fluxes indicate a SIBL depth < 2 m. Above the SIBL, at the height of the EC sensor unstable stratification prevailed.

The left column of Fig. 3.10c and d illustrate the conversion between turbulence potential energy and turbulence kinetic energy. The cold snow surface and calm winds during nighttime lead to a strongly stable stratification. Then, increased $\overline{\left(T_s'\right)^2}$ and concurrently almost zero e indicate the substantial mitigation of turbulence and the conversion of e into turbulence potential energy. While increased wind speeds and weaker stratification during daytime favour turbulent energy being contained in turbulence kinetic energy. The increased wind speeds and weaker stratification on 29 May led to less dampened vertical motion and thus more small scale e compared to 30 May. During the second period, daytime increased $\overline{\left(T_s'\right)^2}$ on shorter, turbulence time scales are in line with the observed intermittent advection of warm air (see Figs. 3.8 and 3.9).

3.5.5 Vertical Profiles of Turbulence

The following part aims at examining turbulence at various measurement heights, mainly at the ECT above snow at the transition from bare ground to snow covered surface (c.f. Fig. 3.1 for the position of the ECT). The 5 m measurement was taken at the AWS, while the other three stem from data recorded by sensors at the ECT. Figures 3.11 and 3.12 display decompositions of e and $\overline{w'T_s'}$ at different measurement heights.

The decompositions of e show a similar spectral pattern throughout all heights at the same

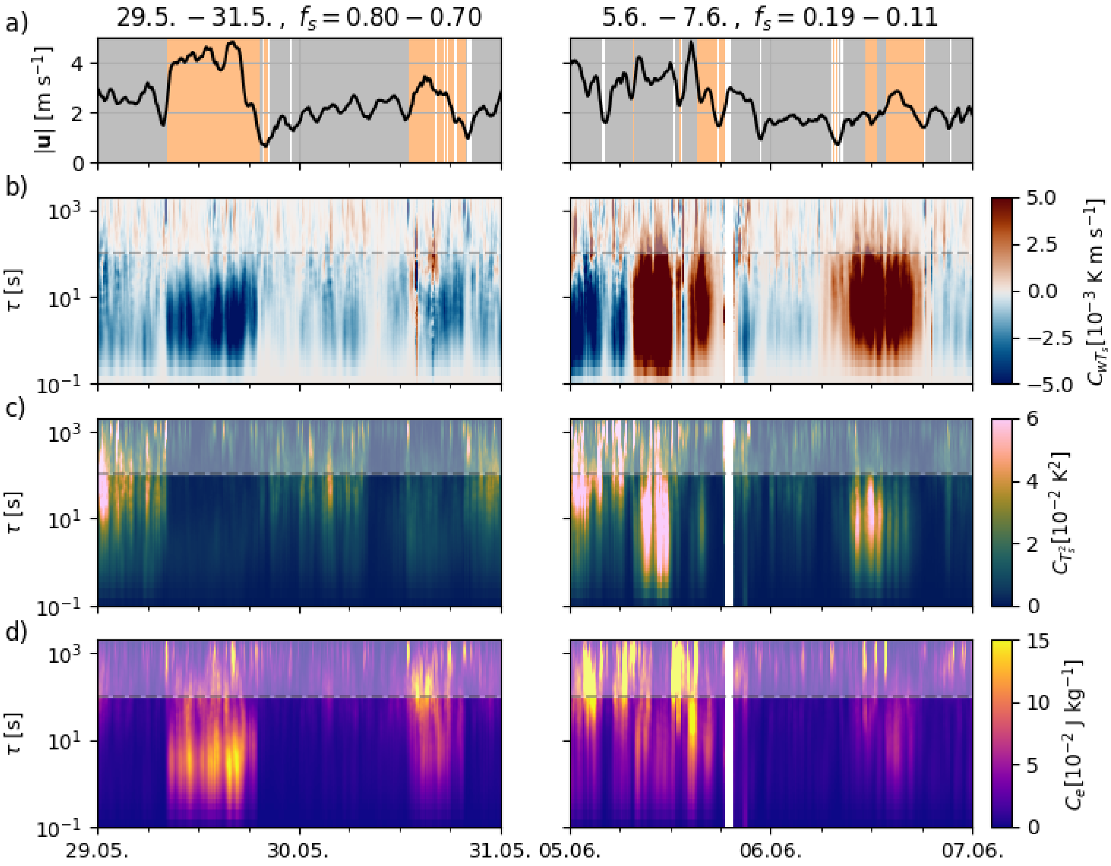

Figure 3.10: Spectral decompositions for two 2 d periods. In the left column data from 29 to 31 May, and in the right column from 5 to 7 June are shown. Furthermore, the range of snow cover fractions f_s is given. In row **a** the wind speed is plotted with background colours indicating the wind direction class. In the following rows, spectral decompositions of buoyancy fluxes $\overline{w'T_s'}$ (**b**), sonic temperature variance $\overline{\left(T_s'\right)^2}$ (**c**), and turbulent kinetic energy e (**d**) are depicted. All data are calculated from the EC measurements at 2 m at the ECT.

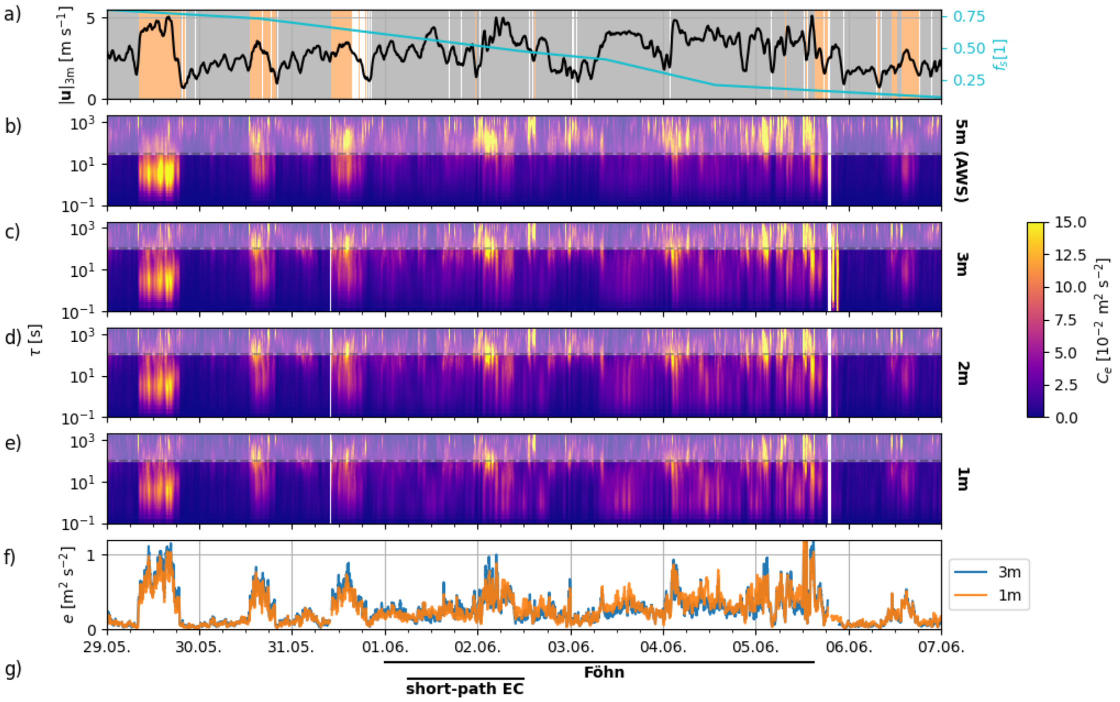

Figure 3.11: Decomposition of e at various measurement heights for 29 May – 7 June. **a** Horizontal wind speed measured at 3 m above the surface on the left y-axis. The background colors indicate the wind direction class. Additionally, we show snow cover fraction f_s on the right y-axis. **b** shows data for the 5 m EC sensor at the AWS. The panels **c, d**, and **e** refer to data measured by instruments at the ECT. The height is indicated on the right. We compare e for 3 m and 1 m measurements in panel **f**. **g** visualizes the Föhn period as identified at the beginning of section 3.5. Furthermore, we show the period with the short-path EC sensor presented in Figs. 3.13 and 3.14.

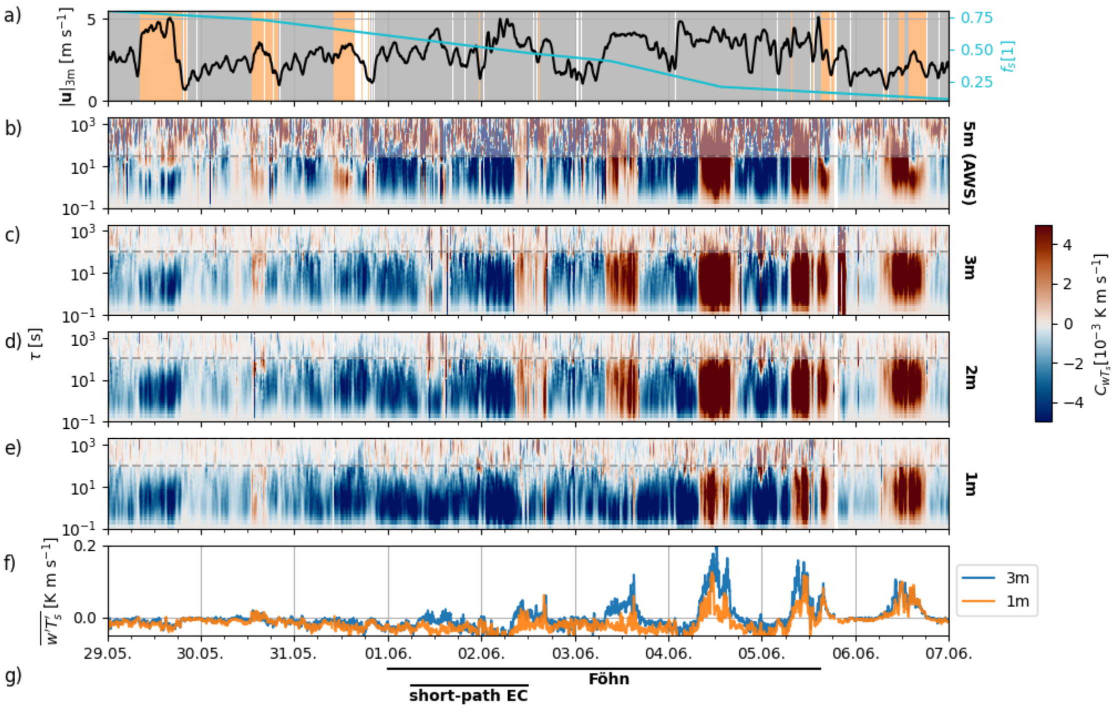

Figure 3.12: Decomposition of $\overline{w'T_s'}$ at various measurement heights for 29 May – 7 June. Similar figure set-up as Fig. 3.11. Horizontal wind speed measured at 3 m above the surface on the left y-axis. The background colors indicate the wind direction class. Additionally, we show snow cover fraction f_s on the right y-axis. **b** shows data for the 5 m EC sensor at the AWS. The panels **c, d**, and **e** refer to data measured by instruments at the ECT. The height is indicated on the right. We compare e for 3 m and 1 m measurements in panel **f**. **g** visualizes the Föhn period as identified at the beginning of section 3.5. Furthermore, we show the period with the short-path EC sensor presented in Figs. 3.13 and 3.14.

measurement time, with both smaller scale turbulence $\mathcal{O}(10\,\mathrm{s})$ and larger scale motions observed in data at all sensor heights simultaneously. Furthermore, the magnitude of e was very similar, as shown for data from 3 m above snow compared to 1 m in Fig. 3.11f. Homogeneous turbulence pattern with height are also confirmed by the $\overline{w'T_s'}$ decompositions in Fig. 3.12b-e before 1 June and after 5 June. Turbulent buoyancy flux spectra showed similar pattern throughout the measurement heights with few exceptions in the 5 m measurement. This homogeneous turbulence (and larger scale motion) pattern with height observed in both decomposition profiles indicates sufficient mixing. Disturbances were coherent, so measurements at all levels were coupled.

The three sensors at the ECT presented in Fig. 3.12c-e exhibited weak spectral contributions beyond the turbulent scale. The majority of the $\overline{w'T_s'}$ spectrum stemmed from short turbulent scales. In contrast, the data at 5 m (Fig. 3.12b) showed substantial contributions from larger scales. These differences are consistent with the clearly larger footprints of the 5 m measurement compared to the lower sensors, as shown in Fig. 3.1. The lack of larger scale contributions for the 2 m measurement and the difference to the 5 m data are also represented by the tails (at longer time scales) of the MRDs in Fig. 3.6.

In the transition period 1 to 5 June, when the snow cover fraction strongly decreased from $f_s \approx 0.6$ to $f_s \approx 0.2$ differences between measurement levels in the $\overline{w'T_s'}$ decomposition became apparent. For example, around midday on 3 June, we measured positive $\overline{w'T_s'}$ at 2 m and negative $\overline{w'T_s'}$ at 1 m. These differences can be explained by the decreasing SIBL depth. As mentioned earlier, the upper SIBL boundary is defined by a change in stability and, thus, a change in sign of the buoyancy fluxes (positive above and negative below SIBL height). Figures 3.12c-e show that on 2 and 3 June, positive buoyancy fluxes were observed for the upper measurement levels, while the 1 m still recorded negative fluxes within the SIBL. Therefore, the SIBL depth was between 1 m and 2 m. From 4 June on, we also measured positive buoyancy fluxes at the 1 m level. The SIBL depth decreased below 1 m. After 5 June, the SIBL is so shallow that all measurement levels are above the SIBL and, thus, are coupled again similar to the earlier period. In contrast to the stable stratification within the SIBL before 1 June, positive buoyancy fluxes indicate an unstable stratification for 6 June.

The dynamics of the SIBL depth are governed by the decreasing snow cover fraction and the resulting increased emergence of bare ground. However, the snow cover fraction as an averaged scalar descriptor of the snow coverage of the (larger surrounding) area is not the only relevant driver. Additionally, the local distribution of patches in the footprint of the EC sensors is important. For example, a longer upwind bare patch leads to warmer air being advected over the snow surface. Consequently, the negative (downward) buoyancy fluxes near the snow surface increase. In the present study, we focus on the turbulence properties above the snow patch and therefore do not take the upwind distribution of patches into account.

3.5.6 Near-Surface Eddy Covariance Measurements

In order to further investigate the processes close to the surface, we deployed a short-path EC sensor at the height of 0.3 m below the sensors of the ECT for a 30 h period. The period is indicated in Figs. 3.11g and 3.12g. Figures 3.13 and 3.14 show decompositions of e and $\overline{(T_s')^2}$ including the 0.3 m data.

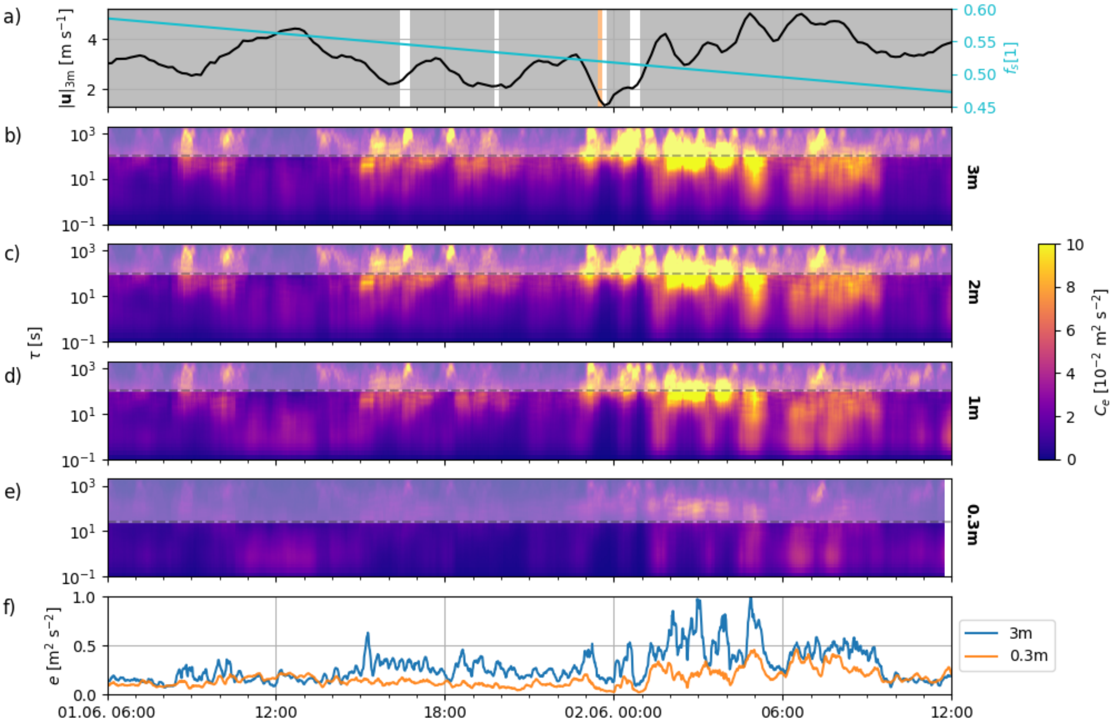

Figure 3.13: Decomposition of e at various measurement heights for a 30 h period when the short-path ultrasonic anemometer was installed below the instruments at the ECT. **a** Horizontal wind speed measured at 3 m above the surface on the left y-axis. The background colors indicate the wind direction class. Additionally, we show snow cover fraction f_s on the right y-axis. **b, c**, and **d** show data measured by instruments at the ECT. **e** refers to data measured by the short-path ultrasonic sensor. The height of all instruments is indicated on the right. We compare e for 3 m and 0.3 m measurements in panel **f**.

Figures 3.13b-e indicate that the spectral pattern of e from aloft (3 m, 2 m, and 1 m) was also present close to the surface (0.3 m). Mostly, the spectral magnitude was reduced towards the surface (c.f. Fig. 3.13f). Additional to the physical limitation of eddy sizes due to the height above the surface, this reduction was probably caused by the strongly stable near-surface stratification over snow. The strongly stable layer adjacent to the surface is also visible in the temperature profiles captured with the thermal IR camera in Fig. 3.9b. However, around midday (1 June 1000 LT – 1500 LT and 2 June 1000 LT – 1200 LT), e close to the surface (0.3 m and 1 m) was nearly as high as at 3 m. During those noon and afternoon times, also the sonic temperature variance at 0.3 m shown in Fig. 3.14e and f was increased. The increase in both

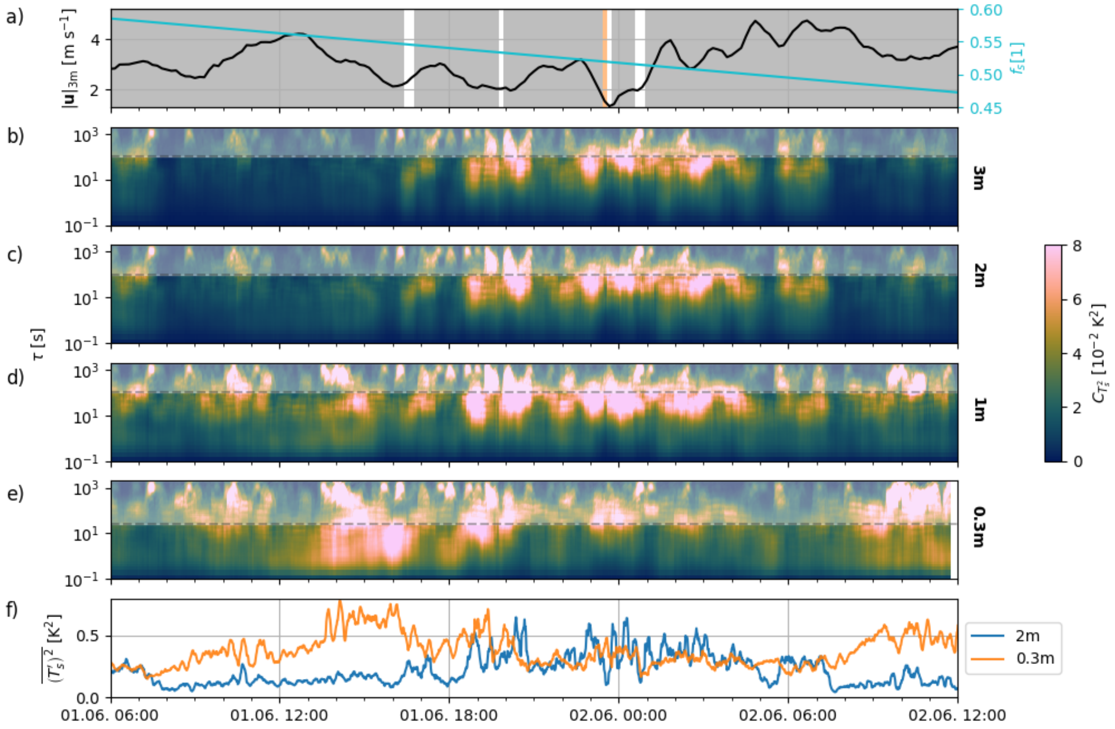

Figure 3.14: Decomposition of $\overline{(T_s')^2}$ at various measurement heights for a 30 h period when the short-path ultrasonic anemometer was installed below the instruments at the ECT. Similar figure set-up as Fig. 3.13. **a** Horizontal wind speed measured at 3 m above the surface on the left y-axis. The background colors indicate the wind direction class. Additionally, we show snow cover fraction f_s on the right y-axis. **b, c**, and **d** show data measured by instruments at the ECT. **e** refers to data measured by the short-path ultrasonic sensor. The height of all instruments is indicated on the right. We compare $\overline{(T_s')^2}$ for 3 m and 0.3 m measurements in panel **f**.

variables mainly stemmed from scales $\tau \leq 10\,\mathrm{s}$. In contrast, the short scale contributions in the $\overline{\left(T_s'\right)^2}$ decompositions at the upper measurement levels (3 m, 2 m, and 1 m shown in Fig. 3.14b-d) were strongly mitigated and hardly recognisable. The upper spectra mostly matched indicating vertical homogeneity above 1 m.

These observations point to a local near-surface process that lead to increased turbulence kinetic energy and sonic temperature variance close to the surface during daytime. As mentioned earlier and visible in the snapshots in Fig. 3.8b the driver was the intermittent advection of warm air. Around midday, solar radiation heated the bare patches up wind of the ECT and the short-path EC sensor. The dynamic interplay between cold air adjacent to the melting snow surface and the intermittent plumes of warm air from bare ground caused the increase in $\overline{\left(T_s'\right)^2}$ and e. At the leading edge of the snow patch (or over the total snow patch, if the snow patch is small) the advected plumes stayed close enough to the ground to only influence the lowest measurement level.

3.6 Conclusion and Outlook

During a snow ablation season, we conducted a comprehensive field campaign in an alpine catchment with a particular focus on characterizing the near-surface atmospheric layer over patchy snow. Our primary objective was to collect eddy covariance data at various measurement levels above the snow, aiming to provide a comprehensive understanding of the dynamics involved. To highlight the different time scales, we investigated spectra of the vertical virtual temperature flux and the turbulence kinetic energy. Analysing the evolution of the spectra over the observation time allowed us to explore the dependency of the findings on meteorological conditions and snow cover fraction. We summarize the results in Fig. 3.15, which displays four distinct periods: The initial Föhn phase with a continuous snow cover (a), advection of warm air from a few bare patches over snow (b), the second Föhn phase over patchy snow (c), and the final period with intermittent advection of warm air plumes over the remaining isolated snow patches (d). The main findings are summarized in the following points.

- During the Föhn periods, we observed pronounced turbulence kinetic energy at scales $\mathcal{O}(100\,\mathrm{s})$. The shear-generated turbulence is indicated by large eddies and wavy transitions in temperature in Fig. 3.15a and c. Additionally, we observed pronounced negative buoyancy fluxes.
- In the early period of snow ablation (Fig. 3.15b), we recorded negative buoyancy fluxes at all measurement levels (1 m, 2 m, 3 m, and 5 m). Later, we measured negative fluxes only at 1 m, while above positive fluxes prevailed during daytime as indicated in Fig. 3.15d. This suggests that the SIBL above the snow patch became shallower as the snow cover fraction decreased over time.
- On 27 and 29 May, we measured turbulence kinetic energy on turbulent time scales,

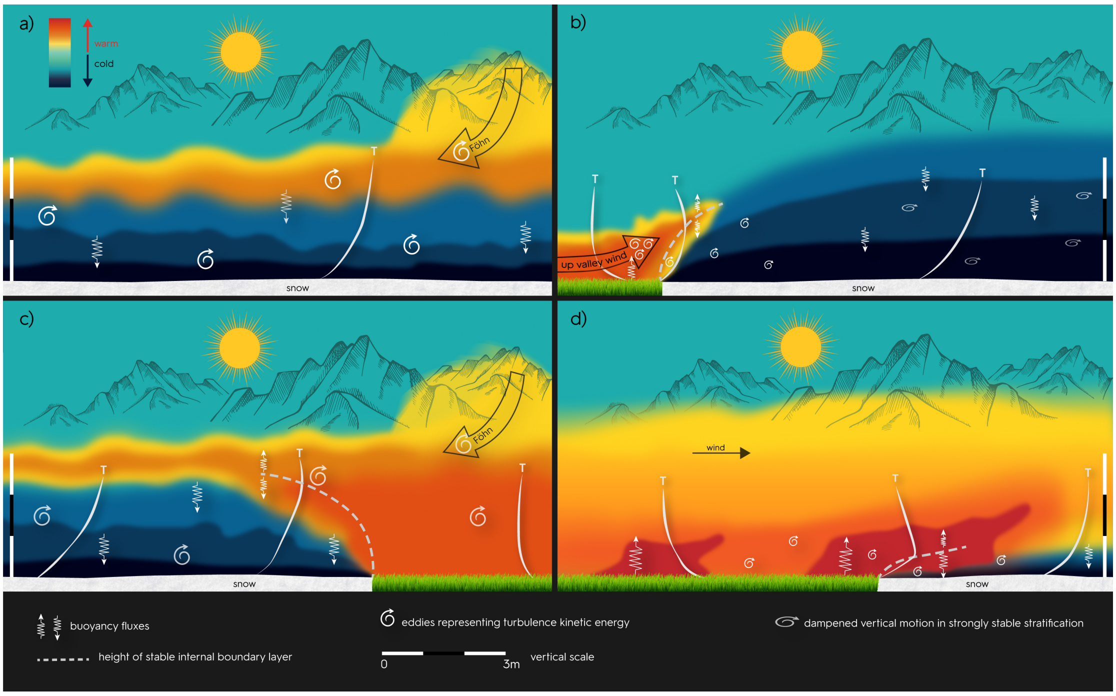
a)
warm
cold
Föhn
T
snow
b)
T
T
T
up valley wind
snow
c)
T
T
T
Föhn
snow
d)
wind
T
T
T
snow
buoyancy fluxes
height of stable internal boundary layer
eddies representing turbulence kinetic energy
0
3m
vertical scale
dampened vertical motion in strongly stable stratification

Figure 3.15: The key phases observed during the campaign: **a** Föhn flow over still continuous snow cover. Intense Föhn flow prevailed over the initially continuous snow cover. The resulting high wind speeds induced shear-generated turbulence kinetic energy, accompanied by pronounced negative buoyancy fluxes. **b** Emergence of bare patches and warm air advection: As the first bare patches emerged, warm air was advected over the advancing leading edge of the snow patch by up valley winds. Calm phases exhibited strongly stable stratification, suppressing vertical motion, as indicated by the flat and faint eddies on the right side. Turbulence energy was predominantly contained in turbulence potential energy during these periods. **c**, Impingement of warm Föhn air: The high wind speeds induced shear-generated turbulence kinetic energy. **d** Intermittent advection over remaining snow patches: As only a few snow patches remained, the near-surface air above bare ground experienced significant heating. This led to intermittent advection of warm air plumes over the snow surface, forming a very shallow Stable Internal Boundary Layer (SIBL).

while on other days in this period, larger scales were present. We hypothesize that the up valley wind advected buoyancy-driven small-scale turbulence as indicated by the small eddies in the left part of Fig. 3.15b.

- The sonic temperature variance showed a transition in time scales as the snow cover diminished. Initially, we found the main spectral contribution to be $\mathcal{O}(100\,\mathrm{s})$ with concurrently low turbulence kinetic energy. As the SIBL depth decreased below the measurement levels, the spectra indicate a shift towards smaller time scales $\mathcal{O}(10\,\mathrm{s})$, while we simultaneously observed an increase in turbulence kinetic energy (small eddies in Fig. 3.15d). We argue that these variances reflect the conversion of turbulence kinetic energy into turbulence potential energy in the strongly stable stratification within the SIBL during the initial period. The very weak turbulence kinetic energy in the strongly stable stratification with dampened vertical motion is indicated by the flat faded eddies in the right part of Fig. 3.15b. Later, with a low snow cover fraction, the variances result from the surface temperature heterogeneity in the immediate vicinity of the remaining snow patch.
- We found a mostly homogeneous pattern of turbulence with height for the measurements at 1 m, 2 m, and 3 m. An exception is when the SIBL depth is within this range, resulting in a sign change of the buoyancy fluxes.
- With strong surface temperature heterogeneity between bare ground and the melting snow, we observed intermittent advection of warm air over the snow (Fig. 3.15d). The plumes of warm air were shallow only affecting the lowest measurement levels up to 1 m.

To generalize the findings, additional data from different campaigns are necessary to cover multiple seasons, different locations, and various meteorological conditions. Furthermore, measurements over melting ice can help to transfer the described findings to the near-surface atmosphere over glaciers and gain information on summer-time glacier–atmosphere interaction and its consequences on summer-time glacier mass loss. The resulting knowledge will enable us to improve parameterizations of lateral heat advection in coupled hectometre-scale surface–atmosphere models. These models can investigate the accumulated effect over catchments and entire seasons.

Data and Code Availability

Data is available at doi:10.16904/envidat.399. Documented source code can found at https://github.com/michhau/turbpatchsno.

4 Large Eddy Simulation of Near-Surface Boundary Layer Dynamics over Patchy Snow

This chapter corresponds to the version of the article submitted to the journal *Frontiers in Earth Science: Cryospheric Sciences* by the authors

Michael Haugeneder, Michael Lehning, Océane Hames, Mahdi Jafari, Dylan Reynolds, and Rebecca Mott

Abstract

The near-surface boundary layer over patchy snow is highly heterogeneous and dynamic. Layers of opposing stability coexist within only a few horizontal meters. Conventional experimental methods to investigate this layer suffer from limitations related to the fixed positions of eddy covariance sensors. To overcome these difficulties, we set up a centimeter resolution large eddy simulation of flow across an idealised transition from bare ground to snow. We force the simulation with high-frequency eddy covariance data recorded during a field campaign. We show that the model can represent the real flow by comparing to independent eddy covariance data. However, the simulation underestimates vertical wind speed fluctuations, especially at high frequencies. Sensitivity analyses show that this is influenced by grid resolution and surface roughness representation but not much by subgrid-scale parameterization. Nevertheless, the model can reproduce the experimentally observed plumes of warm air intermittently detaching from bare ground and being advected over snow. This process is highly dynamic with time scales of only a few seconds. We can show that the growth of a stable internal boundary layer adjacent to the snow surface can be approximated by a power law. With low wind speeds, deeper stable layers develop, while strong wind speeds limit the growth. Even close to the surface, the buoyancy fluxes are heterogeneous and driven by terrain variations, which also induce the frequent decoupling of a thin layer adjacent to the

snow surface. Our simulations point the path towards generalizing point-based and aerial measurements to three dimensions.

4.1 Introduction

In spring, the snow that has accumulated throughout the winter begins to melt. The resulting run-off plays a crucial role, for example, for the ecosystem (Groffman et al., 2001; Rixen et al., 2022; Wheeler et al., 2016; Wipf & Rixen, 2010), drinking water supply (Siirila-Woodburn et al., 2021; Sturm et al., 2017), or hydropower generation (Magnusson et al., 2020; Stucchi et al., 2019). Furthermore, in combination with precipitation, it can amplify the risk of flooding and associated damages (D. Li et al., 2019; Mott et al., 2023b; Sui & Koehler, 2001; Würzer et al., 2016), underscoring the necessity for a precise understanding and prediction of snowmelt dynamics.

The mountain snow cover is heterogeneous on a wide range of scales shaped by accumulation and ablation processes. Preferential deposition (Lehning et al., 2008), wind-induced snow transport (Föhn & Meister, 1983; Pomeroy & Gray, 1995), and avalanches lead to spatially varying snow depth (Quéno et al., 2023; Reynolds et al., 2024). These spatially irregular accumulation features, together with spatially heterogeneous melt, support the formation of patchy snow covers later in spring. Due to its lower albedo, the bare ground heats up faster than adjacent snow patches. In numerical simulations, studies by Ménard et al., 2014b, Letcher and Minder, 2017, and Schlögl et al., 2018a demonstrated the resulting warming feedback for the near-surface atmosphere. The surface temperature of the snow is constrained by its melting temperature of 0 °C. Consequently, there is a strong horizontal heat flux divergence between positive heat fluxes above bare ground and negative heat fluxes over snow-covered areas (Mott et al., 2015; Schlögl et al., 2018a).

Local-scale winds, influenced by small-scale surface temperature variations (Johnson et al., 1984) interact with larger-scale circulations such as valley breezes. The valley breeze, in turn, is influenced by an elevation gradient in snow cover: Lower parts of the valley are already snow-free, while higher up, the snow cover is still continuous (Farina & Zardi, 2023). The resulting winds mix the heterogeneously stratified air masses above the patchy snow cover. Warm air from bare ground is advected over snow-covered areas, leading to a strongly stratified layering. Close to the snow surface, a stable internal boundary layer (SIBL) forms (Garratt, 1990). A change in sign of sensible heat fluxes defines its upper boundary. Within the SIBL, negative (downward) fluxes prevail, while above it, positive (upward) fluxes align with the locally unstable stratification. The depth of the SIBL fluctuates rapidly depending on various parameters such as wind speed or stability (Mott et al., 2013; Schlögl et al., 2018a). Thus, the feedback loops between heterogeneous surfaces in spring, the near-surface atmosphere, and the snow-atmosphere interaction processes are highly complex. Further experimental studies are essential for a comprehensive understanding and the development of valid parameterizations for models.

Experimentally investigating the atmosphere close to the surface poses some difficulties.

Conventional eddy covariance (EC) measurements are limited to fixed positions and can not be deployed arbitrarily close to the surface (Stiperski & Rotach, 2016). Granger et al., 2006 performed temperature profile measurements at several positions across the transition from bare ground to snow using fine-wire thermocouples. However, this setup can also only sample data at limited locations. Recently, Haugeneder et al., 2023 adapted an approach from Grudzielanek and Cermak, 2015b that allows aerial estimations of air temperature and wind speed close to the surface. In this technique, a thermal infrared camera pointing to thin vertically deployed synthetic screens records frames at 30 Hz. Since the screens have a low heat capacity, their surface temperature can be used as a proxy for the local air temperature. The measurements offer a spatial resolution of 0.5 cm and give insights into the dynamics of the near-surface atmospheric layer. However, they represent only snapshots in time and are confined to small measurement domains. Obtaining a comprehensive understanding of spatial dynamics solely from such measurements is challenging.

High-resolution numerical simulations offer the possibility to bridge the gap between point or aerial measurements and a full three-dimensional representation of the flow across the transition from bare ground to snow. The basis of most fluid dynamics simulations is the Navier-Stokes equations. The coupled system of partial differential equations describes and predicts the three-dimensional momentum field. A common technique to solve the coupled system is the Reynolds-averaged Navier-Stokes (RANS) approach. The Navier-Stokes equations are solved in RANS for time-averaged quantities, and turbulent motions of higher frequencies are parameterized. Due to its computational efficiency, it is used for modeling studies of the ABL (e.g. Balogh et al., 2012; Hames et al., 2022). It has also been used to study atmosphere-cryosphere interactions(Hames et al., 2022; Jafari et al., 2022). Challenges arise when the focus of the research is on turbulent quantities. Naturally, turbulence is not steady-state but transient. Therefore, only looking at time-averaged quantities does not yield enough information.

On the opposite side of the complexity spectrum for solving fluid dynamics problems is direct numerical simulation (DNS) (Pope, 2000). The Navier-Stokes equations can be accurately solved in idealized scenarios with relatively moderate Reynolds numbers. Eddies of all scales are directly resolved, and therefore no turbulence parameterization is necessary. For example, van der Valk et al., 2021 use a DNS model to simulate the near-surface boundary layer over patchy snow. Using temperature profile measurements above patchy snow from Harder et al., 2017, they found spatial variability in sensible heat fluxes that result in spatially heterogeneous melt rates. However, this computationally costly approach is limited to highly idealized conditions.

Large Eddy Simulations (LES) act as a robust intermediary, filling the complexity gap between RANS and DNS. By spatially filtering the Navier-Stokes equations, LES directly represents supra-filter scale motions while parameterizing sub-filter motions (Pope, 2000). Relevant energy-containing scales are directly resolved by choosing a suitable filter scale. In recent decades, multiple studies have applied the LES approach to study ABLs of various stability on a wide range of scales. Some more recent studies include Huang and Bou-Zeid, 2013; Melo et al., 2024; Richardson et al., 2013; Sigmund et al., 2022; Smith and Porté-Agel, 2014; Zahn and

Bou-Zeid, 2024; Zwaaftink et al., 2014. The review of Stoll et al., 2020 provides a comprehensive overview of studies.

In this work, we set up, validate, and analyze an LES simulation to study the near-surface atmosphere adjacent to the transition from bare ground to snow. We aim to generalize data recorded during a previous field campaign to get more information on the fetch dependence of heat fluxes close to the surface. Therefore, Sect. 4.2 gives an overview of the experimental data and the setup of the model followed by a validation of the model results with measurements in Sect. 4.3. In Sect. 4.4 we use the simulation results to investigate the near-surface boundary layer dynamics. Specifically, we examine the intermittent advection of plumes of warm air over the snow and the spatial and temporal dynamics of the SIBL. Furthermore, in Sect. 4.4.3 we analyze the dependence of vertical profiles of temperature and wind speed, as well as the SIBL depth, on wind speed. Section 4.5 summarizes the findings and gives a brief outlook.

4.2 Methods

4.2.1 Study Site

In late spring 2021, we collected data during a comprehensive field campaign in the Dischma valley near Davos (Switzerland). The valley axis of the straight high alpine valley is oriented in the southeast-northwest direction. Steep slopes enclose the valley floor with an elevation difference of approximately 1000 m. The area has been extensively studied (Bavay et al., 2009; Brauchli et al., 2017; Carletti et al., 2022; Gerber et al., 2019; Lehning et al., 2006; Mott et al., 2017; Reynolds et al., 2023; Schlögl et al., 2018b, 2018a; Urfer-Henneberger, 1970; Wever et al., 2017). Dürrboden, the flat measurement site at an elevation of 2010 m a.g.l., is located at the end of the valley. The map in Fig. 4.1 gives an overview of the area. The right part of Fig. 4.1 shows an aerial overview picture captured on 30 May 2021 by an Uncrewed Aerial Vehicle (UAV). Bare patches have already emerged.

To force and validate the LES simulation presented in this study, we use eddy covariance (EC) data recorded during this campaign. We deployed multiple sensors at various locations and heights. We installed two IRGASONs (Campbell Scientific, Logan, Utah, USA) on ECT1 at 1.2 m above the surface and on ECT2 at 0.9 m above the surface. Furthermore, at ECT2, we installed two CSAT3Bs (Campbell Scientific, Logan, Utah, USA) at heights of 1.9 m and 2.9 m, together with a Campbell PT1000 ventilated air temperature sensor (Campbell Scientific, Logan, Utah, USA) positioned at 1 m above the surface. All EC sensors recorded data at a sampling frequency of 20 Hz. The lines in the UAV image indicate the 80% flux footprints as described by the parameterization of Kljun et al., 2015. For interpretation, we note that the LES simulation is forced with data taken on 31 May 2021, so one day after the UAV image in Fig. 4.1 was taken. During this period of snow melt, bare patches emerge and extend rapidly. For the snow cover on 31 May, the area within the flux footprints of both ECTs was mostly snow-covered. The automatic weather station (AWS) was installed ≈ 30 m upwind of the ECTs. In the present study, we use air temperature measured at the height of 3.7 m above the surface by a HygroVue 5 (Campbell Scientific, Logan, Utah, USA). The AWS recorded data averaged

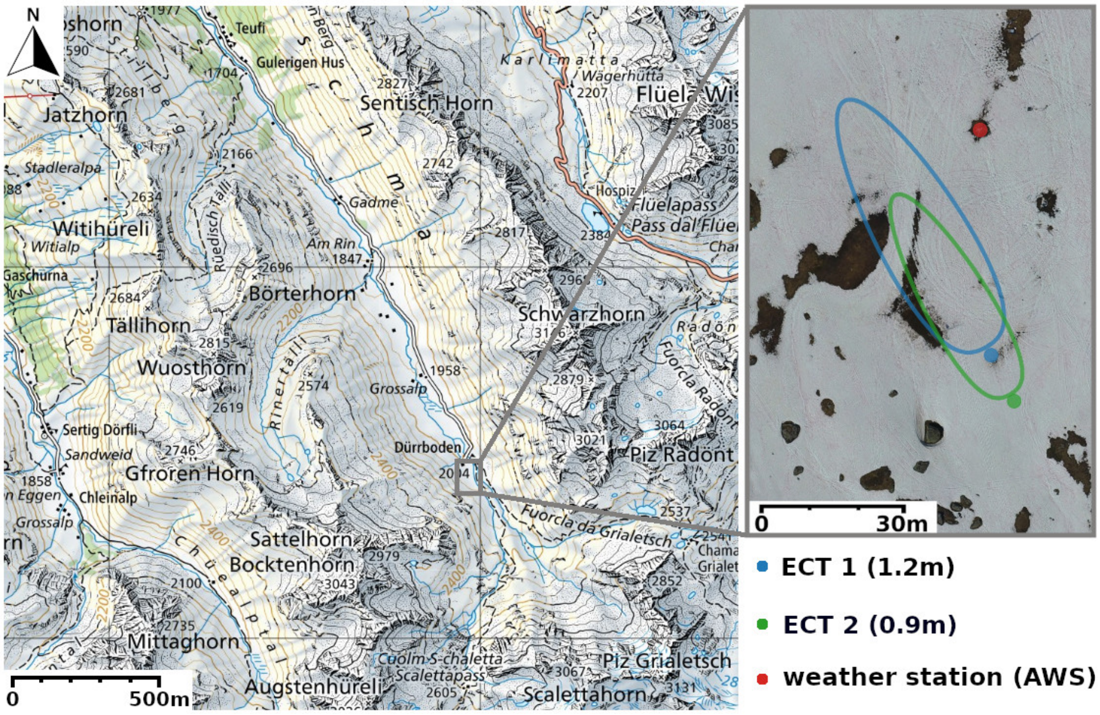
N
0
500m
0
30m
● ECT 1 (1.2m)
● ECT 2 (0.9m)
● weather station (AWS)
Jatzhorn
Witihüreli
Tällihorn
Wuosthorn
Börterhorn
Sentisch Horn
Gfroren Horn
Sattelhorn
Bocktenhorn
Mittaghorn
Augstenhüreli
Schwarzhorn
Piz Radönt
Piz Grialetsch
Scalettahorn
Dürrboden
Flüelapass
Scalettapass

Figure 4.1: Topographic map of the Dischma valley end close to Davos (Switzerland). In the gray box, an orthophoto (30 May 2021) obtained from an Uncrewed Aerial Vehicle shows the flat study site with measurement stations including two eddy covariance towers (ECT) and an automatic weather station (AWS). Additionally, the 80% flux footprints according to Kljun et al., 2015 are shown for EC measurement at a height of 1.2 m at the ECT1 (blue line) and for a 0.9 m measurement at the ECT2 (green line).

every 10 min.

In addition to conventional EC measurements, we deployed thin synthetic screens vertically positioned across the transition from bare ground to snow. Using a thermal infrared camera to film these screens, we obtained surface temperatures at a spatial resolution of 0.6 cm and a temporal resolution of 30 Hz. The screens are thin enough to quickly adjust to the ambient air temperature. Therefore, the recorded surface temperature of the screens serves as a proxy for the local air temperature. The data visualizes the temperature stratification and its dynamics adjacent to the surface. In the following, we will refer to this setup as the IR setup. We refer the reader to Haugeneder et al., 2023 for further details about the field campaign.

4.2.2 LES

This study aims to set up, validate, and analyze a high resolution numerical simulation of atmospheric flow over a single bare ground to snow transition forced with measurement data collected as described above. Therefore, we employ a large-eddy simulation (LES). LESs were first introduced in 1963 by Smagorinski, 1963. Since then, the approach has grown rapidly and has become a popular and powerful tool to investigate atmospheric processes on various scales (Stoll et al., 2020).

In the following, we quickly summarize the basic concept and equations, which are important for the interpretation of the later results. For easier notation, we use the Einstein summation convention, in which a summation over the three spatial directions x, y, and z is implied for repeated indices. As an example, we show the momentum equation.

The Navier-Stokes equations for incompressible flow predict the three-component velocity field u_i at time t.

$$\frac{\partial u_i}{\partial t} + u_j \frac{\partial}{\partial x_j} u_i = \nu \frac{\partial^2 u_i}{\partial x_j \partial x_j} - \frac{1}{\rho} \frac{\partial p}{\partial x_i}. \tag{4.1}$$

ν describes the kinematic viscosity, ρ the fluid density and p the pressure including gravitational pressure (Pope, 2000). For simplicity, we drop the buoyancy term, which can be written in the Boussinesq approximation as $-\delta_{iz} g \alpha \Delta T$, where g denotes the gravitational acceleration (in the downward z-direction), α the thermal expansion coefficient, and $\Delta T = T - T_0$ the difference between the local temperature and a reference temperature. The additional variable T can be solved by utilizing energy conservation.

Directly solving Eq. (4.1) and the incompressible continuity equation

$$\frac{\partial u_i}{\partial x_i} = 0 \tag{4.2}$$

is known as Direct Numerical Simulation (DNS). Due to the tremendous computational costs, this is (to date) only possible for highly idealized conditions. To reduce the computational demands, Eq. (4.1) can be filtered. The filter, which can take on various shapes such as spectral cut-off or Gaussian, separates resolved large scale motions from non-resolved and thus parameterized subgrid scale (SGS) motions. This filtering step is the cornerstone of LES modelling. In our case, filtering is achieved implicitly by discretizing the mesh (Lund, 2003). We give a more detailed description of the model setup in Sect. 4.2.3. The filtered Eq. (4.1) are

$$\frac{\partial \overline{u_i}}{\partial t} + \frac{\partial \overline{u_i u_j}}{\partial x_j} = \nu \frac{\partial^2 \overline{u_i}}{\partial x_j \partial x_j} - \frac{1}{\rho} \frac{\partial \overline{p}}{\partial x_i}, \tag{4.3}$$

where variables with an overbar denote filtered quantities. The second term presents a challenge: $\overline{u_i u_j}$ is the filtered product of two unfiltered quantities u_i and u_j. This means that to solve Eq. (4.3), knowledge about unfiltered quantities is necessary. This problem is solved by parameterizing the anisotropic residual stress tensor $\tau^r_{ij} = \tau^R_{ij} - \frac{1}{3}\tau^R_{ii}\delta_{ij}$ where the residual stress tensor is given by $\tau^R_{ij} = \overline{u_i u_j} - \overline{u_i} \cdot \overline{u_j}$ (Pope, 2000). Multiple approaches with different levels of complexity are available for this SGS parameterization. Despite more sophisticated parameterizations having been suggested (e.g. dynamic SGS model (Germano et al., 1991), Lagrangian dynamic model (Meneveau et al., 1996), or SGS models solving a transport equation (Deardorff, 1974)), we use the computationally efficient Smagorinski-Lilly SGS model (Smagorinski, 1963). From sensitivity analysis we found no strong change in the results when we used, for example, a dynamic Lagrangian SGS model.

The Smagorinski-Lilly SGS model utilizes the concept of viscosity and builds upon the presence of an inertial subrange (Stoll et al., 2020). Within the frequency range of the inertial subrange, turbulent energy is transferred, in the mean, only from larger to smaller scales (Kolmogorov, 1941). If the filter is chosen to be in the inertial subrange, Smagorinski, 1963 hypothesize a linear relation between the anisotropic residual stress and the filtered rate of strain $\overline{S_{ij}}$

$$\tau^r_{ij} = -\nu_r \left(\frac{\partial \overline{u_i}}{\partial x_j} + \frac{\partial \overline{u_j}}{\partial x_i} \right) = -2\nu_r \overline{S_{ij}}, \tag{4.4}$$

where

$$\nu_r = (C_S \Delta)^2 \sqrt{2\overline{S_{ij}}\,\overline{S_{ij}}} \tag{4.5}$$

describes the eddy viscosity, C_S the Smagorinski coefficient and $\Delta = \left(\Delta_x \Delta_y \Delta_z\right)^{\frac{1}{3}}$ the filter width. A disadvantage of the Smagorinski-Lilly SGS model is that it is purely dissipative and not representing the true equilibrium between forward and backward scatter (Stoll et al., 2020). Backward scattering, i.e. the influence of non-resolved subgrid scale motion on resolved scales, can significantly modify the flow field (Leslie & Quarini, 1979).

4.2.3 Model Setup and Forcing

We set up the LES simulation across an idealized transition from bare ground to snow. The computational domain spans 20 m along the flow direction (x), 6 m in across-flow direction (y) and is 5 m high (h). We use a horizontal cell width of $\Delta x = \Delta y = 0.04$ m with a vertical cell height of $\Delta h = 0.03\,\mathrm{m} - 0.07\,\mathrm{m}$. The smallest cells are at the bottom of the domain. With these cell sizes, the simulation includes about 7.7×10^6 cells. We use adaptive time-stepping to prevent excess Courant numbers that could cause numerical instability (Moukalled et al., 2016). Throughout the simulation, the median time step is $\overline{\Delta t} = 8 \times 10^{-3}$ s.

To allow for forcing with high-frequency EC measurements, we use inflow-outflow boundary conditions in the x direction and cyclic boundaries in the y direction. We apply a zero-gradient Neumann boundary condition for momentum and temperature as an upper boundary condition.

The transition between bare ground and snow in the model at $x = 8$ m is characterized by a change in surface roughness and surface temperature. There were many old footsteps on the snow surface. We estimated the height of the roughness elements on snow from field observations to be ≈ 0.1 m. We assumed a height of the roughness elements of ≈ 0.05 m for grass. For generating rough surfaces, we use the open-source Python library tamaas (available from https://gitlab.com/tamaas/tamaas/-/tree/master). It generates random rough surfaces by back-transformation of a given spectrum. To account for the different structures of the surfaces, we not only changed the height of the roughness elements, but also the frequencies contained in the spectrum. For grass, we included higher frequencies to represent finer structures. We set the surface temperature of the snow to the melting point at 0 °C. Using data collected from the thermal infrared camera, we approximated the temperature of the bare ground at 15 °C.

We force the simulation directly with high-frequency EC measurements. To our knowledge, this has not yet been done in such a setup. Figure 4.2 gives an overview of the domain in relation to the available EC sensors. We chose the location of the domain such that the flow resembles the data captured by the IR screen setup. The idea is to apply the larger scale forcing via measured wind speeds and air temperatures and let the model simulate the surface-driven

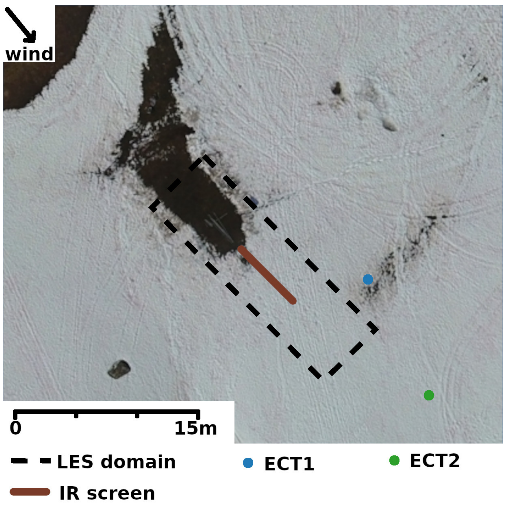

Figure 4.2: Location of the LES simulation domain (dashed black box) in relation to the measurement locations. The UAV image is a cutout from the one in Fig. 4.1.

buoyancy effects at the transition from bare ground to snow.

For wind speed forcing, we fit a logarithmic wind profile (log-profile) through the median of 5 min EC data from three sensors at ECT2. To obtain a high-frequency wind profile, we scaled the log-profile to the data measured at 0.9 m above the surface at ECT2.

A challenging task in LES modelling is to obtain realistic turbulence at the inlet. We use the divergence-free synthetic eddy method (DFSEM) developed by Poletto et al., 2013. The method generates realistically shaped eddies according to a given mean wind speed, Reynolds stress tensor, and turbulence integral length scale. We use 20 Hz horizontal wind speed data and calculated the Reynolds stress tensor from the 0.9 m EC sensor at ECT2. We also estimate the turbulence length scale from an auto-correlation analysis of this data. Additionally, we assume that the Reynolds stress tensor and the turbulence length scale are constant in the horizontal and vertical directions.

We do not apply vertical wind speed forcing, since we do not have enough measurement data to realistically interpolate, accounting for larger-scale vertical motions. However, the turbulent part of the vertical wind speed is generated by the DFSEM.

For temperature forcing, we use the upwind measurement at the AWS at 3.7 m height (see Fig. 4.1). Since the AWS recorded data only every 10 min, we use the 5 s variations recorded by the ventilated thermometer at ECT2 scaled to the mean temperature measured at the AWS. We then logarithmically scale the air temperature to the surface temperature of bare ground of 15 °C (Högström, 1996).

For the analysis in this study, we extract data on a slice aligned with the wind direction at $y = 3\,\text{m}$. Furthermore, to account for the spin-up of the simulation, we discard the first 10 s of data.

For the simulation, we use the *buoyantBoussinesqPimpleFoam* solver (OpenFoam API Guide, 2024) available from the open-source fluid dynamics platform OpenFOAM (Weller et al., 1998). The transient solver is designed for incompressible flow. OpenFOAM uses a finite volume method for discretization.

4.3 Validation of Model Results Against Measurements

In this section, our objective is to compare the LES simulation results with eddy covariance (EC) measurements. Therefore, we use the EC measurement at 1.2 m height on the ECT1. This particular EC measurement, not included in the initial model forcing, serves as an independent means of validation. Extracting data from the simulation domain at $x = 10.0\,\text{m}$, $y = 3.0\,\text{m}$, and $z = 1.2\,\text{m}$ ensures a sufficient downwind distance to the transition from bare ground to snow. However, when interpreting the results, the reader should keep in mind that the flux footprint of the 1.2 m measurement on the ECT1 (cf. Fig. 4.1) hardly contains any bare ground. Figure 4.3 compares the LES simulation with the EC measurement. We discard the first 10 s of the simulation results for flow spin up.

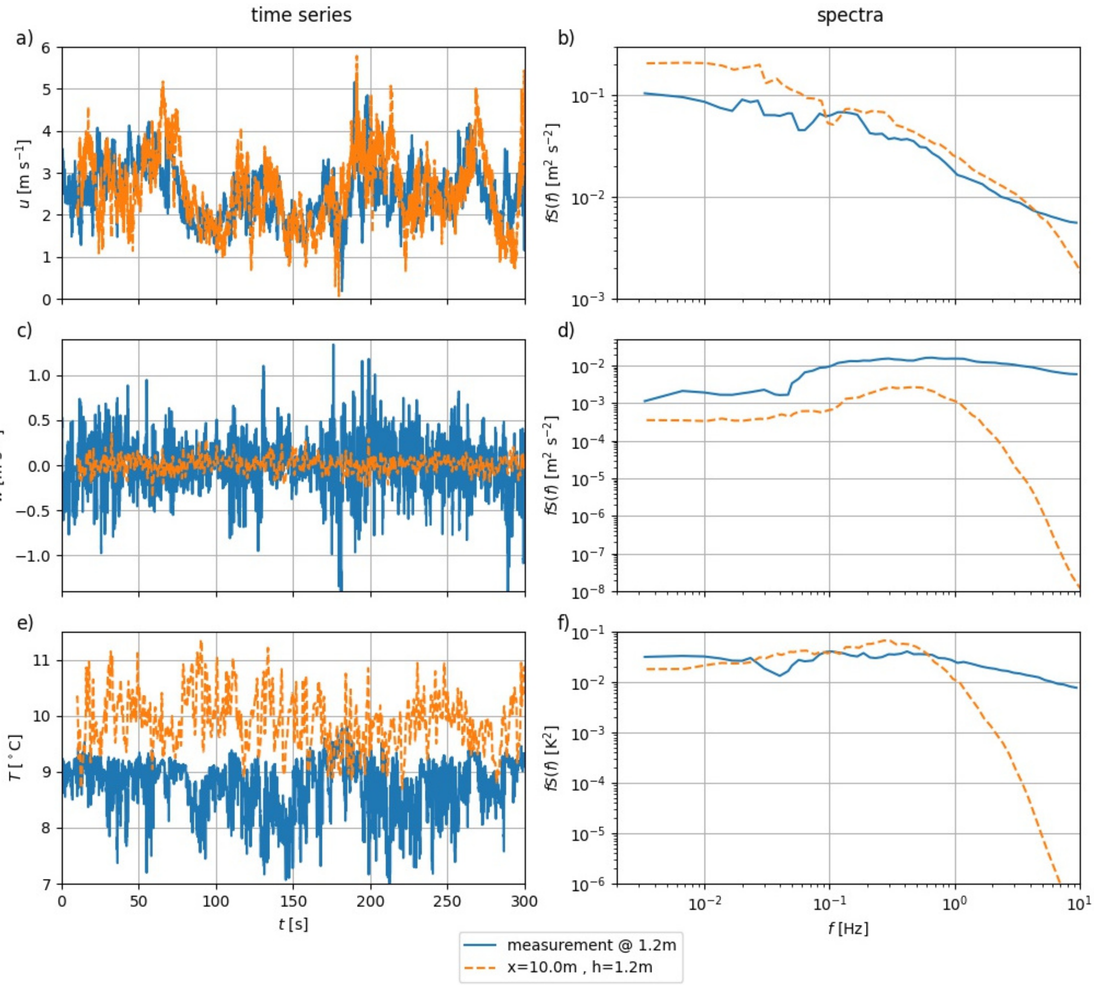

Figure 4.3: Comparison of model output at $x = 10.0\,\mathrm{m}$, $y = 3.0\,\mathrm{m}$, and $z = 1.2\,\mathrm{m}$ (orange dashed) and measurements at a height of 1.2 m at the ECT1 (blue solid line). We did not use the measurements shown in the figure for forcing. **a** and **b** show the along-stream wind speed u, **c** and **d** the vertical wind speed w, and **e** and **f** the air temperature. The left column - subfigures a, c, and e - compares time series of the respective variables. We show the corresponding Fourier spectra in the right column, subfigures b, d, and f. We generated the spectra using the pre-processing steps described in Stull, 1988.

The time series of wind speed along the flow presented in Fig. 4.3 agree very well in both the absolute magnitude and the magnitude of the fluctuations. Nevertheless, a slight lag is observed between the two time series. This lag can be attributed to the setup depicted in Fig. 4.1. Data for driving the LES simulations originate from ECT2, whereas the comparison data are obtained from ECT1 approximately 10 m upwind of ECT2. Consequently, the simulation exhibits a lag relative to the measurements. Nonetheless, the good agreement between measurement and simulation is also reflected by the spectra in Fig. 4.3b. Both measurement and simulation agree well on all time scales. Time series and spectra indicate that the LES simulation features a realistic along-stream wind speed.

Furthermore, the mean vertical wind speed of the LES simulation at the extracted point $\overline{w_{LES}} = 0.011\,\mathrm{m\,s^{-1}}$ is in good agreement with the double-rotated measurement data (and thus $\overline{w_{EC}} \approx 0\,\mathrm{m\,s^{-1}}$). Nevertheless, the simulation underestimates the magnitude of the fluctuations. While EC measurements yield a variance of $\sigma^2_{w,EC} = 7.9 \times 10^{-2}\,\mathrm{m^2\,s^{-2}}$, the simulation shows a variance of $\sigma^2_{w,LES} = 7.0 \times 10^{-3}\,\mathrm{m^2\,s^{-2}}$. Both variances differ by a factor of 11. This mismatch in the magnitude of the fluctuations is evident from the spectrum depicted in Fig. 4.3d. The simulation notably lacks spectral energy density across all frequencies, with the discrepancy becoming more pronounced for $f > 1\,\mathrm{Hz}$. Sensitivity analysis unveiled multiple potential factors contributing to this discrepancy, some of which are interrelated. Specifically, the analysis suggests that grid spacing is critical in accurately representing vertical wind speeds. Conversely, the impact of employing a more sophisticated Sub-Grid-Scale (SGS) model, such as a dynamic Lagrangian SGS model, was relatively small. The gap for high-frequency data and the dependence on the grid spacing indicates that relevant eddy sizes in this strongly heterogeneous setting might even be smaller than the chosen grid spacing of 4 cm (horizontal) and 3 cm-7 cm (vertical). We think there are multiple reasons for these not-captured small-scale eddies. One such factor is the presence of sharp terrain features that remain unresolved by the simulation. In addressing this issue, it was important to add resolved surface roughness. Surface roughness proved crucial, demonstrating a comparable impact to increasing grid resolution (not shown). Furthermore, the model does not account for small-scale heterogeneities in the surface temperature of bare ground driving smaller-scale (and thus higher frequency) buoyant motion. Another contributing factor could be an inadequate description of inflow conditions. The model is forced by a logarithmic wind profile scaled by a single measurement, which may not adequately capture disturbances in the inflow, such as low-level jets. Finally, the dimensions of the model domain itself influence the flow by constraining the scale of motions within the simulation. Our sensitivity analysis indicates that state-of-the-art SGS models struggle to parameterize these intricate effects. Future work should prioritize efforts to address and improve upon these limitations. However, it is important to note that for our present study, further reduction of grid spacing was unfeasible due to constraints imposed by limited computational resources.

For the comparison of air temperature in Fig. 4.3e, we corrected the measured sonic temperature with the simultaneously measured humidity according to Schotanus et al., 1983. The spectra presented in Fig. 4.3f indicate a similar mismatch between the EC measurement and the simulation for $f > 1\,\mathrm{Hz}$. However, for lower frequencies, both spectra match well. This is also reflected by the time series shown in Fig. 4.3e. The magnitude of the fluctuations seems very similar to the EC data. Not visible from the spectrum, there is a positive temperature bias of $\approx 1\,^{\circ}\mathrm{C}$ of the air temperature extracted from the simulation. Different footprints can explain this bias. The mean temperature used for forcing was recorded at the height of 3.7 m at the AWS (cf. Fig 4.1). In contrast, the data shown as the blue curve in Fig. 4.3e was measured at ECT1.

In summary, the LES simulation demonstrates remarkable capability in replicating the observed horizontal wind speed pattern as measured by a high-frequency EC sensor. Moreover, the mean vertical wind speed and the air temperature fluctuations agree well with the measurements. However, for frequencies exceeding $f > 1\,\mathrm{Hz}$, the simulation tends to underestimate the spectral energy densities for w and T. We explain this discrepancy with the strongly heterogeneous nature of the setting, which can not be fully represented in fine detail by the model. Despite this limitation, we maintain that the LES simulation yields realistic results suitable for subsequent analysis.

4.4 Characterization of Near-Surface Boundary Layer Dynamics

4.4.1 Intermittent Advection

In the following section, we aim to compare the LES simulation results with data obtained from the IR screen setup as described in Haugeneder et al., 2023. Our objective is to demonstrate the model's capability to resolve the dynamics of the near-surface boundary layer accurately. In (Haugeneder et al., 2024), the authors describe the intermittent advection of warm air plumes from bare ground over snow, a phenomenon successfully captured using the IR screen setup. We extracted a two-dimensional slice perpendicular to the cross-flow direction from the simulation data to facilitate comparison with our simulations. This slice then shows an aerial overview of the near-surface boundary layer similar to the IR screen data.

We compare snapshots from the IR screen data (Figs. 4.4 b and d) with snapshots from the slice of the LES simulation (Figs. 4.4 c and e) in Fig. 4.4. Furthermore, the video in the Supplementary Materials visualizes the temporal dynamics. For a better understanding of the processes discussed in the following, we strongly encourage the reader to watch it. In the second row, Figs. 4.4b and c, we show a snapshot taken when a plume of warm air was advected over the snow patch. In both, measurement and simulation data, the air temperature is the highest directly adjacent to the bare surface. The plume of warm air reaches up to $\approx 1\,\mathrm{m}$ above the surface at $x = 0\,\mathrm{m}$. In the measurement, the warm air reaches a few meters along the wind direction over the snow surface. For $x > 1\,\mathrm{m}$ we detected a shallow layer of cold air close to the snow surface. Further down wind, this layer grows up to 0.5 m depth. The slice of the LES simulation shows a very similar pattern: The plume of warm air reaches $x \approx 2\,\mathrm{m}$. Similar to the measurement, a layer of cold air is adjacent to the snow surface. The layer seems to be slightly thicker than the measurement for fetch distances $x < 2\,\mathrm{m}$. At $x = 3\,\mathrm{m}$ it grows as observed from the IR screen measurements. The plume of warm air displaces the cold air layer from left to right.

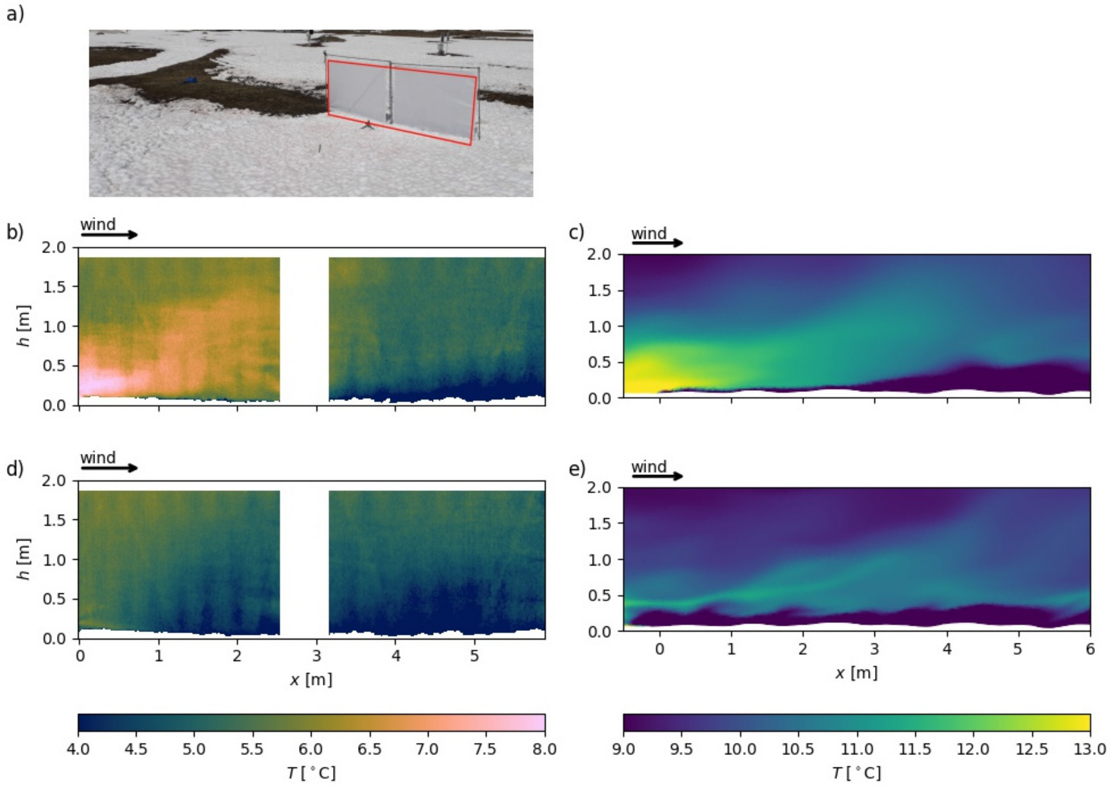

Figure 4.4: Comparisons of snapshots from measurements using the IR screen setup (Haugeneder et al., 2023) with snapshots from the LES simulations visualizing intermittent advection. The data show along-wind slices through the near-surface boundary layer. The picture in **a** depicts the experimental setup for the IR screen method, and the red frame indicates the excerpt shown in **b** and **d**. **c** and **e** depict LES data. The wind blows from left to right across the bare ground - snow transition which is at $x = 0\,\mathrm{m}$. The surface appears as the white area at the bottom of the frames. b and c show the intermittent advection of a plume of warm air, while d and e depict a calmer period.

In the simulation, the layer of cold air adjacent to the snow surface appears to be more clearly separated from the air above. This is especially obvious from the videos in the Supplementary. You can see that in the simulation, the wind influences the growth of this layer. However, especially at the leading edge of the snow patch, the depth does not change as much over time as expected from the measurements. This could be explained by vertical wind speeds that are too low and, thus, insufficient vertical mixing. We found from previous simulation runs that the vertical wind speed is an important factor in determining the thickness of the cold air layer in the simulation results. With an underestimated vertical wind speed, there is insufficient vertical mixing to develop a deeper layer of cold air. With a finer grid, we could increase the vertical wind speeds near the surface. However, the fluctuations are still too low as the reader can also see from the comparison in Fig. 4.3c at 1.2 m above the surface.

Just a few seconds after the advection of the warm air plume, the boundary layer near the surface was distinctly colder, as shown in Figs. 4.4d and e. In the measurement, the layer of cold air adjacent to the snow surface was deeper. Air is significantly colder than in Fig. 4.4c, but some slightly warmer plumes as remnants of a previously advected plume detached from the surface, are visible. A deeper layer of decoupled cold air adjacent to the snow surface develops at the leading edge of the snow patch during more quiescent conditions. The cold air even spreads over bare ground because rising buoyant plumes further to the left lead to a local back-flow close to the surface, sucking in cold air from over the snow. The short time difference between the respective two snapshots emphasizes the strong temporal heterogeneity of the near-surface boundary layer apparent in both the simulation results and the measurements. The offset in absolute temperature between the measurement and the simulation can be explained by the temperature forcing. Using air temperatures measured at 3.7 m above the surface at the AWS (see Fig. 4.1), we do not expect a perfect match. The focus is more on the temporal heterogeneity caused by local surface-driven buoyancy effects. Based on the comparison of time series and spectra between measurement and results, Fig. 4.4 demonstrates that our LES model setup is capable of resolving the measured pattern in the dynamics of the near-surface boundary layer above the transition from bare ground to snow. Furthermore, the above comparison shows the value of visualization using the IR screen setup.

4.4.2 Buoyancy Fluxes and Stable Internal Boundary Layer Growth

By employing EC sensors in the field, we can gather a temporal sequence of data at specific locations. However, it is difficult or even impossible to interpolate or extrapolate the data to regions without sensors spatially. Especially very close to the surface, within the lowest tens of centimeters, most traditional EC sensors do not yield reliable results. Therefore, the data obtained from the validated LES simulation presented in this study is a powerful tool for investigating spatial properties of the near-surface boundary layer. In the following, we investigate the spatial pattern of median buoyancy flux and the growth of the SIBL adjacent to the snow surface downwind of the transition from bare ground to snow.

We therefore calculate the buoyancy fluxes at every grid point of the along-wind slice taken out of the LES simulation. Figure 4.5a shows the spatial pattern. For the interpretation, the reader should keep in mind that the simulation tends to underestimate vertical wind speeds and, thus, also buoyancy fluxes. The emphasis is here on spatial patterns without claiming full quantitative accuracy. For a median SIBL depth, we take the median of the buoyancy fluxes time series at every grid point. We define the upper boundary of the SIBL by the sign change of the buoyancy fluxes. Within the SIBL, negative (downward) fluxes prevail. While above the SIBL the stratification in our setting is unstable in accordance with positive (upward) fluxes. Figure 4.5b depicts the diagnosed SIBL depth as a function of fetch distance over snow, x. As a fit, we apply the commonly used power law (Brutsaert, 1982a)

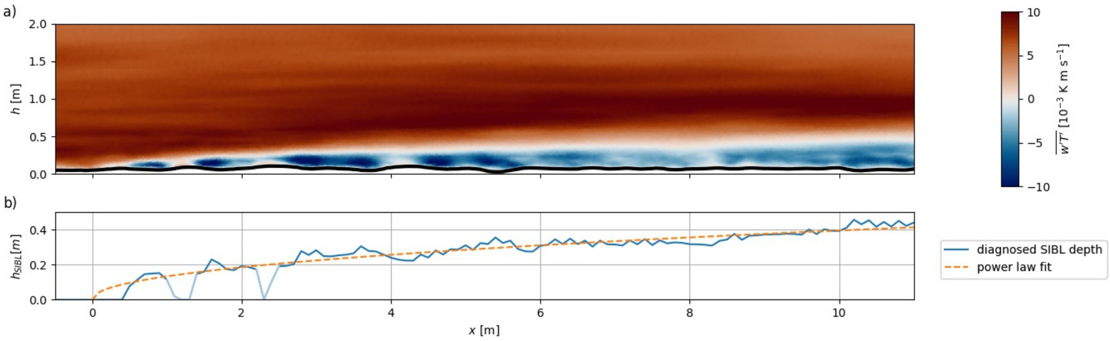

Figure 4.5: **a** Median buoyancy fluxes in an along-wind cross section through the flow. $x = 0$ marks the transition from bare ground to snow. **b** Diagnosed depth of the stable internal boundary layer adjacent to the snow surface as a function of fetch distance over snow, x. The dashed orange line indicates a power law fit (Brutsaert, 1982a). The two blurred gaps at $x = 1.5\,\mathrm{m}$ and at $x = 2.3\,\mathrm{m}$ where excluded from the fit, since the very shallow SIBL there was disturbed by the topography (see text for more details).

$$h_{SIBL} = c\left(\frac{x}{1\,\mathrm{m}}\right)^{b}. \tag{4.6}$$

We exclude the two drops in the diagnosed SIBL height around $x = 1.2\,\mathrm{m}$ and $x = 2.3\,\mathrm{m}$, because at these positions, the shallow SIBL is disturbed by the local topography. We discuss this effect in the following passage. The parameters obtained from the least squares fit are

$$b = 0.47 \tag{4.7}$$

$$c = 0.13\,\mathrm{m}. \tag{4.8}$$

Two different regimes immediately become obvious from Fig. 4.5a. Negative (downward) buoyancy fluxes prevail close to the snow surface. In contrast, the rest of the domain exclusively exhibits positive fluxes. The air heats up over bare ground and is then intermittently advected over the snow surface. Along the trajectory of the plumes, we detect the maximum positive buoyancy fluxes, because warm plumes ($T' > 0$) raise due to buoyancy ($w' > 0$). Above $h = 1.5\,\mathrm{m}$ the influence of surface-driven warm air advection decreases and the positive buoyancy fluxes are weaker which indicates the blending height. Above this height, flux differences can not be clearly attributed to the surface heterogeneities anymore but are already sufficiently mixed by the ambient flow. Close to the snow surface, we see an effect of the artificial topography on the buoyancy fluxes. On the downwind side of the local terrain height maxima, pronounced negative fluxes develop. The small regions just upwind of these maxima exhibit at least zero or slightly positive fluxes. These differences can be driven by warm air sweeps. When a wind gust advects warm air near the snow surface, the flow follows the local topography. On the upwind side of local terrain maxima $w' > 0$ and $T' > 0 \rightarrow w'T' > 0$, while behind the maxima $w' < 0$ and $T' > 0 \rightarrow w'T' < 0$. The maximum negative values of the buoyancy fluxes occur around the upper boundary of the cold air layer visible in Fig. 4.4c, e. The cold air layer grows with low wind speeds until a wind gust replaces it with warmer air. These sweep events lead to pronounced negative buoyancy fluxes. Further downwind ($x > 6\,\mathrm{m}$), the cold layer close to the surface is already deep enough that the sweeps cannot reach down to the surface anymore. Additionally, the air, initially heated up over bare ground, has already cooled down so that the temperature heterogeneities are not as pronounced as for smaller fetch distances over snow. The resulting increased energy input at the leading edge of the snow patch leads to accelerated melt described in previous experimental studies (Mott et al., 2011; Schlögl et al., 2018a).

The SIBL depth depicted in Fig. 4.5b can be nicely described by the fit reviewed in Brutsaert, 1982a. At the very leading edge ($x < 0.4\,\mathrm{m}$) the grid spacing in the LES simulation seems to be too small to properly resolve the SIBL. However, the fit parameter (4.7), determining the growth rate does deviate from previously found values for step changes in surface roughness. Elliott, 1958 and Bradley, 1968 (as reviewed by Brutsaert, 1982a) report typical values for neutral conditions of $b = 0.7 - 0.8$. More recently Granger et al., 2006 also investigated the SIBL growth adjacent to snow downwind of a transition from bare ground to snow. Depending on the roughness of the surface in the upwind direction, they found values of $b = 0.5 - 0.62$ and $c = 0.18 - 0.64$, which is just larger than the values of our fitting parameters. However, Granger et al., 2006 compared air temperature upwind and downwind of the transition to diagnose the SIBL depth. They defined the upper SIBL boundary as the height above which both profiles overlap, which is higher than the depth of the (statically) stable layer. Consequently, we expect shallower SIBLs with our definition. In fact, Granger et al., 2006 report SIBL depths according to their best fits of $h_{SIBL,Granger2006} \approx 0.3\,\mathrm{m} - 0.9\,\mathrm{m}$ at a fetch distance over snow of $x = 2\,\mathrm{m}$, whereas our best-fit power law only yields a SIBL depth of $h_{SIBL} = 0.18\,\mathrm{m}$. With the same temperature profile modification approach to estimate the SIBL depth, Takahara and Higuchi, 1985a also suggest slightly deeper SIBLs.

4.4.3 Near-Surface Boundary Layer For Low and High Wind Speeds

The results of the LES simulation are well suited to study not only the median flow properties but also the influence of the ambient wind speed on the near-surface boundary layer. In the following, we examine how the near-surface boundary layer changes during periods of low and high wind speeds. We therefore filter the data using the wind speed at $x = 0\,\mathrm{m}$, $y = 3.0\,\mathrm{m}$, and $h = 1.5\,\mathrm{m}$ after calculating all fluxes. The low wind speed class comprises periods with the 20% lowest wind speeds. (≤ 20%-quantile). We denote this class by "$u \leq u_{0.2}$". On the contrary,

the high wind speed class contains the 20% highest wind speeds (≥ 80%-quantile). This class is abbreviated by "$u \geq u_{0.8}$". Therefore, both classes contain the equivalent of 1 min data.
Figure 4.6 compares vertical profiles for both classes. The temperature profiles in Figs. 4.6a and b show a growing depth of the statically stable layer close to the surface with fetch distance. Furthermore, a dependency of its depth on the wind speed is apparent. Higher wind speeds coincide with shallower statically stable layers. For example, the depth difference at $x = 2\,\mathrm{m}$ between the two wind speed classes is $\Delta h_{ssl,x=2m} = 0.09\,\mathrm{m}$ and at $x = 10.5\,\mathrm{m}$ $\Delta h_{ssl,x=10.5m} = 0.30\,\mathrm{m}$. During periods of low wind, a deeper layer over snow can cool down. In contrast, the high wind speeds intermittently advect warm air from over bare ground limiting the depth of the statically stable layer. The buoyancy fluxes presented in Figs. 4.6c and d support this observation. The layer of negative buoyancy fluxes in line with statically stable conditions close to the snow surface is deeper for low wind speeds. Furthermore, during calm periods the median and the 25%-quantile of the buoyancy fluxes, especially at the leading edge of the snow patch ($x = 0.5\,\mathrm{m}$ and $x = 2\,\mathrm{m}$) indicate slightly stronger negative fluxes. The energy from cooling the near-surface air during calm periods is transferred to the snow surface. When the snow is already at 0 °C, the additional energy is available for melt.
Layers of different stability also leave their footprints in the profiles of the horizontal wind speed shown in Figs. 4.6e and f. During the quiescent periods the profile at $x = 10.5\,\mathrm{m}$ shows a kink at the upper boundary of the SIBL. With high wind speeds, the flow accelerates above the SIBL and forms a jet. The decoupled stable layer adjacent to the surface seems to act like a nozzle to the flow aloft. The effect is similar to the speed up of wind above ridge crests at larger scales such as demonstrated in Reynolds et al., 2023.

To further study the heat transfer, especially close to the surface, where reliable measurements are challenging, Fig. 4.7 shows buoyancy fluxes and diagnosed SIBL depths for low and high wind speeds. The setup for each wind speed class is similar to Fig. 4.5. In line with the discussion of the profiles above, we can directly see that the layer of negative fluxes adjacent to the snow surface, the SIBL, is deeper for low wind speeds. The power-law fit yields a SIBL depth at $x = 10\,\mathrm{m}$ of $h_{SIBL,u \leq u_{0.2}} = 0.41\,\mathrm{m}$ for low wind speeds and $h_{SIBL,u \geq u_{0.8}} = 0.32\,\mathrm{m}$ for high wind speeds. Shallower SIBLs with higher wind speeds are in contrast to the findings of Mott et al., 2013. Analyzing field data, they associate deep SIBLs with high wind speeds through enhanced generation of shear turbulence. Also, Granger et al., 2006 investigated the SIBL growth in dependency of the Weisman horizontal stability parameter (Weisman, 1977). Their Fig. 8 indicates, that with increased shear, i.e. generated by higher wind speed, shallower SIBLs develop, which is in accordance with our findings.
We see from Fig. 4.7 that the buoyancy fluxes within the SIBL are spatially heterogeneous. There are regions with pronounced negative buoyancy fluxes next to regions with positive fluxes. Especially during periods of high wind speeds (Fig. 4.7d), sharp transitions between these regions of fluxes with opposite signs are apparent. This horizontal flux divergence seems to be driven by an interplay of the local wind field with the topography. It points to the fact that the SIBL, and the atmospheric layer adjacent to the snow patch generally, is spatio-temporally highly heterogeneous.

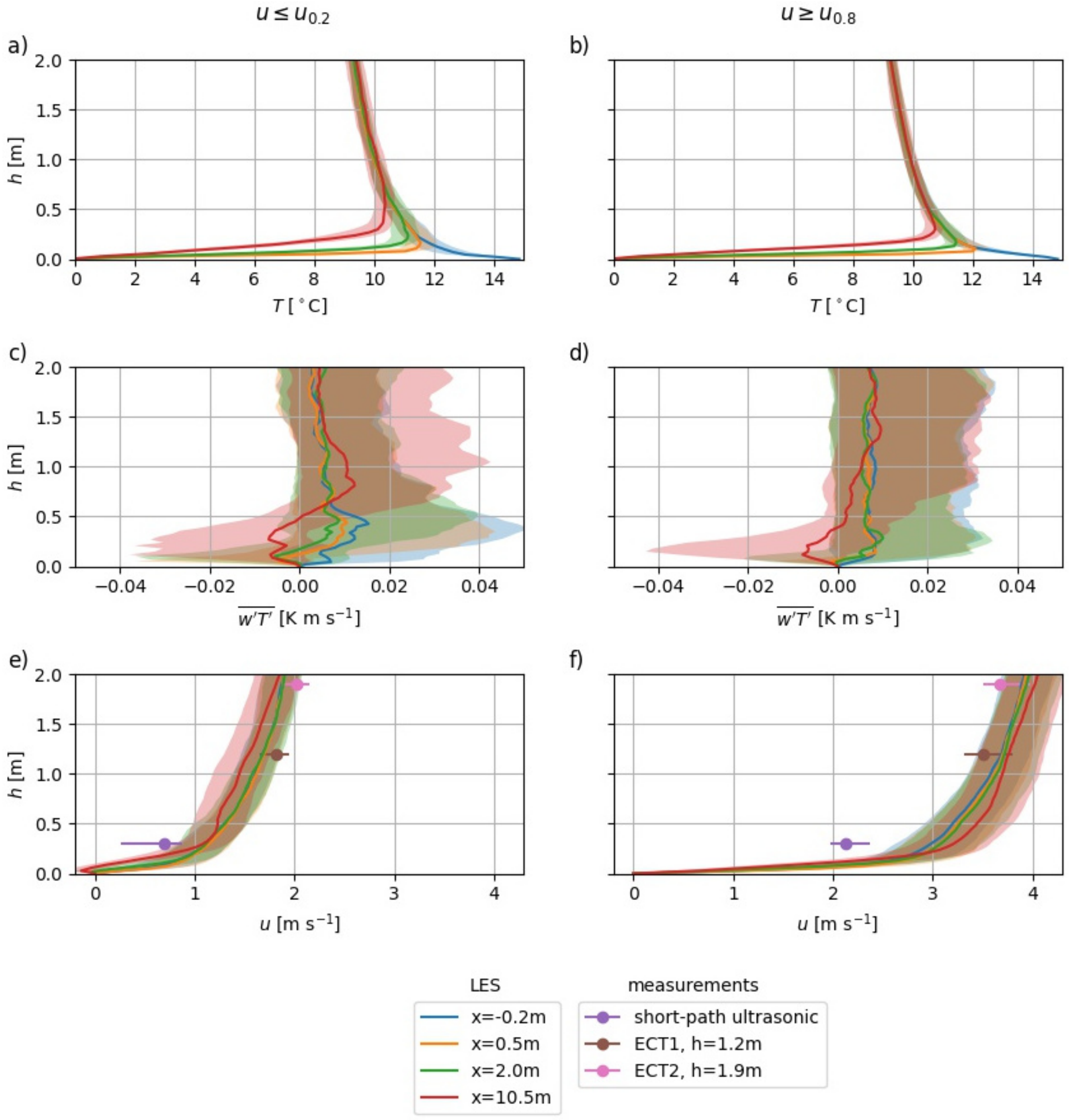

Figure 4.6: Vertical profiles for two wind speed classes: The left column (a, c, e, g, i) contains data with the horizontal wind speed u below or equal to the 20%-quantile, the right column (b,d,f,h,j) data with u larger or equal to the 80%-quantile. **a** and **b** show profiles of the horizontal wind speed u, **c** and **d** of the vertical wind speed w, **e** and **f** of the air temperature T, **g** and **h** of the buoyancy flux $\overline{w'T'}$, and **i** and **j** of the turbulence kinetic energy e. The solid lines indicate the median and the shaded regions the interquartile range (25% - 75%). We classified the data according to the wind speed after calculating the fluxes.

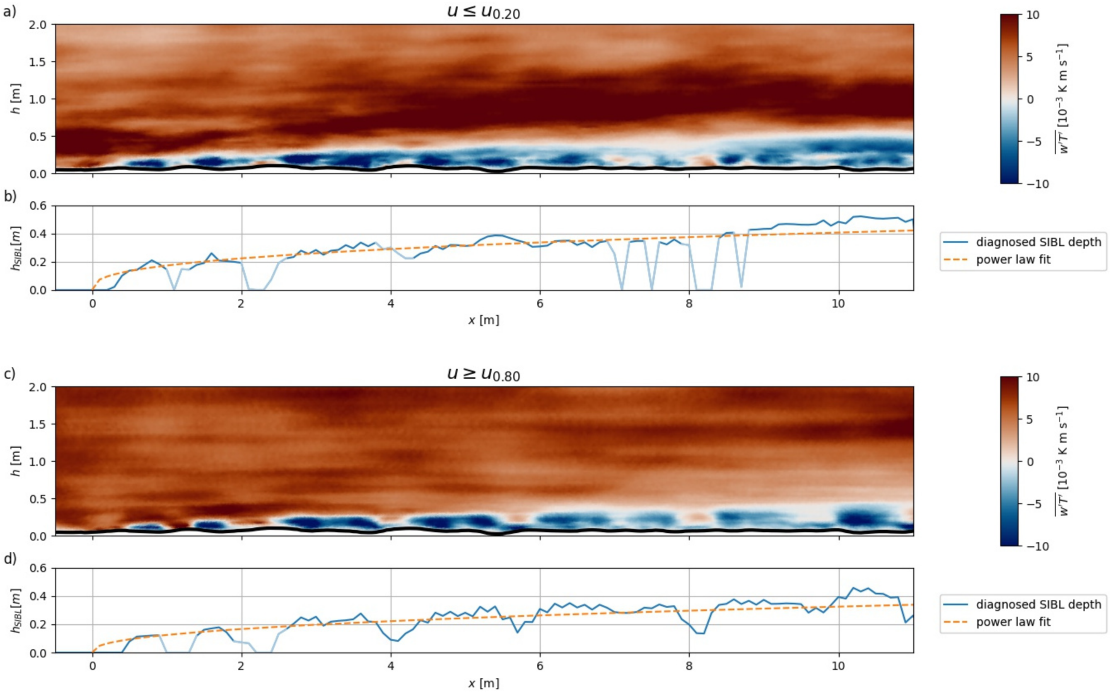

Figure 4.7: **a** Median buoyancy flux for the 20% lowest wind speeds and **b** the SIBL depth diagnosed from it together with a fit of (4.6). **c** Median buoyancy flux for the 80% highest wind speeds and **d** the SIBL depth diagnosed from it with a fit of (4.6). We neglected the blurred parts of the diagnosed SIBL depth similar to Fig. 4.5.

4.5 Conclusions, Limitations, and Outlook

In the present study, we set up a centimeter-resolution large eddy simulation to model the near-surface atmospheric flow across an idealized transition from bare ground to snow. We force the inflow-outflow model with high-frequency eddy covariance data recorded during a comprehensive field campaign in patchy snow conditions. Validation with independent high-frequency data shows that the model can reasonably reproduce horizontal wind speed and energy density spectra. However, the model lacks vertical motion and some high-frequency air temperature fluctuations as captured by the measurements. Sensitivity analysis indicates that that this disparity may stem from the cell size. Within this highly heterogeneous setting, some energy-containing eddies appear smaller than the chosen horizontal grid spacing of 4 cm. We explain this for the following reasons: (1) artificially smoothed surface, (2) insufficient inflow description and (3) restriction of large-scale motions through the model domain dimensions. As our sensitivity analyses indicate, even state-of-the-art subgrid-scale models cannot adequately parameterize these effects on the centimeter scale. Nevertheless, the model adeptly reproduces flow features observed using measurements with a thermal infrared camera pointing at vertically deployed thin synthetic screens. It accurately depicts buoyant plumes of warm air intermittently detaching from the bare ground and being transported over the snow surface. This process is highly dynamic with time scales of only a few seconds.
Furthermore, the simulation results enable us to investigate the growth of a thermal stable internal boundary layer (SIBL) adjacent to the snow surface. We show that the upper boundary of the SIBL can be well described by a power law as suggested by the literature. Moreover, by distinguishing quiescent periods from periods with higher wind speeds, we can show that the wind speed influences the growth of the SIBL. A slightly deeper SIBL can develop with low wind speeds, while higher wind speeds limit its growth. The results also show that the buoyancy fluxes are spatially heterogeneous and driven by terrain roughness even within the lowest layer adjacent to the surface.

The next step towards establishing a physically grounded parameterization of atmospheric processes over highly heterogeneous surfaces entails utilizing actual snow cover distributions as a lower boundary condition. Together with an extended domain size, this helps to quantify the energy exchange between snow and atmosphere on a larger scale spanning tens to hundreds of meters. These scales align with those typically employed in state-of-the-art regional-scale numerical weather models, enabling direct comparisons between the two modeling estimates. The obtained results may be relevant not only for snow hydrological modeling but also for enhancing the performance of atmospheric models.

Conflict of Interest Statement

The authors declare that the research was conducted in the absence of any commercial or financial relationships that could be construed as a potential conflict of interest.

Author Contributions

MH set up the model with close help of OH and MJ under the guidance of ML and RM. The research was conducted with regular discussions among all coauthors. MH prepared the manuscript with the contributions of RM. All coauthors gave feedback on the draft and helped improving the manuscript.

Funding

This work is funded by the Swiss National Science Foundation (SNF) project 'Snow–atmosphere interactions in mountains: Assessing wind-driven coupling processes and snow-albedo-temperature feedbacks' (nr. 188554).

Acknowledgments

Our gratitude goes to Larissa Schädler for recording UAV orthophotos and assisting during the field campaign.

Data Availability Statement

The datasets for this study can be found under 10.16904/envidat.500
The source code for the analysis presented in this study is accessible under https://github.com/michhau/les_paper_24/tree/main

5 Conclusions, Limitations, and Outlook

This thesis aimed to advance our understanding of submeter-scale heat-exchange processes over patchy snow exhibiting intense surface temperature contrasts. The pronounced heterogeneity of these areas results in a highly heterogeneous and dynamic near-surface boundary layer, where multiple layers of opposing stability coexist within only a few meters of horizontal distance. Conventional eddy covariance (EC) measurements allow insight into the temporal variations of such layers at a fixed location. However, recognizing the need for a broader perspective, we have developed a novel approach. Our new method not only allows us to extract spatially distributed insights into the dynamic patterns of air temperature over diverse land surfaces, but also enhances our comprehension of the intricate interplay between near-surface turbulent exchanges driven by the surface and larger-scale flows. By combining various measurement techniques and Large Eddy Simulations (LES), we delve deeper into understanding the underlying processes governing these phenomena, thereby advancing our knowledge of the complex atmospheric dynamics above a patchy snow cover.

Extending Point Measurements to Two Dimensions

To gain two-dimensional information on air temperature dynamics at high spatial and temporal resolution, we adapted a method initially proposed by Grudzielanek and Cermak, 2015a. With this method, we can extract spatially continuous profiles of air temperatures in two dimensions. Moreover, the resulting videos directly visualize the near-surface boundary-layer dynamics adjacent to the surface, an area inaccessible to conventional EC sensors. These visual representations help to understand the spatio-temporal heterogeneity and eddy dynamics of the atmospheric layer adjacent to the surface.

Subsequently, we developed an innovative algorithm capable of estimating two-dimensional wind speeds by tracking the pattern of air temperatures. The WEIRD algorithm allows unprecedented insights into the near-surface boundary layer dynamics. To validate the efficacy of WEIRD, we installed the IR screen setup amidst patchy snow during late spring of 2021 in the Dischma Valley close to Davos (Switzerland). By comparing the wind speed estimations from WEIRD with data collected by a short-path ultrasonic device placed adjacent to the screens, we could validate its accuracy. Moreover, the infrared data captured the formation and the growth of a stable internal boundary layer (SIBL) adjacent to the snow surface, providing valuable observations of this atmospheric phenomena.

The data acquired through our novel method elevate our understanding beyond conventional point-based measurements, extending insights into two dimensions. Furthermore, we tested the IR screen setup across different surfaces, including glacier ice or pure bare ground. These experiments not only prove the suitability over less heterogeneous surfaces, but also point towards future applications, which are further detailed at the end of this chapter. The IR screen setup, while highly effective, does come with a few constraints. The screen axis must be aligned with the prevailing wind direction to ensure reliable data. Our investigations revealed artificial flow disturbances for wind directions persistently deviating more than 30° from the screen axis. In our field experiments, we predominantly deployed the setup in valleys, where the topography naturally constrains the flow to prevailing wind directions. In such environments, thermally driven winds, such as valley or katabatic winds, usually exhibit a constant wind direction. This may present challenges for other topographical settings with more varying flow conditions. One challenge for the WEIRD algorithm is the low signal-to-noise ratio. When temperature differences are small, indicative of highly homogeneous atmospheric conditions, accurate wind speed estimates become difficult. Our measurements over patchy snow revealed phases where distinct patterns were scarcely visible. For such situations, the elaborate pre-processing requires tailored adjustments to address the low signal-to-noise ratio. Lastly, it is important to note that our data's exceptionally high spatio-temporal resolution necessitates coping with the challenge of producing big data. Just to provide a sense of range, 1 h of data recorded by the thermal infrared camera accumulates to approximately 100 GB of zip-compressed data. Consequently, the analysis of temperature fields has to be approached with a strategic focus, either narrowing it down to limited periods or discrete profile locations.

Understanding Near-Surface Heat Exchange Processes over Patchy Snow

In an attempt to remedy the lack of experimental data investigating the near-surface boundary layer over patchy snow, we conducted a comprehensive field campaign during spring 2021. We deployed EC sensors at multiple heights and locations in combination with measurements utilizing the IR screen setup. We focussed our analyses on the time scale of the turbulent motions. Therefore, we extended the Multi Resolution Flux Decomposition (MRD) as initially proposed by Howell and Mahrt, 1997 to yield more detailed cospectra. By applying this extended MRD to a moving window out of a 21 day long time series, we could gain information on the temporal changes of turbulence spectra. We concentrated the analyses on the buoyancy flux, temperature variance, and turbulence kinetic energy.

We could split the dataset into four different periods. During a Föhn event at the beginning, we observed pronounced shear-generated turbulence and negative (downward) buoyancy fluxes. As the first bare patches arose, warm air was advected over the leading edge of the snow patch and the depth of a stable internal boundary layer (SIBL) adjacent to the snow surface decreased. During calmer phases, the strongly stable stratification attenuated vertical motion with very low turbulence kinetic energies and concurrently increased temperature variations. We explained this using the concept of turbulence potential energy in a strongly stratified atmosphere (Zilitinkevich et al., 2007). During a second Föhn event, warm air impinged, and increased turbulence kinetic energy was in line with higher wind speeds. Finally, during the last period, the SIBL depth at the measurement location decreased below 1 m and we observed intermittent advection of warm air over the remaining snow patches. The intermittent advection left its footprints in a scale jump of the temperature variances towards scales $\mathcal{O}(10\,\mathrm{s})$. We could also observe and visualize this intermittent advection with the IR screen setup.

Analyzing the data from this campaign, we could combine conventional EC measurement with our IR screen method to thoroughly understand the near-surface boundary layer dynamics. We could show that turbulence patterns, i.e. the relevant eddy sizes do not substantially change within the first few meters above the surface. However, the buoyancy fluxes exhibit a sign change at the upper boundary of the SIBL. The SIBL depth decreased from $> 3\,\mathrm{m}$ to $< 1\,\mathrm{m}$ at the leading edge of the snow patch during the campaign. The IR screen enabled us to extend the information gained from EC point data to a two-dimensional cross section. For instance, we could visualize the intermittent advection of plumes of warm air from bare ground over the snow, leading to a pronounced temperature variance observed by the EC sensors. This highly dynamic process occurs on time scales of only a few seconds, showcasing the dynamic interplay between different surface types and their coupling to the overlying atmosphere.

Although we were able to capture turbulence data at multiple locations and heights throughout several weeks in the ablation season, this dataset is only one further piece filling the lack of experimental data. Our observations were constrained to a limited range of atmospheric conditions throughout the three-week campaign. Specifically, the analysis of the impact of up valley flows was confined to just a few days. The broader investigation of the interplay between the valley wind system and the thermal internal boundary layers was further hindered by the occurrence of two Föhn events, disrupting its typical valley wind system. However, the Föhn periods are also a valuable addition in the dataset. In general, the dependence of the near-surface heat exchange on multiple parameters such as snow cover fraction, wind direction, radiation budget, and regional wind direction inherently poses a challenge: How can we separate the influence of a single parameter without influences from others? Our approach was to split the dataset into different periods where at least some of the parameters were constant so that we could investigate the impact of the others. However, some inter-parameter dependencies remain. We, therefore, repeat the call of most of the previous studies for further experimental data covering different locations and conditions.

Numerical Model

To spatially extend point and two-dimensional measurements and gain insights into the submeter scale atmospheric processes occurring in the presence of thermal internal boundary layers forming over patchy snow covers, we employed Large-Eddy Simulation (LES) techniques. This approach allowed us to simulate atmospheric dynamics at a fine spatial resolution, providing valuable information about the intricate interactions within the near-surface boundary layer. Moreover, this approach allows to extent the range of atmospheric conditions beyond existing measurements by conducting virtual experiments. For this purpose, we set up a centimeter-scale LES over an idealized transition from bare ground to snow. We directly forced the inflow-outflow model with high-frequency EC data recorded during the field campaign described in Chapter 3, marking a novel integration of observational and modeling techniques. This allowed us to compare and validate the model results with field measurements directly. Remarkably, we observed a high level of agreement in horizontal wind speeds between the model and field data. However, vertical wind speeds were underestimated by the LES model. Further spectral analysis showed a pronounced underestimation, particularly at higher frequencies, a trend consistent with the discrepancies observed in air temperatures. Sensitivity analyzes showed that grid resolution is a crucial factor to better represent vertical motions. More sophisticated Sub-Grid-Scale (SGS) models led to only minor improvements. We attributed the mismatch to multiple factors. Insufficient inflow conditioning may have weakened turbulence and flow variations with height above the surface. Furthermore, the artificially smoothed surface did not generate enough small-scale turbulence. In addition, the model domain itself influenced the simulated flow by restricting the eddy scales. Nevertheless, we could also show by comparison to data from the IR screen that the model can reproduce observed near-surface boundary layer dynamics as the intermittent advection of plumes of warm air over snow. We showed that the SIBL growth can be well described by a power-law function of fetch distance as described in previous literature. In addition, we investigated its dependence on wind speed by separately analyzing data during low and high wind speeds. The results indicate that the SIBL grows slightly deeper for periods of weaker wind, whereas warm air sweeps limit the SIBL growth during periods with higher wind speeds. Furthermore, the results highlight the effect of the topography on the buoyancy fluxes at the surface through a locally modified flow field.

Our simulations break the path towards generalizing point-based and two-dimensional measurements to three dimensions. With the direct inflow forcing by high-frequency EC measurements, we ensure that the model closely follows the dynamics during the measurements. Additionally, the numerical model offers the possibility to conduct virtual experiments under different atmospheric conditions. However, the lack of representation of vertical motions raises the need for future research. Multiple sensitivity analyses can help reduce the mismatch step by step, addressing the abovementioned factors. Furthermore, it might be worth performing a more in-depth testing of sophisticated SGS models to find reasons for the lack of representation of small-scale motions. Available SGS models are mostly applied and tested at scales of 10 m-1000 m, but not at the centimeter scale.

Ultimately, we aim at developing a parameterization for the small-scale heat exchange processes in hectometer scale regional models such as the High-Resolution Atmospheric Research Model (HICAR) (Reynolds et al., 2023). HICAR was developed for efficient dynamic downscaling data from kilometer-scale weather models in mountainous terrain. Therefore, we must extend the LES model domain to larger areas and include a realistic snow cover distribution. A possible way would be to use the snow cover masks obtained from uncrewed aerial vehicles shown in Fig. 3.3 as a bottom temperature boundary condition and high-frequency EC measurements to force the flow at the inlet similar to the presented model. However, an extended domain requires coarser grid resolution and, thus, a reliable SGS model to parameterize smaller-scale motions. Such a setup would also allow us to focus not only on energy exchange processes at the surface but also on the coupling of the near-surface boundary layer with the overlying atmospheric boundary layer.

Further Field Data for Future Research

As part of the sublimation of snow (SOS) campaign (Lundquist et al., 2024) we had the chance to deploy the IR screen setup in autumn 2022 and spring 2023 at the Rocky Mountain Biological Laboratory near Mount Crested Butte (CO, USA). The campaign was designed to deepen our understanding and quantify the role of snow sublimation for the water resources available from snow melt. To quantify atmospheric stratification and turbulent exchange, 20 hygrothermometers and 16 EC sensors were installed on towers up to 20 m above the surface. Augmenting this instrumentation, we deployed the IR screen setup directly downwind of the towers. We captured several sequences under consistent snow coverage and numerous sequences during intermittent snow coverage, enabling a comprehensive analysis of atmospheric interactions across varying conditions. While our analysis of the recorded data remains ongoing during this thesis, the dataset presents a pathway for prospective research endeavors. Leveraging data from the towers enables us to quantify larger submeso-scale motions, offering insights that can be connected with the small-scale dynamics in the layer adjacent to the surface as observed with the IR screen setup. This dataset can help to investigate the complex interaction of motions at different scales in future research.

In summer 2023, we actively participated in the Hintereisferner Experiment (HEFEX2) on the Hintereisferner glacier in Austria. The comprehensive campaign featured an array of various atmospheric measurements aimed at investigating the influence of a glacier atmosphere on the energy and mass balance of the glacier surface. Notably, shallow katabatic winds significantly cool the near-surface atmosphere, resulting in decoupling from the overlying warmer atmosphere (Grachev et al., 2016; Mott et al., 2020). The katabatic jet, often just a few meters thick, is subject to various influencing factors, including ambient stratification and synoptic scale flow dynamics. The IR screen data helps to understand glacier flow dynamics and its effects on the glacier microclimate. By observing the intricate heat exchange processes between the glacier and the overlying atmosphere, our findings contribute to a deeper understanding

of glacier-atmosphere interactions.
Although a detailed analysis of these datasets will be the subject of future research, the scientific collaborations have provided an opportunity to put the IR screen setup to the test across diverse environmental conditions. This testing encompassed not only strongly heterogeneous surfaces such as patchy snow but also more homogeneous settings over a continuous snow cover or glacier ice. The preliminary analysis indicates that the temperature fields are less spatio-temporally heterogeneous, yet intriguing dynamic features are still visible, underscoring the versatility and efficacy of the IR screen setup across a wide range of situations and research questions.

In summary, the novel experimental method presented in this work allows us to extend information gained from point-based measurements to two dimensions and visualize the near-surface boundary-layer dynamics. Measurements in the context of other experimental campaigns also suggest the applicability over surfaces exhibiting less heterogeneity as continuous snow covers or on glaciers. Combining the IR screen method with conventional EC measurements, we investigate interacting motions at different scales from large scale synoptic flow to small turbulent eddies close to the surface. With this we improve the understanding of sub-meter scale heat exchange processes over patchy snow. By setting up a centimeter scale LES, we make the first step towards including the observed processes in hectometer-scale atmospheric models.

A Supplementary Material for Chapter 2

A.1 Spectral Density

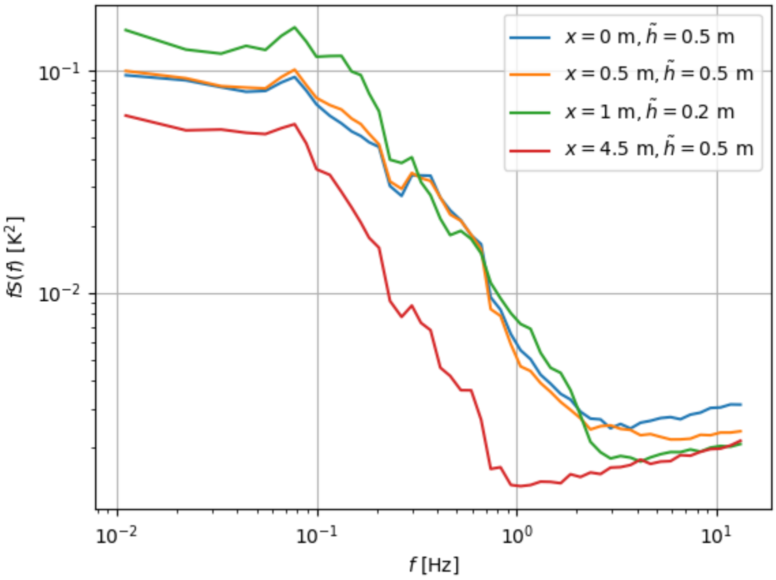

Figure A.1: Spectral density of the screen temperature time series for four different pixels. The height above snow, $\tilde{h}$, and the fetch distance x are given for the four pixels

A.2 Real Time Near-Surface Atmosphere Dynamics (Video)

A 1 min excerpt from the recorded infrared sequence (28 April 2021 1200 LT) in real time is uploaded separately. The video shows the advection of warm air plumes over the snow surface and the strong spatio-temporal dynamics of the near-surface atmospheric layer over patchy snow cover. The field of view is the same as in Fig. 2.4.

B Supplementary Material for Chapter 3

B.1 Spectra For All Sensors

B.2 Föhn Diagnosis

To diagnose Föhn conditions during our observation period, we applied the mixture model from Plavcan et al., 2014. The model performs an unsupervised classification based on measured variables. In our case, we used the wind speed measured at the AWS as the primary classifier. Additionally, we took the potential temperature difference between the ridge station (see Fig. 3.1 for the location) and the AWS, the relative humidity measured at the AWS, and the wind direction at the AWS as concomitant classifiers. We used the foehnix-python package available on github (https://github.com/matthiasdusch/foehnix-python, accessed on 26 November 2023). Before applying the model, we filtered the AWS data and the data from the Grialetsch ridge station according to the prevailing wind directions. Only wind directions from the southern sector were selected as candidates for potential Föhn events.

The probability panel shows that there was a Föhn event from the begin of the campaign (21 May to 24 May 1400 LT interrupted by two phases without Föhn. The model also classifies the period from 25 May 1800 LT to 26 May 1500 LT as Föhn. However, due to lack of power, the sensors at the ECT did not record data during this period and EC data cannot be analyzed. The following days are mostly recognized as non-Föhn days with short phases of increased probability of Föhn. Later, the period from 1 June 0000 LT to 5 June 1500 LT is dominated by Föhn with disruptions. Towards the end of the observation period, the model only classified short periods as Föhn. To sum up, for the analysis of the data in the present study the identified Föhn periods are

- 21 May 0000 LT to 25 May 1800 LT, interrupted twice
- 1 June 0000 LT to 5 June 1500 LT, high Föhn probability with disruptions

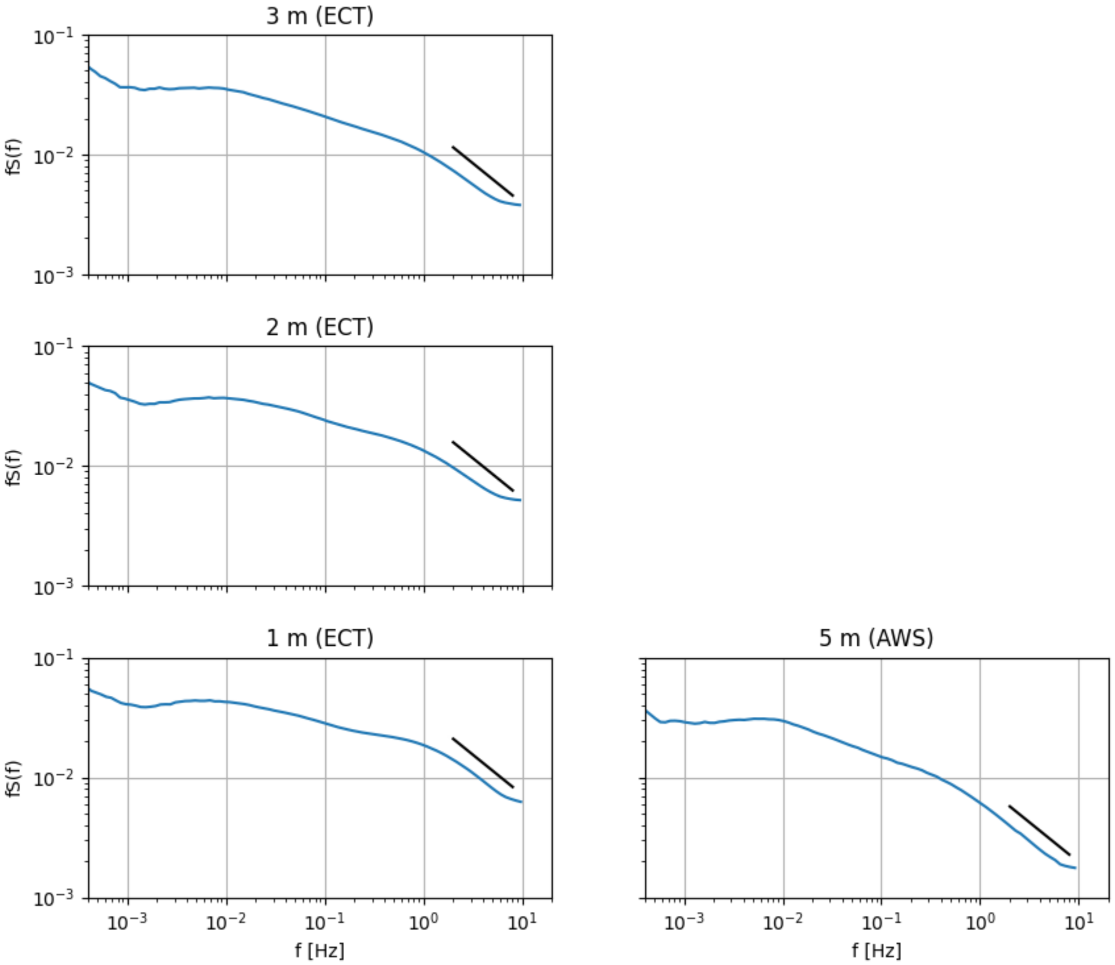

Figure B.1: Fourier-decomposed spectra of the sonic temperature T_s for all EC sensors over the whole observation period from 21 May to 11 June. The black lines indicate the theoretical $-\frac{2}{3}$ slope expected for the inertial subrange. An agreement indicates that the recorded data are trustworthy.

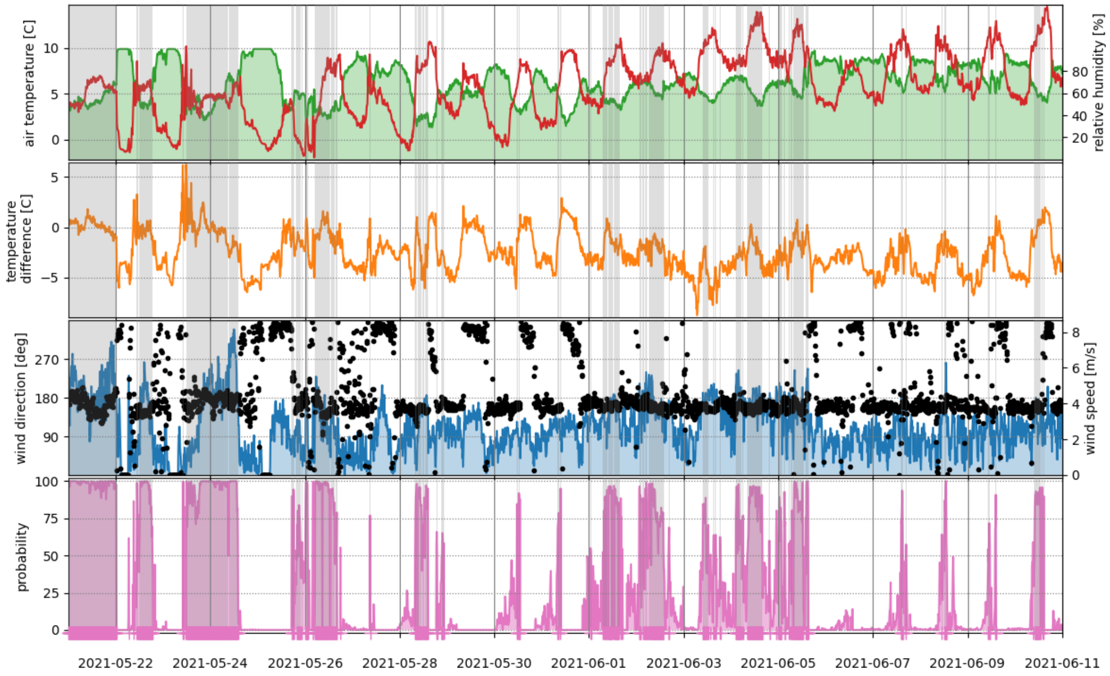

Figure B.2: Föhn diagnosis created with the foehnix-python package using the mixture model from Plavcan et al., 2014. The top panel shows the air temperature (red, left y-axis) and relative humidity (green, right y-axis) recorded at the AWS. The panel below depicts the potential temperature difference between the ridge station at Piz Grialetsch (see Fig. 3.1 for the location) and the AWS at Dürrboden. The next panel indicates the wind direction (black dots, left y-axis) and the wind speed (blue curve, right y-axis) at the AWS. The bottom panel displays the probability of Föhn according to the mixture model.

B.3 Multi-Resolution Flux Decomposition For All EC Sensors

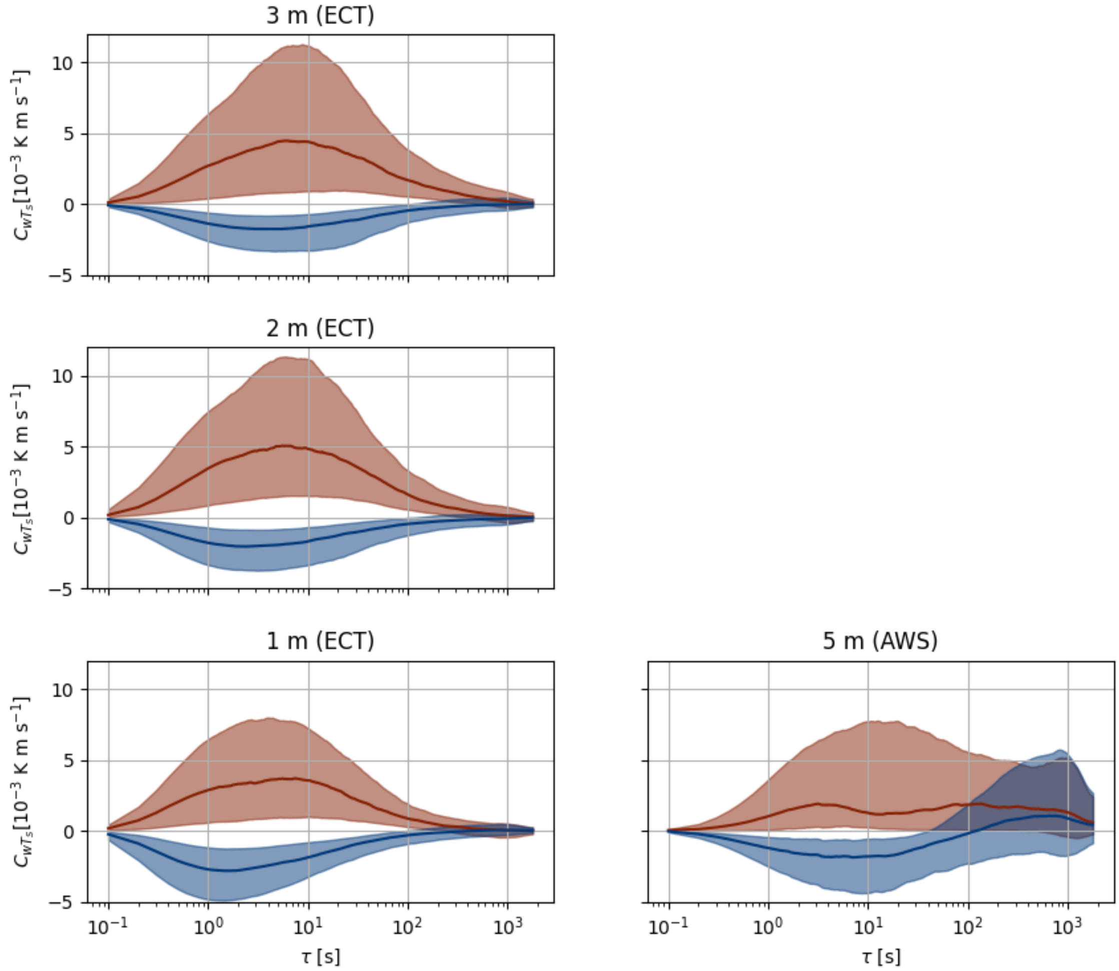

Figure B.3: Multi-Resolution Flux Decompositions for all EC sensors installed at Dürrboden during the observation period from 21 May to 11 June. The red curves correspond to unstable conditions, while the blue curves correspond to stable conditions.

B.4 Real Time Near-Surface Atmosphere Dynamics (Video)

An excerpt from a recorded thermal infrared sequence (31 May 2021 1445 LT) in real time is uploaded separately. Two thin, synthetic screens are deployed vertically across the transition from bare to snow. The screen's surface temperature serves as a proxy for the local air temperature (indicated by the colours) (Haugeneder et al., 2023). In the video, the up valley wind blows from left to right. The x-axis denotes the wind fetch distance over snow x, while the y-axis shows the height h above the bottom of the frame. The snow surface is shown in white.

The video visualizes the interaction between advected plumes of warm air and the stable internal boundary layer development over the snow surface in real time. The field of view is the same as in Fig. 3.9.

Bibliography

Aubinet, M., Vesala, T., & Papale, D. (Eds.). (2012). *Eddy covariance. a practical guide to measurement and data analysis*. Springer Netherlands.

Balogh, M., Parente, A., & Benocci, C. (2012). Rans simulation of abl flow over complex terrains applying an enhanced k-ϵ model and wall function formulation: implementation and comparison for fluent and openfoam. *Journal of Wind Engineering and Industrial Aerodynamics*, *104-106*, 360–368. https://doi.org/10.1016/j.jweia.2012.02.023

Bavay, M., Lehning, M., Jonas, T., & Löwe, H. (2009). Simulations of future snow cover and discharge in alpine headwater catchments. *Hydrological Processes*, *23*, 95–108. https://doi.org/10.1002/hyp.7195

Beniston, M., Farinotti, D., Stoffel, M., Andreassen, L. M., Coppola, E., Eckert, N., Fantini, A., Giacona, F., Hauck, C., Huss, M., Huwald, H., Lehning, M., López-Moreno, J.-I., Magnusson, J., Marty, C., Morán-Tejéda, E., Morin, S., Naaim, M., Provenzale, A., ... Vincent, C. (2018). The european mountain cryosphere: a review of its current state, trends, and future challenges. *The Cryosphere*, *12*, 759–794.

Bezanson, J., Edelman, A., Karpinski, S., & Shah, V. B. (2017). Julia: a fresh approach to numerical computing. *SIAM Review*, *59*, 65–98.

Bradley, E. F. (1968). A micrometeorological study of velocity profiles and surface drag in the region modified by a change in surface roughness. *Quarterly Journal of the Royal Meteorological Society*, *94*, 361–379. https://doi.org/10.1002/qj.49709440111

Brauchli, T., Trujillo, E., Huwald, H., & Lehning, M. (2017). Influence of slope-scale snowmelt on catchment response simulated with the <i>alpine3d</i> model. *Water Resources Research*, *53*, 10723–10739. https://doi.org/10.1002/2017WR021278

Brock, B. W., Mihalcea, C., Kirkbride, M. P., Diolaiuti, G., Cutler, M. E. J., & Smiraglia, C. (2010). Meteorology and surface energy fluxes in the 2005–2007 ablation seasons at the miage debris-covered glacier, mont blanc massif, italian alps. *Journal of Geophysical Research*, *115*, D09106.

Brutsaert, W. (1982a). *Evaporation into the atmosphere*. Springer Netherlands. https://doi.org/10.1007/978-94-017-1497-6

Brutsaert, W. (1982b). *Evaporation into the atmosphere*. Springer Netherlands.

Carletti, F., Michel, A., Casale, F., Burri, A., Bocchiola, D., Bavay, M., & Lehning, M. (2022). A comparison of hydrological models with different level of complexity in alpine regions in the context of climate change. *Hydrology and Earth System Sciences*, *26*, 3447–3475. https://doi.org/10.5194/hess-26-3447-2022

Chapin, F. S., Sturm, M., Serreze, M. C., McFadden, J. P., Key, J. R., Lloyd, A. H., McGuire, A. D., Rupp, T. S., Lynch, A. H., Schimel, J. P., Beringer, J., Chapman, W. L., Epstein, H. E., Euskirchen, E. S., Hinzman, L. D., Jia, G., Ping, C.-L., Tape, K. D., Thompson, C. D. C., . . . Welker, J. M. (2005). Role of land-surface changes in arctic summer warming. *Science*, *310*, 657–660.

Clark, M. P., Hendrikx, J., Slater, A. G., Kavetski, D., Anderson, B., Cullen, N. J., Kerr, T., Hreinsson, E. Ö., & Woods, R. A. (2011). Representing spatial variability of snow water equivalent in hydrologic and land-surface models: a review. *Water Resources Research*, *47*. https://doi.org/10.1029/2011WR010745

Cohen, J., & Rind, D. (1991). The effect of snow cover on the climate. *Journal of Climate*, *4*, 689–706.

Colle, B. A., Smith, R. B., & Wesley, D. A. (2013). Theory, observations, and predictions of orographic precipitation. https://doi.org/10.1007/978-94-007-4098-3_6

Crameri, F., Shephard, G. E., & Heron, P. J. (2020). The misuse of colour in science communication. *Nature Communications*, *11*, 5444. https://doi.org/10.1038/s41467-020-19160-7

Deardorff, J. W. (1974). Three-dimensional numerical study of the height and mean structure of a heated planetary boundary layer. *Boundary-Layer Meteorology*, *7*, 81–106. https://doi.org/10.1007/BF00224974

Deems, J. S., Fassnacht, S. R., & Elder, K. J. (2006). Fractal distribution of snow depth from lidar data. *Journal of Hydrometeorology*, *7*, 285–297. https://doi.org/10.1175/JHM487.1

Drobinski, P., Steinacker, R., Richner, H., Baumann-Stanzer, K., Beffrey, G., Benech, B., Berger, H., Chimani, B., Dabas, A., Dorninger, M., Dürr, B., Flamant, C., Frioud, M., Furger, M., Gröhn, I., Gubser, S., Gutermann, T., Häberli, C., Häller-Scharnhost, E., . . . Zängl, G. (2007). Föhn in the rhine valley during map: a review of its multiscale dynamics in complex valley geometry. *Quarterly Journal of the Royal Meteorological Society*, *133*, 897–916.

Eker, R., Bühler, Y., Schlögl, S., Stoffel, A., & Aydın, A. (2019). Monitoring of snow cover ablation using very high spatial resolution remote sensing datasets. *Remote Sensing*, *11*, 699.

Elliott, W. P. (1958). The growth of the atmospheric internal boundary layer. *Eos, Transactions American Geophysical Union*, *39*, 1048–1054. https://doi.org/10.1029/TR039i006p01048

Essery, R., Granger, R., & Pomeroy, J. (2006). Boundary-layer growth and advection of heat over snow and soil patches: modelling and parameterization. *Hydrological Processes*, *20*, 953–967. https://doi.org/10.1002/hyp.6122

Farina, S., & Zardi, D. (2023). Understanding thermally driven slope winds: recent advances and open questions. *Boundary-Layer Meteorology*. https://doi.org/10.1007/s10546-023-00821-1

Föhn, P. M. B., & Meister, R. (1983). Distribution of snow drifts on ridge slopes: measurements and theoretical approximations. *Annals of Glaciology*, *4*, 52–57. https://doi.org/10.3189/S0260305500005231

Fujita, K., Hiyama, K., Iida, H., & Ageta, Y. (2010). Self-regulated fluctuations in the ablation of a snow patch over four decades. *Water Resources Research*, *46*.

Garratt, J. R. (1990). The internal boundary layer - a review. *Boundary-Layer Meteorology*, *50*, 171–203. https://doi.org/10.1007/BF00120524

Gerber, F., Mott, R., & Lehning, M. (2019). The importance of near-surface winter precipitation processes in complex alpine terrain. *Journal of Hydrometeorology*, *20*, 177–196. https://doi.org/10.1175/JHM-D-18-0055.1

Germano, M., Piomelli, U., Moin, P., & Cabot, W. H. (1991). A dynamic subgrid-scale eddy viscosity model. *Physics of Fluids A: Fluid Dynamics*, *3*, 1760–1765. https://doi.org/10.1063/1.857955

Goger, B., Stiperski, I., Nicholson, L., & Sauter, T. (2022). Large-eddy simulations of the atmospheric boundary layer over an alpine glacier: impact of synoptic flow direction and governing processes. *Quarterly Journal of the Royal Meteorological Society*, *148*, 1319–1343. https://doi.org/10.1002/qj.4263

González-Herrero, S., Sigmund, A., Haugeneder, M., Hames, O., Huwald, H., Fiddes, J., & Lehning, M. (2024). Using the sensible heat flux eddy covariance-based exchange coefficient to calculate latent heat flux from moisture mean gradients over snow. *Boundary-Layer Meteorology (accepted)*.

Grachev, A. A., Leo, L. S., Sabatino, S. D., Fernando, H. J. S., Pardyjak, E. R., & Fairall, C. W. (2016). Structure of turbulence in katabatic flows below and above the wind-speed maximum. *Boundary-Layer Meteorology*, *159*, 469–494. https://doi.org/10.1007/s10546-015-0034-8

Granger, R. J., Pomeroy, J. W., & Parviainen, J. (2002). Boundary-layer integration approach to advection of sensible heat to a patchy snow cover. *Hydrological Processes*, *16*.

Granger, R. J., Essery, R., & Pomeroy, J. W. (2006). Boundary-layer growth over snow and soil patches: field observations. *Hydrological Processes*, *20*, 943–951. https://doi.org/10.1002/hyp.6123

Groffman, P. M., Driscoll, C. T., Fahey, T. J., Hardy, J. P., Fitzhugh, R. D., & Tierney, G. L. (2001). Colder soils in a warmer world: a snow manipulation study in a northern hardwood forest ecosystem. *Biogeochemistry*, *56*, 135–150. https://doi.org/10.1023/A:1013039830323

Grudzielanek, A. M., & Cermak, J. (2015a). Capturing cold-air flow using thermal imaging. *Boundary-Layer Meteorology*, *157*.

Grudzielanek, A. M., & Cermak, J. (2015b). Capturing cold-air flow using thermal imaging. *Boundary-Layer Meteorology*, *157*, 321–332. https://doi.org/10.1007/s10546-015-0042-8

Grünewald, T., Schirmer, M., Mott, R., & Lehning, M. (2010). Spatial and temporal variability of snow depth and ablation rates in a small mountain catchment. *The Cryosphere*, *4*, 215–225. https://doi.org/10.5194/tc-4-215-2010

Haid, M., Gohm, A., Umek, L., Ward, H. C., & Rotach, M. W. (2022). Cold-air pool processes in the inn valley during föhn: a comparison of four cases during the piano campaign. *Boundary-Layer Meteorology*, *182*, 335–362.

Hames, O., Jafari, M., Wagner, D. N., Raphael, I., Clemens-Sewall, D., Polashenski, C., Shupe, M. D., Schneebeli, M., & Lehning, M. (2022). Modeling the small-scale deposition of snow onto structured arctic sea ice during a mosaic storm using snowbedfoam 1.0. *Geoscientific Model Development*, *15*, 6429–6449. https://doi.org/10.5194/gmd-15-6429-2022

Harder, P., Pomeroy, J. W., & Helgason, W. (2017). Local-scale advection of sensible and latent heat during snowmelt. *Geophysical Research Letters*, *44*, 9769–9777. https://doi.org/10.1002/2017GL074394

Haugeneder, M., Lehning, M., Reynolds, D., Jonas, T., & Mott, R. (2023). A novel method to quantify near-surface boundary-layer dynamics at ultra-high spatio-temporal resolution. *Boundary-Layer Meteorology*, *186*, 177–197. https://doi.org/10.1007/s10546-022-00752-3

Haugeneder, M., Lehning, M., Stiperski, I., Reynolds, D., & Mott, R. (2024). Turbulence in the strongly heterogeneous near-surface boundary layer over patchy snow. *Boundary-Layer Meteorology*, *190*, 7. https://doi.org/10.1007/s10546-023-00856-4

Helbig, N., Bühler, Y., Eberhard, L., Deschamps-Berger, C., Gascoin, S., Dumont, M., Revuelto, J., Deems, J. S., & Jonas, T. (2021). Fractional snow-covered area: scale-independent peak of winter parameterization. *The Cryosphere*, *15*, 615–632. https://doi.org/10.5194/tc-15-615-2021

Helbig, N., Schirmer, M., Magnusson, J., Mäder, F., van Herwijnen, A., Quéno, L., Bühler, Y., Deems, J. S., & Gascoin, S. (2021). A seasonal algorithm of the snow-covered area fraction for mountainous terrain. *The Cryosphere*, *15*, 4607–4624. https://doi.org/10.5194/tc-15-4607-2021

Högström, U. (1996). Review of some basic characteristics of the atmospheric surface layer. *Boundary-Layer Meteorology*, *78*, 215–246. https://doi.org/10.1007/BF00120937

Houze, R. A. (2012). Orographic effects on precipitating clouds. *Reviews of Geophysics*, *50*. https://doi.org/10.1029/2011RG000365

Howell, J. F., & Mahrt, L. (1997). Multiresolution flux decomposition. *Boundary-Layer Meteorology*, *83*, 117–137. https://doi.org/10.1023/A:1000210427798

Huang, J., & Bou-Zeid, E. (2013). Turbulence and vertical fluxes in the stable atmospheric boundary layer. part i: a large-eddy simulation study. *Journal of the Atmospheric Sciences*, *70*, 1513–1527. https://doi.org/10.1175/JAS-D-12-0167.1

Hunter, J. D. (2007). Matplotlib: a 2d graphics environment. *Computing in Science & Engineering*, *9*, 90–95. https://doi.org/10.1109/MCSE.2007.55

Inagaki, A., Kanda, M., Onomura, S., & Kumemura, H. (2013). Thermal image velocimetry. *Boundary-Layer Meteorology*, *149*, 1–18.

Jackson, P. L., Mayr, G., & Vosper, S. (2013). Dynamically-driven winds. In F. K. Chow, S. F. D. Wekker, & B. J. Snyder (Eds.), *Mountain weather research and forecasting* (pp. 121–218). Springer Netherlands.

Jafari, M., Sharma, V., & Lehning, M. (2022). Convection of water vapour in snowpacks. *Journal of Fluid Mechanics*, *934*, A38. https://doi.org/10.1017/jfm.2021.1146

Jansing, L., Papritz, L., Dürr, B., Gerstgrasser, D., & Sprenger, M. (2022). Classification of alpine south foehn based on 5 years of kilometre-scale analysis data. *Weather and Climate Dynamics*, *3*, 1113–1138.

Johnson, R. H., Young, G. S., Toth, J. J., & Zehr, R. M. (1984). Mesoscale weather effects of variable snow cover over northeast colorado. *Monthly Weather Review*, *112*, 1141–1152. https://doi.org/10.1175/1520-0493(1984)112<1141:MWEOVS>2.0.CO;2

Kaga, A., Inoue, Y., & Yamaguchi, K. (1992). *Application of a fast algorithm for pattern tracking on airflow measurements*.

Kaimal, J. C., & Finnigan, J. J. (1994, March). *Atmospheric boundary layer flows*. Oxford University Press. https://doi.org/10.1093/oso/9780195062397.001.0001

Kljun, N., Calanca, P., Rotach, M. W., & Schmid, H. P. (2015). A simple two-dimensional parameterisation for flux footprint prediction (ffp). *Geoscientific Model Development*, *8*, 3695–3713. https://doi.org/10.5194/gmd-8-3695-2015

Kolmogorov, A. N. (1941). The local structure of turbulence in incompressible viscous fluid for very large reynolds numbers. *Doklady Akademii Nauk SSSR*, *30*, 301–304.

Lehner, M., & Rotach, M. (2018). Current challenges in understanding and predicting transport and exchange in the atmosphere over mountainous terrain. *Atmosphere*, *9*, 276.

Lehning, M., Löwe, H., Ryser, M., & Raderschall, N. (2008). Inhomogeneous precipitation distribution and snow transport in steep terrain. *Water Resources Research*, *44*. https://doi.org/10.1029/2007WR006545

Lehning, M. (2013). Snow–atmosphere interactions and hydrological consequences. *Advances in Water Resources*, *55*, 1–3. https://doi.org/10.1016/j.advwatres.2013.02.001

Lehning, M., Völksch, I., Gustafsson, D., Nguyen, T. A., Stähli, M., & Zappa, M. (2006). Alpine3d: a detailed model of mountain surface processes and its application to snow hydrology. *Hydrological Processes*, *20*, 2111–2128. https://doi.org/10.1002/hyp.6204

Leslie, D. C., & Quarini, G. L. (1979). The application of turbulence theory to the formulation of subgrid modelling procedures. *Journal of Fluid Mechanics*, *91*, 65. https://doi.org/10.1017/S0022112079000045

Letcher, T. W., & Minder, J. R. (2015). Characterization of the simulated regional snow albedo feedback using a regional climate model over complex terrain. *Journal of Climate*, *28*, 7576–7595. https://doi.org/10.1175/JCLI-D-15-0166.1

Letcher, T. W., & Minder, J. R. (2017). The simulated response of diurnal mountain winds to regionally enhanced warming caused by the snow albedo feedback. *Journal of Atmospheric Science*, *74*, 49–67. https://doi.org/10.1175/JAS-D-16-0158.1

Li, D., Lettenmaier, D. P., Margulis, S. A., & Andreadis, K. (2019). The role of rain-on-snow in flooding over the conterminous united states. *Water Resources Research*, *55*, 8492–8513. https://doi.org/10.1029/2019WR024950

Li, H., & Zhu, M. (2009, October). Simulation of vignetting effect in thermal imaging system. In J. K. Udupa, N. Sang, L. G. Nyul, & H. Tong (Eds.).

Liston, G. E. (1995). Local advection of momentum, heat, and moisture during the melt of patchy snow covers. *Journal of Applied Meteorology*, *34*.

Lund, T. (2003). The use of explicit filters in large eddy simulation. *Computers & Mathematics with Applications*, *46*, 603–616. https://doi.org/10.1016/S0898-1221(03)90019-8

Lundquist, J. D., Vano, J., Gutmann, E., Hogan, D., Schwat, E., Haugeneder, M., Mateo, E., Oncley, S., Roden, C., Osenga, E., & Carver, L. (2024). Sublimation of snow. *Bulletin of the American Meteorological Society*. https://doi.org/10.1175/BAMS-D-23-0191.1

Magnusson, J., Nævdal, G., Matt, F., Burkhart, J. F., & Winstral, A. (2020). Improving hydropower inflow forecasts by assimilating snow data. *Hydrology Research*, *51*, 226–237. https://doi.org/10.2166/nh.2020.025

Mahrt, L. (2014). Stably stratified atmospheric boundary layers. *Annual Review of Fluid Mechanics*, *46*, 23–45. https://doi.org/10.1146/annurev-fluid-010313-141354

Mahrt, L., & Vickers, D. (2006). Extremely weak mixing in stable conditions. *Boundary-Layer Meteorology*, *119*, 19–39.

Marsh, P., & Pomeroy, J. W. (1996). Meltwater fluxes at an arctic forest-tundra site. *Hydrological Processes*, *10*, 1383–1400. https://doi.org/10.1002/(SICI)1099-1085(199610)10:10<1383::AID-HYP468>3.0.CO;2-W

Marty, C., Rohrer, M. B., Huss, M., & Stähli, M. (2023). Multi-decadal observations in the alps reveal less and wetter snow, with increasing variability. *Frontiers in Earth Science*, *11*. https://doi.org/10.3389/feart.2023.1165861

Melo, D. B., Sigmund, A., & Lehning, M. (2024). Understanding snow saltation parameterizations: lessons from theory, experiments and numerical simulations. *The Cryosphere*, *18*, 1287–1313. https://doi.org/10.5194/tc-18-1287-2024

Ménard, C. B., Essery, R., & Pomeroy, J. (2014a). Modelled sensitivity of the snow regime to topography, shrub fraction and shrub height. *Hydrology and Earth System Sciences*, *18*, 2375–2392.

Ménard, C. B., Essery, R., & Pomeroy, J. (2014b). Modelled sensitivity of the snow regime to topography, shrub fraction and shrub height. *Hydrology and Earth System Sciences*, *18*, 2375–2392. https://doi.org/10.5194/hess-18-2375-2014

Meneveau, C., Lund, T. S., & Cabot, W. H. (1996). A lagrangian dynamic subgrid-scale model of turbulence. *Journal of Fluid Mechanics*, *319*, 353. https://doi.org/10.1017/S0022112096007379

Minder, J. R., Durran, D. R., Roe, G. H., & Anders, A. M. (2008). The climatology of small-scale orographic precipitation over the olympic mountains: patterns and processes. *Quarterly Journal of the Royal Meteorological Society*, *134*, 817–839. https://doi.org/10.1002/qj.258

Monin, A. S., & Obukhov, A. M. (1954). Basic laws of turbulent mixing in the surface layer of the atmosphere. *Contrib. Geophys. Inst. Acad. Sci. USSR*, *24*(151), 163–187.

Moreno, J. L., Goyette, S., Beniston, M., & Alvera, B. (2008). Sensitivity of the snow energy balance to climatic changes: prediction of snowpack in the pyrenees in the 21st century. *Climate Research*, *36*, 203–217. https://doi.org/10.3354/cr00747

Mott, R., Egli, L., Grünewald, T., Dawes, N., Manes, C., Bavay, M., & Lehning, M. (2011). Micrometeorological processes driving snow ablation in an alpine catchment. *The Cryosphere*, *5*, 1083–1098. https://doi.org/10.5194/tc-5-1083-2011

Mott, R., Gromke, C., Grünewald, T., & Lehning, M. (2013). Relative importance of advective heat transport and boundary layer decoupling in the melt dynamics of a patchy snow cover. *Advances in Water Resources*, *55*, 88–97. https://doi.org/10.1016/j.advwatres.2012.03.001

Mott, R., Schlögl, S., Dirks, L., & Lehning, M. (2017). Impact of extreme land surface heterogeneity on micrometeorology over spring snow cover. *Journal of Hydrometeorology*, *18*, 2705–2722. https://doi.org/10.1175/JHM-D-17-0074.1

Mott, R., Daniels, M., & Lehning, M. (2015). Atmospheric flow development and associated changes in turbulent sensible heat flux over a patchy mountain snow cover. *Journal of Hydrometeorology*, *16*, 1315–1340. https://doi.org/10.1175/JHM-D-14-0036.1

Mott, R., Paterna, E., Horender, S., Crivelli, P., & Lehning, M. (2016). Wind tunnel experiments: cold-air pooling and atmospheric decoupling above a melting snow patch. *The Cryosphere*, *10*(1), 445–458. https://doi.org/10.5194/tc-10-445-2016

Mott, R., Stiperski, I., & Nicholson, L. (2020). Spatio-temporal flow variations driving heat exchange processes at a mountain glacier. *The Cryosphere, 14*, 4699–4718.

Mott, R., Vionnet, V., & Grünewald, T. (2018). The seasonal snow cover dynamics: review on wind-driven coupling processes. *Frontiers in Earth Science*, *6*. https://doi.org/10.3389/feart.2018.00197

Mott, R., Winstral, A., Cluzet, B., Helbig, N., Magnusson, J., Mazzotti, G., Quéno, L., Schirmer, M., Webster, C., & Jonas, T. (2023a). Operational snow-hydrological modeling for switzerland. *Frontiers in Earth Science*, *11*. https://doi.org/10.3389/feart.2023.1228158

Mott, R., Winstral, A., Cluzet, B., Helbig, N., Magnusson, J., Mazzotti, G., Quéno, L., Schirmer, M., Webster, C., & Jonas, T. (2023b). Operational snow-hydrological modeling for switzerland. *Frontiers in Earth Science*, *11*. https://doi.org/10.3389/feart.2023.1228158

Mott, R., Wolf, A., Kehl, M., Kunstmann, H., Warscher, M., & Grünewald, T. (2019). Avalanches and micrometeorology driving mass and energy balance of the lowest perennial ice field of the alps: a case study. *The Cryosphere*, *13*, 1247–1265. https://doi.org/10.5194/tc-13-1247-2019

Moukalled, F., Mangani, L., & Darwish, M. (2016). *The finite volume method in computational fluid dynamics* (Vol. 113). Springer International Publishing. https://doi.org/10.1007/978-3-319-16874-6

Nadeau, D. F., Pardyjak, E. R., Higgins, C. W., & Parlange, M. B. (2013). Similarity scaling over a steep alpine slope. *Boundary-Layer Meteorology, 147*, 401–419.

Neumann, N., & Marsh, P. (1998). Local advection of sensible heat in the snowmelt landscape of arctic tundra. *Hydrological Processes, 12*.

OpenFoam API Guide. (2024). Buoyantboussinesqpimplefoam.c file reference [Last accessed: 3 April 2024].

Pestana, S., Chickadel, C. C., Harpold, A., Kostadinov, T. S., Pai, H., Tyler, S., Webster, C., & Lundquist, J. D. (2019). Bias correction of airborne thermal infrared observations over forests using melting snow. *Water Resources Research*, *55*.

Plavcan, D., Mayr, G. J., & Zeileis, A. (2014). Automatic and probabilistic foehn diagnosis with a statistical mixture model. *Journal of Applied Meteorology and Climatology*, *53*, 652–659. https://doi.org/10.1175/JAMC-D-13-0267.1

Pohl, S., Marsh, P., & Liston, G. E. (2006). Spatial-temporal variability in turbulent fluxes during spring snowmelt. *Arctic, Antarctic, and Alpine Research*, *38*(1), 136–146.

Poletto, R., Craft, T., & Revell, A. (2013). A new divergence free synthetic eddy method for the reproduction of inlet flow conditions for les. *Flow, Turbulence and Combustion*, *91*, 519–539. https://doi.org/10.1007/s10494-013-9488-2

Pomeroy, J., & Gray, D. (1995). *Snowcover accumulation, relocation and management* (1st ed.). NHRI Science Report No. 7, National Hydrology Research Institute.

Pope, S. B. (2000, August). *Turbulent flows*. Cambridge University Press. https://doi.org/10.1017/CBO9780511840531

Quéno, L., Mott, R., Morin, P., Cluzet, B., Mazzotti, G., & Jonas, T. (2023). Snow redistribution in an intermediate-complexity snow hydrology modelling framework. *EGUsphere*, *2023*, 1–32. https://doi.org/10.5194/egusphere-2023-2071

Reynolds, D., Quéno, L., Lehning, M., Jafari, M., Berg, J., Jonas, T., Haugeneder, M., & Mott, R. (2024). Seasonal snow-atmosphere modeling: let's do it. *EGUsphere*, *2024*, 1–28. https://doi.org/10.5194/egusphere-2024-489

Reynolds, D., Gutmann, E., Kruyt, B., Haugeneder, M., Jonas, T., Gerber, F., Lehning, M., & Mott, R. (2023). The high-resolution intermediate complexity atmospheric research (hicar v1.1) model enables fast dynamic downscaling to the hectometer scale. *Geoscientific Model Development*, *16*, 5049–5068. https://doi.org/10.5194/gmd-16-5049-2023

Richardson, H., Basu, S., & Holtslag, A. A. M. (2013). Improving stable boundary-layer height estimation using a stability-dependent critical bulk richardson number. *Boundary-Layer Meteorology*, *148*, 93–109. https://doi.org/10.1007/s10546-013-9812-3

Rixen, C., Høye, T. T., Macek, P., Aerts, R., Alatalo, J. M., Anderson, J. T., Arnold, P. A., Barrio, I. C., Bjerke, J. W., Björkman, M. P., Blok, D., Blume-Werry, G., Boike, J., Bokhorst, S., Carbognani, M., Christiansen, C. T., Convey, P., Cooper, E. J., Cornelissen, J. H. C., … Zong, S. (2022). Winters are changing: snow effects on arctic and alpine tundra ecosystems. *Arctic Science*, *8*, 572–608. https://doi.org/10.1139/as-2020-0058

Rotach, M. W., Gohm, A., Lang, M. N., Leukauf, D., Stiperski, I., & Wagner, J. S. (2015). On the vertical exchange of heat, mass, and momentum over complex, mountainous terrain. *Frontiers in Earth Science*, *3*. https://doi.org/10.3389/feart.2015.00076

Sauter, T., & Galos, S. P. (2016). Effects of local advection on the spatial sensible heat flux variation on a mountain glacier. *The Cryosphere*, *10*.

Schaefli, B., Hingray, B., & Musy, A. (2007). Climate change and hydropower production in the swiss alps: quantification of potential impacts and related modelling uncertainties. *Hydrology and Earth System Sciences*, *11*, 1191–1205.

Schirmer, M., & Lehning, M. (2011). Persistence in intra-annual snow depth distribution: 2. fractal analysis of snow depth development. *Water Resources Research*, *47*. https://doi.org/10.1029/2010WR009429

Schirmer, M., Wirz, V., Clifton, A., & Lehning, M. (2011). Persistence in intra-annual snow depth distribution: 1. measurements and topographic control. *Water Resources Research*, *47*. https://doi.org/10.1029/2010WR009426

Schlögl, S., Lehning, M., Fierz, C., & Mott, R. (2018a). Representation of horizontal transport processes in snowmelt modeling by applying a footprint approach. *Frontiers in Earth Science*, *6*.

Schlögl, S., Lehning, M., & Mott, R. (2018b). How are turbulent sensible heat fluxes and snow melt rates affected by a changing snow cover fraction? *Frontiers in Earth Science*, *6*.

Schlögl, S., Lehning, M., Nishimura, K., Huwald, H., Cullen, N. J., & Mott, R. (2017a). How do stability corrections perform in the stable boundary layer over snow? *Boundary-Layer Meteorology*, *165*, 161–180. https://doi.org/10.1007/s10546-017-0262-1

Schlögl, S., Lehning, M., Nishimura, K., Huwald, H., Cullen, N. J., & Mott, R. (2017b). How do stability corrections perform in the stable boundary layer over snow? *Boundary-Layer Meteorology*, *165*.

Schmidli, J. (2013). Daytime heat transfer processes over mountainous terrain. *Journal of Atmospheric Science*, *70*, 4041–4066.

Schotanus, P., Nieuwstadt, F., & Bruin, H. D. (1983). Temperature measurement with a sonic anemometer and its application to heat and moisture fluxes. *Boundary-Layer Meteorology*, *26*, 81–93. https://doi.org/10.1007/BF00164332

Segal, M., Garratt, J. R., Pielke, R. A., & Ye, Z. (1991). Scaling and numerical model evaluation of snow-cover effects on the generation and modification of daytime mesoscale circulations. *Journal of the Atmospheric Sciences*, *48*, 1024–1042. https://doi.org/10.1175/1520-0469(1991)048<1024:SANMEO>2.0.CO;2

Serafin, S., Adler, B., Cuxart, J., Wekker, S. D., Gohm, A., Grisogono, B., Kalthoff, N., Kirshbaum, D., Rotach, M., Schmidli, J., Stiperski, I., Večenaj, Ž., & Zardi, D. (2018). Exchange processes in the atmospheric boundary layer over mountainous terrain. *Atmosphere*, *9*, 102. https://doi.org/10.3390/atmos9030102

Sigmund, A., Dujardin, J., Comola, F., Sharma, V., Huwald, H., Melo, D. B., Hirasawa, N., Nishimura, K., & Lehning, M. (2022). Evidence of strong flux underestimation by bulk parametrizations during drifting and blowing snow. *Boundary-Layer Meteorology*, *182*, 119–146. https://doi.org/10.1007/s10546-021-00653-x

Siirila-Woodburn, E. R., Rhoades, A. M., Hatchett, B. J., Huning, L. S., Szinai, J., Tague, C., Nico, P. S., Feldman, D. R., Jones, A. D., Collins, W. D., & Kaatz, L. (2021). A low-to-no snow future and its impacts on water resources in the western united states. *Nature Reviews Earth & Environment*, *2*, 800–819. https://doi.org/10.1038/s43017-021-00219-y

Smagorinski, J. (1963). General circulation experiments with the primitive equations. *Monthly Weather Review*, *91*, 99–164. https://doi.org/10.1175/1520-0493(1963)091<0099:GCEWTP>2.3.CO;2

Smith, C. M., & Porté-Agel, F. (2014). An intercomparison of subgrid models for large-eddy simulation of katabatic flows. *Quarterly Journal of the Royal Meteorological Society*, *140*, 1294–1303. https://doi.org/10.1002/qj.2212

Stiperski, I., & Calaf, M. (2023). Generalizing monin-obukhov similarity theory (1954) for complex atmospheric turbulence. *Physical Review Letters*, *130*, 124001. https://doi.org/10.1103/PhysRevLett.130.124001

Stiperski, I., & Rotach, M. W. (2016). On the measurement of turbulence over complex mountainous terrain. *Boundary-Layer Meteorology*, *159*, 97–121. https://doi.org/10.1007/s10546-015-0103-z

Stoll, R., Gibbs, J. A., Salesky, S. T., Anderson, W., & Calaf, M. (2020). Large-eddy simulation of the atmospheric boundary layer. *Boundary-Layer Meteorology*, *177*, 541–581. https://doi.org/10.1007/s10546-020-00556-3

Stucchi, L., Bombelli, G., Bianchi, A., & Bocchiola, D. (2019). Hydropower from the alpine cryosphere in the era of climate change: the case of the sabbione storage plant in italy. *Water*, *11*, 1599. https://doi.org/10.3390/w11081599

Stull, R. B. (1988). *An introduction to boundary layer meteorology*. Springer Netherlands. https://doi.org/10.1007/978-94-009-3027-8

Sturm, M., Goldstein, M. A., & Parr, C. (2017). Water and life from snow: a trillion dollar science question. *Water Resources Research*, *53*, 3534–3544. https://doi.org/10.1002/2017WR020840

Sui, J., & Koehler, G. (2001). Rain-on-snow induced flood events in southern germany. *Journal of Hydrology*, *252*, 205–220. https://doi.org/10.1016/S0022-1694(01)00460-7

Takahara, H., & Higuchi, K. (1985a). Thermal modification of air moving over melting snow surfaces. *Annals of Glaciology*, *6*, 235–237. https://doi.org/10.3189/1985AoG6-1-235-237

Takahara, H., & Higuchi, K. (1985b). Thermal modification of air moving over melting snow surfaces. *Annals of Glaciology*, *6*.

Taylor, G. I. (1938). The spectrum of turbulence. *Proceedings of the Royal Society Series A - Mathematical and Physical Sciences*, *164*, 476–490.

Trujillo, E., Ramírez, J. A., & Elder, K. J. (2007). Topographic, meteorologic, and canopy controls on the scaling characteristics of the spatial distribution of snow depth fields. *Water Resources Research*, *43*. https://doi.org/10.1029/2006WR005317

Urfer-Henneberger, C. (1970). Neuere beobachtungen über die entwicklung des schönwetterwindsystems in einem v-förmigen alpental (dischmatal bei davos). *Archiv fur Meteorologie Geophysik und Bioklimatologie Serie B*, *18*, 21–42. https://doi.org/10.1007/BF02245866

van der Valk, L. D., Teuling, A. J., Girod, L., Pirk, N., Stoffer, R., & van Heerwaarden, C. C. (2021). Understanding wind-driven melt of patchy snow cover. *The Cryosphere Discussions*, *2021*, 1–32. https://doi.org/10.5194/tc-16-4319-2022

van der Valk, L. D., Teuling, A. J., Girod, L., Pirk, N., Stoffer, R., & van Heerwaarden, C. C. (2022). Understanding wind-driven melt of patchy snow cover. *The Cryosphere*, *16*, 4319–4341.

Vickers, D., & Mahrt, L. (1997). Quality control and flux sampling problems for tower and aircraft data. *Journal of Atmospheric and Oceanic Technology*, *14*, 15.

Vickers, D., & Mahrt, L. (2003). The cospectral gap and turbulent flux calculations. *Journal of Atmospheric and Oceanic Technology*, *20*, 660–672. https://doi.org/10.1175/1520-0426(2003)20<660:TCGATF>2.0.CO;2

Weisman, R. N. (1977). Snowmelt: a two-dimensional turbulent diffusion model. *Water Resources Research*, *13*, 337–342. https://doi.org/10.1029/WR013i002p00337

Weller, H. G., Tabor, G., Jasak, H., & Fureby, C. (1998). A tensorial approach to computational continuum mechanics using object-oriented techniques. *Computers in Physics*, *12*, 620–631. https://doi.org/10.1063/1.168744

Wever, N., Comola, F., Bavay, M., & Lehning, M. (2017). Simulating the influence of snow surface processes on soil moisture dynamics and streamflow generation in an alpine catchment. *Hydrology and Earth System Sciences*, *21*, 4053–4071. https://doi.org/10.5194/hess-21-4053-2017

Wheeler, J. A., Cortés, A. J., Sedlacek, J., Karrenberg, S., van Kleunen, M., Wipf, S., Hoch, G., Bossdorf, O., & Rixen, C. (2016). The snow and the willows: earlier spring snowmelt reduces performance in the low-lying alpine shrub *Salix herbacea* (H. Cornelissen, Ed.). *Journal of Ecology*, *104*, 1041–1050. https://doi.org/10.1111/1365-2745.12579

Whiteman, C. D., & Doran, J. C. (1993). The relationship between overlying synoptic-scale flows and winds within a valley. *Journal of Applied Meteorology*, *32*, 1669–1682. https://doi.org/10.1175/1520-0450(1993)032<1669:TRBOSS>2.0.CO;2

Wipf, S., & Rixen, C. (2010). A review of snow manipulation experiments in arctic and alpine tundra ecosystems. *Polar Research*, *29*, 95–109. https://doi.org/10.1111/j.1751-8369.2010.00153.x

Würzer, S., Jonas, T., Wever, N., & Lehning, M. (2016). Influence of initial snowpack properties on runoff formation during rain-on-snow events. *Journal of Hydrometeorology*, *17*, 1801–1815. https://doi.org/10.1175/JHM-D-15-0181.1

Zahn, E., & Bou-Zeid, E. (2024). Setting up a large-eddy simulation to focus on the atmospheric surface layer. *Boundary-Layer Meteorology*, *190*, 12. https://doi.org/10.1007/s10546-023-00841-x

Zängl, G. (2009). The impact of weak synoptic forcing on the valley-wind circulation in the alpine inn valley. *Meteorology and Atmospheric Physics*, *105*, 37–53.

Zardi, D., & Whiteman, C. D. (2013). Diurnal mountain wind systems. In F. K. Chow, S. F. D. Wekker, & B. J. Snyder (Eds.), *Mountain weather research and forecasting* (pp. 35–119). Springer Netherlands. https://doi.org/10.1007/978-94-007-4098-3_2

Zilitinkevich, S. S., Elperin, T., Kleeorin, N., & Rogachevskii, I. (2007). Energy- and flux-budget (EFB) turbulence closure model for stably stratified flows. part i: steady-state, homogeneous regimes. *Boundary-Layer Meteorology*, *125*(2), 167–191.

Zwaaftink, C. D. G., Diebold, M., Horender, S., Overney, J., Lieberherr, G., Parlange, M. B., & Lehning, M. (2014). Modelling small-scale drifting snow with a lagrangian stochastic model based on large-eddy simulations. *Boundary-Layer Meteorology*, *153*, 117–139. https://doi.org/10.1007/s10546-014-9934-2

Michael Haugeneder

michael.haugeneder@slf.ch

Education

2004 – 2013 **high school** Gabriel-von-Seidl-Gymnasium Bad Tölz

2013 – 2017 **B.Sc. Physics, Munich** in Applied and Engineering Physics.
Thesis title: *Morphology and Electronic Characteristics of Organic Molecules on Semiconductors.*
Supervisor: Prof. Martin Stutzmann

2017 – 2020 **M.Sc. Physics, Munich** in Applied and Engineering Physics.
Thesis title: *Optimization of A Cylindrical Para-Hydrogen Moderator for Cold Neutrons.*
Supervisor: Prof. Christoph Morkel

2020 – 2024 **Ph.D., EPFL Lausanne** in Cryospheric Sciences.
Thesis title: *Turbulence and Heat Exchange in the Near-Surface Boundary Layer over Patchy Snow.*
Supervisors: Prof. Michael Lehning and Dr. Rebecca Mott

Research Publications

Journal Articles

① S. González-Herrero, A. Sigmund, **M. Haugeneder**, *et al.*, "Using the sensible heat flux eddy covariance-based exchange coefficient to calculate latent heat flux from moisture mean gradients over snow," *Boundary-Layer Meteorology*, Mar. 2024 (accepted).

② **M. Haugeneder**, M. Lehning, O. Hames, M. Jafari, D. Reynolds, and R. Mott, "Large eddy simulation of near-surface boundary layer dynamics over patchy snow," *Frontiers in Earth Science*, 2024 (in review).

③ J. D. Lundquist, J. Vano, E. Gutmann, *et al.*, "Sublimation of snow," *Bulletin of the American Meteorological Society*, Apr. 2024, ISSN: 0003-0007. DOI: `10.1175/BAMS-D-23-0191.1`.

④ **M. Haugeneder**, M. Lehning, I. Stiperski, D. Reynolds, and R. Mott, "Turbulence in the strongly heterogeneous near-surface boundary layer over patchy snow," *Boundary-Layer Meteorology*, vol. 190, p. 7, 2 Feb. 2024, ISSN: 0006-8314. DOI: `10.1007/s10546-023-00856-4`.

⑤ D. Reynolds, L. Quéno, M. Lehning, *et al.*, "Seasonal snow-atmosphere modeling: Let's do it," *EGUsphere*, vol. 2024, pp. 1–28, 2024. DOI: `10.5194/egusphere-2024-489`.

⑥ **M. Haugeneder**, M. Lehning, D. Reynolds, T. Jonas, and R. Mott, "A novel method to quantify near-surface boundary-layer dynamics at ultra-high spatio-temporal resolution," *Boundary-Layer Meteorology*, vol. 186, pp. 177–197, 2 Feb. 2023, ISSN: 0006-8314. DOI: `10.1007/s10546-022-00752-3`.

⑦ D. Reynolds, E. Gutmann, B. Kruyt, *et al.*, "The high-resolution intermediate complexity atmospheric research (hicar v1.1) model enables fast dynamic downscaling to the hectometer scale," *Geoscientific Model Development*, vol. 16, pp. 5049–5068, 17 Sep. 2023, ISSN: 1991-9603. DOI: `10.5194/gmd-16-5049-2023`.

Skills

Languages German (native speaker), English (proficient)

Coding Julia, Python, C++, LaTeX, Unix/Bash

Skills (continued)

Misc.	Academic research, field work, teaching.

Experience

since 2012	instructor and active member of the Bavarian Mountain Rescue team